Chair of Drilling and Completion Engineering

Master's Thesis

Sorption of Nanomaterials to Rock

Christian Scheurer, BSc

September 2021

Christian Scheurer BSc

Master Thesis 2021

Supervisors:
Univ.-Prof. MBA, PhD Kris Ravi
Dr. Rafael E. Hincapie
Dr. Elisabeth Neubauer

Sorption of Nanomaterials to Rock

dpe DEPARTMENT PETROLEUM ENGINEERING

MONTAN UNIVERSITÄT

I dedicate this thesis to my father,
for supporting me and being a friend that I can rely on.

Affidavit

I declare in lieu of oath that I wrote this thesis and performed the associated research myself using only literature cited in this volume.

Eidesstattliche Erklärung

Ich erkläre an Eides statt, dass ich diese Arbeit selbständig verfasst, andere als die angegebenen Quellen und Hilfsmittel nicht benutzt und mich auch sonst keiner unerlaubten Hilfsmittel bedient habe.

Christian Scheurer, 20. September 2021

Abstract

Nanoparticles have gained close attention over the recent years in many industries but especially so in the oil and gas. Various researches have been investigating, for instance, the use of surface-modified silica nanoparticles in reservoir rock applications.

In this work, the interaction of silica nanoparticles and sandstone rock was investigated using a combination of various experimental approaches. Among others, fluid-fluid and rock-fluid interactions were assessed by means of fluid compatibility, batch sorption experiments and single-phase core floods. The underlying task was to gain a better understanding on the factors influencing nanoparticle adsorption to the rock material.

In the experimental approach, diol and polyethylenglycol (PEG) surface-modified silica nanoparticles were tested using two brines differing in ionic strength, plus sodium carbonate (Na_2CO_3) and Berea and Keuper outcrops (core plug and crushed form). Core flood effluents were analysed to define changes in concentration and a rock's retention compared to a tracer. Field Flow Fractionation (FFF) and Dynamic light scattering (DLS) in selected effluent samples were performed to investigate changes in size distribution. Adsorption was evaluated using UV-visible Spectroscopy and scanning electron microscopy (SEM).

Highest adsorption was observed in brine with high ionic strength whereas the use of alkali reduced the adsorption. Crushed material from Berea rock showed slightly higher adsorption compared to Keuper rock whereas temperature had a minor effect on adsorption behaviour. In single phase core-flood experiments no effects on permeability have been observed. The used nanoparticles showed a delayed breakthrough compared to the tracer and bigger particles passed the rock core faster. Nanoparticle recovery was significantly low for PEG-modified nanoparticles in Berea, suggesting high adsorption. SEM images indicate, that adsorption spots are defined via surface roughness rather than mineral type. Despite an excess of nanoparticles in the porous medium monolayer adsorption was the prevailing type observed.

Investigation of nanoparticle interactions with rocks required the development and improvement of methods to evaluate concentration history and recovery. The understanding obtained is crucial for further research in this area and application in a possible field trial.

Zusammenfassung

Nanopartikel haben in den letzten Jahren in vielen Industriezweigen, insbesondere aber in der Öl- und Gasindustrie, große Aufmerksamkeit erregt. In verschiedenen Forschungsarbeiten wurde beispielsweise der Einsatz von oberflächenmodifizierten Siliziumdioxidnanopartikeln in Lagerstättengestein untersucht.

In dieser Arbeit wurde die Wechselwirkung von Nanopartikel mit Sandstein durch eine Kombination verschiedener experimenteller Ansätze untersucht. Unter anderem wurden Fluid - Fluid- und Gestein - Fluid-Wechselwirkungen mittels Kompatibilitätstests, Batch-Sorptionsexperimenten und einphasigen Kernflutversuchen bewertet. Die zugrundeliegende Aufgabe bestand darin, ein besseres Verständnis für die Faktoren zu erlangen, die die Adsorption von Nanopartikeln an das Gesteinsmaterial beeinflussen.

In dem experimentellen Ansatz wurden Diol- und Polyethylenglycol (PEG)-oberflächenmodifizierte Siliziumdioxidnanopartikel unter Verwendung von zwei Solen mit unterschiedlicher Ionenstärke sowie Natriumcarbonat (Na_2CO_3) und Berea und Keuper Aufschlüssen (Kernmaterial und gebrochene Form) getestet. Die Effluenten der Kernflutversuche wurden analysiert, um Konzentrationsänderungen und die Rückhaltung der Nanopartikel im Gestein zu bestimmen. Feldflussfraktionierung (FFF) und dynamische Lichtstreuung (DLS) wurden in ausgewählten Proben durchgeführt, um Veränderungen in der Größenverteilung zu untersuchen. Die Adsorption wurde mit Hilfe der UV-Vis-Spektroskopie und der Rasterelektronenmikroskopie (SEM) bewertet.

Die höchste Adsorption wurde in Sole mit hoher Ionenstärke beobachtet, während die Verwendung von Alkali die Adsorption verringerte. Zerkleinertes Material aus Berea-Gestein zeigte eine etwas höhere Adsorption im Vergleich zu Keuper-Gestein, während die Temperatur einen geringen Einfluss auf das Adsorptionsverhalten hatte. In einphasigen Kernflutversuchen wurden keine Auswirkungen auf die Permeabilität beobachtet. Die verwendeten Nanopartikel zeigten im Vergleich zum Tracer einen verzögerten Durchbruch und größere Partikel passierten den Gesteinskern schneller. Die Rückgewinnung von Nanopartikeln war bei PEG-modifizierten Nanopartikeln in Berea signifikant niedrig, was auf eine hohe Adsorption schließen lässt. REM-Bilder zeigen, dass die Adsorptionsstellen eher durch die Oberflächenrauheit als durch die Mineralart definiert sind. Trotz eines Überschusses an Nanopartikeln im porösen Medium war die Adsorption in einer Monoschicht der vorherrschende Typ.

Die Untersuchung der Wechselwirkungen zwischen Nanopartikeln und Gestein erforderte die Entwicklung und Verbesserung von Methoden zur Bewertung des Konzentrationsverlaufs und der Rückgewinnung. Die gewonnenen Erkenntnisse sind entscheidend für die weitere Forschung in diesem Bereich und die Anwendung in einem möglichen Feldversuch.

Acknowledgements

Throughout this study I have received great support by my family who never stopped believing in me. I am extremely thankful for the love and trust you gave me.

I would like to express my deep and sincere gratitude to my supervisors Dr. Rafael E. Hincapie and Dr. Elisabeth Neubauer. You guided me during this thesis while allowing me to find my own solutions for the challenges given.

Further, I want to thank the team of OMV's Tech Center & Lab for the collaboration and especially Linda Kirchberger for enabling me the laboratory work despite these challenging times. I am extremely thankful for the help Johannes Schnöller, Ante Borovina and Magdalena Biernat gave me, as well as Astrid Metz for introducing me to the exciting world of scanning electron microscopy.

Finally, I would like to thank Nicole for giving me the strength to never give up and push myself beyond my own expectations.

Contents

Chapter 1 Introduction *1*
1.1 Background 1
1.2 Objectives 2
1.3 Milestones 3
1.4 Outline 3

Chapter 2 Theoretical Background *5*
2.1 Formation Damage Mechanisms 5
2.1.1 Fines Migration & Pore Throat Blockage 6
2.1.2 Clay Induced Damage 6
2.2 Fluid Types used in the Reservoir Rock 8
2.2.1 Drilling Fluids 8
2.2.2 Cement 10
2.2.3 Completion & Workover Fluids 11
2.2.4 Injection Fluids 11
2.3 Surface Chemistry 11
2.3.1 DLVO Theory 12
2.3.2 Electric Double Layer & Zeta Potential 12
2.3.3 Formation of Surface Charges 14
2.3.4 Measurement of Zeta Potential of Solid Surfaces 15
2.3.5 Measurement of Zeta Potential of Nanoparticles 15
2.4 Nanomaterials 16
2.4.1 Application of Nanotechnology in Upstream 17
2.4.2 Unique Properties of Nanoparticles 21
2.4.3 Adsorption of Nanoparticles 22

Chapter 3 Materials and Methods *25*
3.1 Materials 25
3.1.1 Core Plugs 25
3.1.2 Fluids 28
3.1.3 Chemical Combinations and Concentrations 30
3.2 Experimental Procedures 31
3.2.1 Overall Methodology 31
3.2.2 Porosity 32
3.2.3 Permeability 32
3.2.4 Streaming Potential 33
3.2.5 Density Measurements 34
3.2.6 pH Measurements 34
3.2.7 Particle Size Measurement 34
3.2.8 Zeta potential Measurements 36
3.2.9 UV-Vis Spectrophotometry 36
3.2.10 Batch Sorption Experiment 38
3.2.11 Core Flooding 39
3.2.12 Scanning Electron Microscope (SEM) 41

3.2.13 Ion Chromatography 41
Chapter 4 Results and Discussion *43*
4.1 Fluid Compatibility 43
4.2 Batch Sorption 43
4.3 Core Flood Experiments 49
4.3.1 Permeability to Brine 49
4.3.2 Effluent Analysis 51
4.3.3 FFF & Particle Size Measurements 58
4.4 Scanning Electron Microscopy (SEM) 59
4.4.1 Effect of Minerology 59
4.4.2 Effect of Brine 62
4.4.3 Vacuum Saturation vs. Core Flood 63
4.4.4 Discussion of Scanning Electron Microscopy Results 64
Chapter 5 Conclusion and Future Work *65*
5.1 Conclusion 65
5.2 Future Work 65

Chapter 1 Introduction

1.1 Background

Nanotechnology has gained a good place over the last decade, dramatically influencing many different industries. For instance, the oil and gas industry have been looking into its potential benefits with applications in up and downstream. On the former, nanotechnology for example provides new and promising approaches when applied in reservoir areas. Applications in the upstream business to name some, are in enhanced oil recovery (EOR) or drilling related activities. For instance, to reduce formation damage during drilling, cementing and production as well as enhance production in mature fields (Saleh et al., 2020; Neubauer et al., 2020; Gbadamosi et al., 2019). Furthermore, nanoparticle additives have shown potential benefits in maintaining borehole stability, cleaning and as emulsion lubricant. They can be utilized to protect the reservoir formation, reduce fluid loss and prevent shale swelling (McDonald 2012, Sharma et al. 2012, Contreras et al. 2014, Fink 2015, Omurlu, Pham, and Nguyen 2016, Pham and Nguyen 2013). On the one hand, due to their small size, nanoparticles have the ability to pass through reservoir rock and on the other hand, they can be surface active, which is a key requirement for influencing oil-rock-water interfaces.

The context and potential applications have attracted the interest of OMV Exploration & Production GmbH. With applications that reach from production facilities to reservoir displacement, the company has made efforts to advance on the depth of their evaluation. From an EOR point of view, the company is investigating two main mechanisms:

- Stabilization of emulsions created during alkali-polymer flooding
- Wettability alteration towards a water-wet state and release of oil from rock surface

These mechanisms are expected not only to be heavily influenced by the adsorption of nanoparticles to reservoir rock. But, also to cause potential formation damage that is currently still unknown and subject of study. Hence, remains unclear, whether nanomaterial application in OMV assets would lead to formation damage caused by the sorption process into reservoir rock. This and other related aspects are covered in this work by means of a detailed laboratory evaluation together with external partners.

1.2 Objectives

In this master thesis the sorption of surface modified silica nanoparticles to reservoir rock is evaluated. Multiple variables are deemed highly important, such as rock mineralogy, nanomaterial surface charge and reservoir brine composition. Two sandstone outcrop rocks were considered, namely Keuper and Berea. Two surface modified silicon dioxide particle samples with different surface modifications and reservoir brine to account for the effect of divalent cations were used. Further, various methods were developed to characterize the nanomaterial effects, together with building and calibrating devices and setups.

Note that a better understanding of nanoparticle adsorption aids the design and use of nanoparticles in various ways. It provides the decision makers with a better estimation of the required volumes of nanoparticles for a certain application. With a comparatively high price of this new and specialized technology this information is crucial to optimize project economics. Additionally, formation or equipment damage due to interaction can be mitigated.

Overall, the objectives of this work can be summarized as:

- Assessing rock sample characterization by means of routine core analysis, particle size distribution, Brunauer-Emett-Teller (BET) and zeta potential experiments.
- Evaluation of fluid-fluid interaction using compatibility test between nanomaterials and brine salinity.
- Define the impact of nanoparticles in the sorption process by ultraviolet-visible (UV-Vis) spectroscopy.
- Evaluate nanomaterial and rock interaction using static batch sorption experiments.
- Define the effect of nanomaterial on reservoir rock through single-phase core floods.

Experiments were comprised of batch sorption experiments and single-phase core flood experiments. In the batch sorption experiment crushed rock samples were mixed with various solutions of nano fluids in brine. The supernatant was investigated for a change of nanoparticle concentration, providing indications like which rock type, brine and temperature will support/ prevent adsorption.

Sorption was evaluated using UV-visible spectrophotometric absorption for nanoparticle concentration in the batch sorption experiments and effluents of the core flood experiments. Porosity and permeability have been measured before and after core flooding in order to investigate pore plugging. Scanning electron microscopy (SEM) was used to analyse which minerals the nanoparticles preferentially attach and to look at plugging effects. Flow Field Flow Fractionation (FFF) was used to investigate the size distribution of nanomaterials before and after core floods. In the core flood effluent, FFF was used to evaluate shifts in size distribution after interaction with the rock. Surface charges of the particles and rocks, by means of zeta potential, were used to analyse the particle-rock interaction. Note, that simulation and derivation of a mathematical models to describe particle's adsorption is considered out of the scope of this work.

1.3 Milestones

The milestones included here are mainly activities that complement each of the work-packages, hence can be summarized as followed:

- Brine Characterization
- Nanomaterials compatibility with Reservoir brine
- Nanomaterial Characterization – Zeta potential, SEM, FFF, UV-Vis
- Rock sample characterization – routine core analysis (RCA), Streaming Potential
- BET experiments
- Static batch experiments in different sets
- Effluent evaluation of batch experiments - UV-Vis
- Single Phase core floods – permeability to brine before/after treatment
- Effluent evaluation of the core floods – UV-Vis, Ion Chromatography (IC), FFF
- Tracer Test evaluation
- Visualize adsorbed nanoparticles - SEM

1.4 Outline

This thesis is divided into six chapters. The focus of each of them is briefly as follows:

Chapter 1 explains the motivation behind this work and gives an overview.

Chapter 2 discusses fundamental principles that are helpful to understand the conducted work and discussion. It also reveals the state of the art in the application of nanotechnology in the oilfield.

Chapter 3 describes the experimental workflow and used materials and fluids.

Chapter 4 reveals the obtained results during this thesis and analyses them.

Chapter 5 summarizes the conclusions drawn in the course of this thesis.

Chapter 2 Theoretical Background

2.1 Formation Damage Mechanisms

To achieve optimal recovery of hydrocarbon it is essential to avoid formation damage at any point of the operation. The first fluids which interact with the reservoir are drilling muds, followed by cement and various completion fluids follow. Applying improved and enhanced oil recovery (IOR/EOR) methods could have negative impacts on reservoir producibility when wrongly designed. To some extent, the main damage mechanisms are similar in various processes. However, higher risk of complications exists due to the wider range of chemical composition and larger injection volumes compared to drilling operations. A clear understanding of reservoir minerology, petrophysical properties, pressure/temperature conditions, and stresses as well as reservoir fluid chemistry is necessary. Some of the possible formation damage can be replicated in the laboratory and assessed on rock cores (e.g., porosity / permeability). Some others are only visible at a reservoir scale via well logs and well tests (e.g., skin damage). Water cut and production rate are key performance indicators (KPI) for formation damage that might reveal damage introduced during a certain operation (Wood and Yuan 2018).

According to Wood and Yuan (2018), four general groups of formation damage mechanisms can occur. Biological damage dictated by bacterial contamination or introduction of nutrients might cause souring of petroleum fluids and corrosion of installed equipment. Chemical damage driven by interaction of fluids and formation resulting in erosion of the porous media or wettability changes. Erosion is caused by clay swelling, deflocculation of clays, dissolution of minerals and changes in wettability result in increasing water mobility. Mechanical damage defined by fines migration from external sources, bit grinding, perforation damage or through production. Thermal damage is defined by souring of fluids or mineral dissolution via introduction of higher temperatures as well as fractures caused by thermoelastic effects.

The main formation damage mechanisms in sandstone reservoirs caused by low salinity waterflooding are fines migration, particle swelling and swelling-induced migration (Mohan et al. 1993).

High water cut flow may lead to clay bridging and fines redeposition in pore throats. This effect can reduce permeability in a desired way by increasing the area reached by injection fluids. This increase in areal sweep is highly dependent on the minerology of the reservoir and the prevailing clay type (Wood and Yuan 2018).

2.1.1 Fines Migration & Pore Throat Blockage

Fines migration is the movement of naturally existing particles of the reservoir rock caused by high fluid shear rates. Fines can be formed by uncemented clays like kaolinite. Fines migration is predominantly a problem in clastic formations due to the higher concentration of transportable material. It can occur when the wetting phase of the reservoir is in motion as seen in Figure 2.1 for a water-wet formation. For oil-wet formations fines migration might occur immediately at the start of production, since the wetting phase is mobile from the beginning (Bennion 2002).

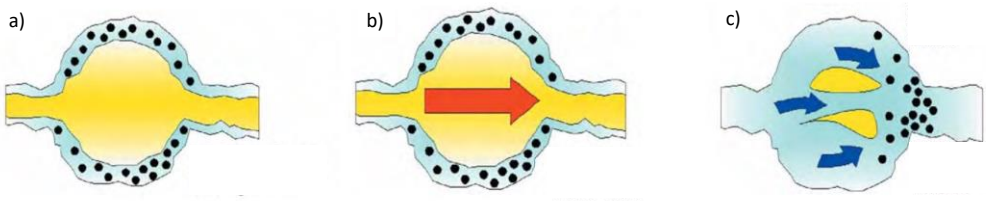

Figure 2.1: *Effect of wettability on fines migration in water wet rock: In most cases the rock and fines are water wet. When oil is produced fines are mobilized in a later stage of production: a) fines immobile in wetting phase (water); b) non wetting phase (oil) is mobilized - fines remain immobile; c) wetting phase mobilizes and fines migrate (modified after Bennion 2002).*

Fines migration can occur due to poor water quality, lack of subsurface definition, poorly managed surface facilities and inappropriate spacing between producers/injectors. The formation of precipitations due to incompatibilities is possible during stimulation, especially during acidizing jobs, if wrongly conducted due to incompatibilities. The consequence of fines migration and their deposition in pore throats is usually lower well injectivity seen as an increase in injection pressure. This results in an increase in pressure at surface which is coupled with higher surface facility requirements and therefore cost of operation. Production of fines and sand can also lead to operational problems such as erosion of downhole and surface equipment. Well clogging can additionally inhibit the production as well (Richard 2013).

2.1.2 Clay Induced Damage

Clay minerals are a group of phyllosilicates of less than 2 µm in their largest dimension, consisting of octahedral and tetrahedral sheets (Bergaya and Lagaly 2006). Octahedral sheets are formed by oxygen and hydroxyl anion groups with aluminum, iron and magnesium typically serving as the coordinating cation. Depending on the valency of their metal ions (e.g. Mg^{2+}, Al^{3+}) they form dioctahedral or trioctahedral minerals to balance their charges. Tetrahedral sheets are comprised of tetrahedrons of four oxygen atoms with silicon, aluminum and sometimes iron and boron atoms in the centers. These tetrahedrons are arranged in a hexagonal sheet. The tetrahedral and octahedral sheets are joined by shared oxygens or silicon atoms in 1:1 (tetrahedral-octahedral, TO, e.g., kaolinite) or 2:1 pattern (TOT, eg. illite) as seen in Figure 2.2. (Murray 2006). These clay mineral layers form clay mineral particles as seen in the bottom part of the figure. The layers are connected via non solvated cations, solvated cations or no interlayer particles.

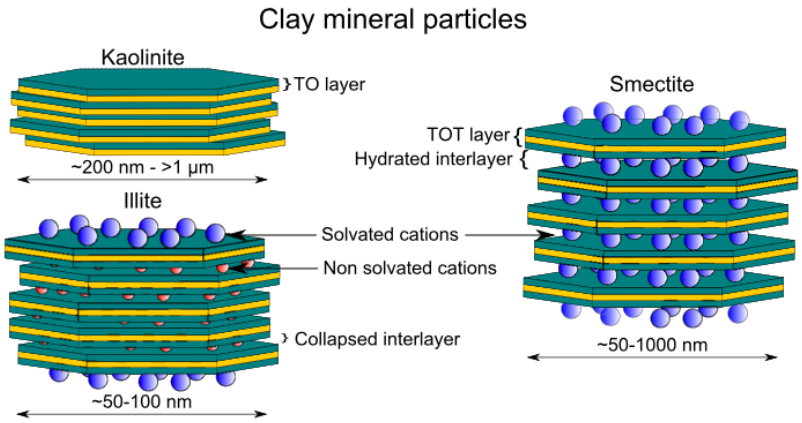

***Figure 2.2**: Clay mineral particles have a substructure that can be arranged in TOT or TO layers connected by interlayer cations (modified after Tournassat et al. 2015).*

Clay Swelling

When hydrophilic minerals like smectite (clay) contact fresh water or low salinity brine, they can expand causing severe permeability reduction. The problem is especially critical if the clay mineral coats the pore throats' surface, since small expansions can cause significant permeability reduction. Therefore, incompatible fluids that come into contact with swelling clays can cause major formation damage. Smectites like montmorillonite are among the clays with the highest swelling potential. The 2:1 structure is negatively charged and the presence of cations in the interlayer space neutralizes these charges. When in contact with cation containing fluids, these cations can be exchanged. The Cation Exchange Capacity (CEC) was defined, to evaluate the maximum quantity of cations a certain clay mineral has available for exchange for a given pH value. When polar molecules like water adsorb to the interplanar layers these layers start to expand. The fluid hereby has a considerable impact on the swelling capability – KCl causes for example less clay swelling compared to NaCl, for example (Pham and Nguyen 2013). Therefore, clay swelling can be inhibited by the use of KCl due to compression of the electrical double layer (EDL) and decrease of electrostatic repulsion between clay particles (Liu et al. 2004). Clay inhibition by the use of PEG coated silica nanoparticles was investigated by Pham and Nguyen (2013). Their work suggests that these nanoparticles reduced montmorillonite swelling in the presence of NaCl and KCl. The principle causing this effect is thought to be water displacement by adsorption of polyethylene glycol (PEG) to the clay surfaces. Potassium ions can stabilize PEG in the interlayer space and possibly explain these synergistic effects. NaCl seemed to cause the EDL to compress resulting in particle aggregation, for a detailed explanation of EDL refer to section 2.3.2.

Two types of clay swelling can be defined depending on type and concentration of cations in the aqueous solution, crystalline/microscopic and osmotic. Crystalline swelling typically occurs in high (saline) brine conditions with dissolved divalent or multivalent ions. Ions present in the interlayer space get hydrated and form hydrogen bonds to the oxygen atoms on the clay surface. A monomolecular water layer is formed between the clay layers causing the swelling process. Crystalline swelling is associated with minimal size expansion and the overall particle morphology is usually preserved. Conversely, osmotic swelling occurs in dilute solutions or in the presence of large

quantities of sodium ions (Na^+). The sodium ions allow the formation of an electric double layer on the surface of clay minerals, creating repulsive forces between platelets. This results in an increase in the interlayer spacing and up to 20-fold volume increase. Osmotic swelling occurs when the solution is below the critical salt concentration (CSC) and crystalline swelling above it (Pham and Nguyen 2013).

Clay Particle Release

In addition to osmotically swelling, a reservoir rock's permeability can be reduced due to the release of clay particles from the pore walls if the salinity of a permeating fluid is below the CSC. These clay particles can block the pore throats. Above this threshold no clay particle release occurs. CSC only occurs when monovalent cations decrease with an increased ion exchange affinity of the clay for the counterion. Critical salt concentration (CSC) depends on the temperature according to the Dejaguin-Landau- Verwey-Overbeek (DLVO) theory describing the colloidal stability (Khilar and Fogler 1984). DLVO theory is described in detail in section 2.3.1.

Clay Deflocculation

Deflocculation is caused by pH or salinity shocks or an abrupt change in divalent ion concentration. This causes a disruption of electrostatic forces holding clay platelets together. Kaolinite is an example for a clay that can be deflocculated (Bennion 2002).

2.2 Fluid Types used in the Reservoir Rock

Over the life of a wellbore and reservoir it is piercing into, a variety of fluids are used and come into contact with the formation. To avoid potential damage and a reduction in oil or gas production, meticulous attention has brought to the fluids intended to be used to guarantee compatibility is given.

2.2.1 Drilling Fluids

Drilling fluids can be classified as oil based, water based or pneumatic (air/foam/gas) fluids. These fluids are pumped down inside the drill string, then exit through the bit, hence pumped up to the surface through the annulus. On the surface the mud is cleaned via the shale shaker and centrifuges to remove cuttings and fines. A special variant are reservoir drill-in fluids (RDF) which are specifically designed to cause as little formation damage in the pay zone as possible (Szczygieł 2019). The purpose of drilling fluids is controlling the formation pressure and providing wellbore stability and well control. Additionally, it is used to seal off permeable zones, provide cooling and lubrication for the bit, inhibit corrosion and transmit hydraulic energy to downhole tools (Williamson 2013). Providing the correct hydrostatic-pressure at all times is fundamental for safe operations to avoid hole collapse or influx into the wellbore. Furthermore, the drilling fluids have to bring the rock chips produced by the drill bit back to the surface. To carry the cuttings even when the mud pumps are switched off and no flow is occurring the mud needs to possess thixotropic properties. By design the viscosity increases during static conditions. Once the fluid comes to rest the gel structure of the fluid is developed and the particles are kept in suspension. Additionally, the fluid shall be shear thinning to reduce friction. The typical rheological behavior of drilling fluids is described best by the Herschel - Bulkley model as seen in Figure 2.3.

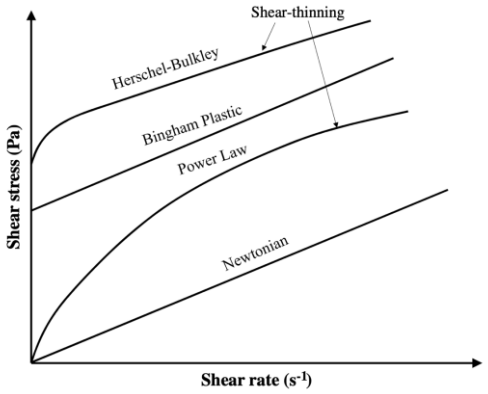

Figure 2.3: *Shear stress versus shear rate relationships of various rheological models. For drilling fluid a behaviour similar to Herschel-Bulkley is desired, since there at low shear rates (at a pump standstill) cuttings are prevented from settling, but at higher shear rates the viscosity does not increase dramatically and therefore reduce pump requirements (Deng et al. 2020).*

To reduce corrosion the pH of the fluid is controlled by adding lime ($Ca(OH)_2$), caustic soda (NaOH), sodium carbonate (Na_2CO_3) and sodium bicarbonate ($NaHCO_3$) To prevent bacterial growth after contamination bactericides are used. Filtrate reducers are used to limit the volume of fluid loss into the formation. The used additives are usually bentonite, lignite or CMC. Sodium bentonite forms a compressible filter cake from platelets to seal off the wellbore. Great care has to be given when this additive is mixed with clay swelling inhibitors: These also prevent the hydration of sodium bentonite clay and might create fluid loss problems. Therefore, it is advised to pre hydrate the sodium bentonite clays in fresh water before adding it to the mud.

When drilling through highly permeable sandstone or fractures a sudden fluid loss might occur. Since the drilling fluid is vital to provide well control this can have hazardous consequences. Therefore, to seal off the wellbore lost circulation material is used (Oilfieldteam). Note here, that these additives are much bigger in size compared to the clays that provide the usual filter cake. For size comparison, sand grains are 10^{-4} m, colloid particles 10^{-6} m and Nanoparticles 10^{-8} m (Zhang et al. 2015).

Surfactants are used to reduce surface tension between two different substances. Their molecular structure combines solubility in one medium on one end and solubility in the other medium on the other end. Soaps are typically a surfactant example, their molecule's hydrophobic side is attracted to debris/oil, whereas the hydrophilic attracted to water. The surfactant molecules therefore encapsulate particles and form a hydrophilic layer on the outside. This layer mobilizes the particle in the water. In the oilfield these chemicals are used to change the colloidal stability or dispersions to provide controlled flocculation. Particles are not repelling each other as strong and therefore form aggregates. These aggregates then have a higher mass and are easier to separate out. The used chemical additives for this process are usually gypsum, soda ash, sodium bicarbonate, sodium tetraphosphate or acrylamide polymers. These compounds form surfactants when e.g., reacting with oil. Additionally, they are used as emulsifiers, wetting agents and defoamers (Oilfieldteam).

2.2.2 Cement

Cement mainly protects the casings that link reservoir fluids to surface, being critical for a long stable and productive operation. The cement supports the casing, hydraulically isolates formations to prevent flow from high – pressure to low-pressure formations and protect the casing from corrosion. In the challenging operating environment, it also needs to protect shallow aquifers during/after drilling and being cost efficient. A good combination of slurry properties (e.g., rheology, fluid-loss, etc.) and mechanical properties of the set cement (e.g. porosity, permeability, etc.) is required. Once the drill string is removed from the open hole wellbore, the casing string is lowered. In the cementing process a sequence of various fluids is used, namely Preflush and cement slurry. The cement slurry is pumped down to inside the casing string to fill the annular space between casing and borehole wall as seen in Figure 2.4 (Lavrov 2016).

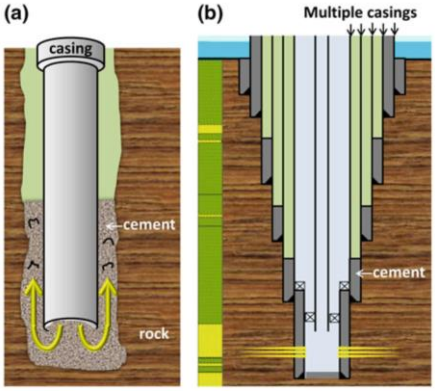

Figure 2.4: *Schematic illustration of a) cementing operation and b) finished well after cementing and perforation. During the cementing operation (a) the cement is pushed down the inside of the casing until it exits and fills the annular space between the steel pipe and the rock. Then the next section can be drilled with a smaller size bit on the inside of this section. Multiple casing strings are placed in succession to form the finished well (b) (Lavrov 2016).*

It is critical to maintain the pressure in the annulus between pore pressure and fracture pressure and depths of the open hole section at all times. If the annular pressure is below the pore pressure of the formation, fluids can enter the annulus which could lead to a blowout. If cement slurry density or the equivalent circulating density (ECD) exceed the formation fracture pressure the annular fluids can exit the borehole into the formation. ECD is the density equivalent of a hypothetical static slurry that exceeds the same hydrostatic pressure to the formation as the pumped slurry at a given pump rate. This added pressure is created by frictional forces and therefore depends on the fluid rheology and the flow rate (Boisnault et al. 1999).

Oilfield cement differs from concrete used in the construction industry: Concrete is a mixture of cement with solid particles, whereas cement in the oil field use is a pure binding material. Dry cement is produced by pulverizing and heating raw materials such as calcium oxide, silica, aluminum and iron) to a clinker. Clinker consists of 50-70% alite (Ca_3SiO_5) 15-30% belite (Ca_2SiO_4) 5-10% aluminate ($Ca_3Al_2O_6$) and 5-15% ferrite (Ca_2AlFeO_5). This clinker is mixed with gypsum to control solidification time – the time necessary for the cement to harden and develop its compressive strength. Usually the water-to-cement ratio by mass is 0.3-0.6 and the reaction of Portland cement with water

creates heat since it is an exothermic reaction. This reaction can be accelerated by increase of the alite content, finer dry cement and better mixing of the raw materials (Lavrov 2016).

2.2.3 Completion & Workover Fluids

Completion fluids are used during drilling or remediation or a well. These completion operations are perforation of the casing, tubing and pump setting and cementing the casing. During workover operations such as removal of tubing, replacement of equipment or cleaning out deposits, workover fluids are used. Both types of fluid are used to provide well control and prevent the well from collapsing. To minimize damage to the formation specifically designed fluids are utilized. Filtration losses and solids invasion can be minimized by operating near balanced conditions. In an overbalanced state, the pressure inside the wellbore is higher and the fluids are designed to seal off perforations temporarily. In an underbalanced situation the fluid exerts a lower pressure and therefore needs to prevent solids form the formation entering the wellbore. These sealing properties have to be temporary, since the goal is to eventually remove the barriers eventually to create a pathway for reservoir fluids to enter the wellbore with minimal obstructions. Therefore, sized salts are used in saturated water systems. These salt platelets seal off permeable zones by plugging the pores. These bridging agents are preferred, because they can later be dissolved by a low salinity water flush. Salts used for this are potassium chloride (KCl), sodium chloride (NaCl), calcium chloride ($CaCl_2$) and many others (Fink 2015).

2.2.4 Injection Fluids

Oil recovery is usually divided into three categories. During primary production the hydrocarbons rise naturally to the surface or get lifted by artificial lift devices such as pumps. Secondary recovery uses water and gas injection to maintain an elevated pressure in the reservoir. This pressure displaces the oil or gas in the reservoir and drives it to the surface. Waters used for this injection are usually low salinity brines. These two production steps can leave big amounts of hydrocarbon in the reservoir. To further increase the production tertiary recovery is applied. Thermal recovery introduces heat into the reservoir by steam. This lowers the viscosity and enables the fluids to flow. Chemical injection introduces long-chained polymers to increase the viscosity of injected waters. This increases efficiency of waterflooding operations. Surfactants are used to lower the surface tension and enables an easier flow of hydrocarbons (Sandeep, Jain, and Agrawal 2020; Fanchi 2002).

2.3 Surface Chemistry

A colloidal system is formed when matter of gas, liquid or solid state is finely dispersed in a medium. Repulsive forces between particles must be sufficient to keep colloidal stability. Otherwise, aggregates of increasing size are formed that alter the fluid's properties and might sediment due to gravity. This flocculation can be reversed, however if aggregation is too far advanced the aggregate's density increases in an unreversible process called coagulation (Khoshnevisan and Barkhi 2015).

2.3.1 DLVO Theory

The DLVO Theory, named after B. Derjaguin, L. Landau, E. Verwey and J. Overbeek, describes the forces of interaction between particle surfaces. According to this theory, the stability of electrostatically stabilized colloidal suspensions depends on the total energy potential between particles V_T.

$$V_T = V_A + V_R + V_S \qquad 2.1$$

V_A is the attraction potential between particles caused by London forces, V_R is the repulsion potential between particles due to the electric double layer and V_S is the potential energy as a function of solvent. V_A and V_R are much stronger than V_S and act on greater distances. If repulsive forces are strong enough to separate the particles far enough, Van-der-Waals attraction cannot dominate, and the suspension is stable. However, due to Brownian Motion the particle's kinetic energy is higher and can overcome repulsive forces. Therefore, a stable mixture might flocculate or coagulate when the temperature is increased (Lauth and Kowalczyk 2016).

The attraction potential V_A between two spherical particles of radii R_1 and R_2 in separation distance D is:

$$V_A = -\frac{A_c}{6D} \cdot \frac{R_1 \cdot R_2}{R_1 + R_2} \qquad 2.2$$

where A_c is the Hamaker constant. The repulsive potential V_R is defined as the following:

$$V_R = 2\pi\epsilon R\zeta^2 e^{-\kappa D} \qquad 2.3$$

Here, ϵ is the dielectric constant, R is the particle radius and ζ is the Zeta-Potential. The Debye-length κ^{-1} is a function of the electrolyte and described in more detail in the following (Lauth and Kowalczyk 2016).

2.3.2 Electric Double Layer & Zeta Potential

Zeta potential describes the charging behavior at interfaces with the latter being either solid-liquid, liquid-liquid (emulsions) or gas-liquid (foams). This work focusses on solid-liquid interactions, using the model of the electric double layer (EDL) to describe the charging behavior. Figure 2.5 shows a negatively charged particle in an electrolyte.

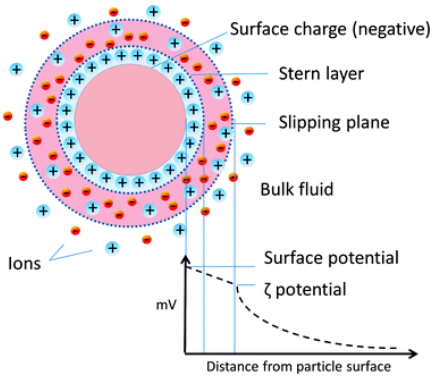

Figure 2.5: *Layer succession according to Bockris-Müller-Devanthan model: A charged particle is surrounded by the stern layer and a diffuse layer. The graph shows the surface potential as a function of distance from particle surface (Herrada García et al. 2014).*

Since the particle has a surface charge, the liquid that surrounds it reacts with it and generates a distinctive surface charge distribution. Coions (ions of the same charge) to the surface charge will be naturally attracted towards the particle and counterions will see repulsion. This results in a higher concentration of coions and lower concentration of counterions in the diffuse layer compared to the bulk solution. The charges of the ions balance the charge of the particle's surface. The rigidly associated layer of counterions and this diffuse layer form the EDL. When the particle moves in the solution the inner layer is so strongly associated with the particle, that it stays attached. The boundary where liquid is not strong enough attached to the particle to be following it is the shear plane. The same principle is applicable for charged solid surfaces where a solid stationary layer is present. The shear plane marks the border, from whereon ions are mobile in the diffuse layer (Luxbacher 2014, Miller 2019).

The electrical potential is a function of distance from the particle surface. Its behavior can be seen in Figure 2.5 and in Figure 2.6 in detail. The electrical potential can be described as the energy necessary to bring an oppositely charged elemental charge to the surface of the particle. It is an indication of the repulsive force as a function of separation distance (Miller 2019).

The zeta potential is the electrical potential measured at the slipping plane of a suspended particle under an electrical field (Carvalho et al. 2018). The pH value strongly affects zeta potential and it reveals the isoelectric point - the pH at which the liquid is assumed to have a zeta potential of 0 mV. Since the zeta potential is defined as the electric potential at the shear plane between the stationary and the diffuse layer, it depends on the ionic strength I – a measure for charge concentration (Miller 2019):

$$I = \frac{1}{2}\sum_{i=1}^{n} c_i \, z_i^2 \qquad 2.4$$

where c_i is the molar concentration [mol l^{-1}] and z_i is the charge number of ion i. Stronger valent ions therefore cause a higher ionic strength at the same concentration. With increasing concentration, the zeta potential decreases because the EDL is compressed at higher ionic strength. The double layer thickness is described using Debye-length κ^{-1},

$$\kappa^{-1} = \sqrt{\frac{\varepsilon_0 \varepsilon_r k_B T}{2 N_A e^2 I}} \qquad 2.5$$

where ε_0 is the vacuum permittivity, ε_r is the dielectric coefficient of the liquid, T is the absolute temperature, k_B is the Boltzmann constant, N_A the Avogadro number and e the elementary charge (Miller 2019, Lauth and Kowalczyk 2016).

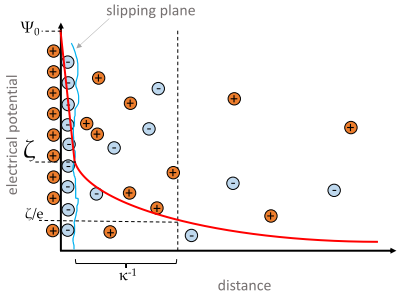

Figure 2.6: *Electrical potential as a function of distance from the surface of a charged particle (modified after Miller 2019).*

The double layer thickness 1/κ is defined as distance where the electrical potential is 1/e of the initial potential. It is a function of concentration and ionic strength. For an aqueous solution at room temperature this allows to calculate the double layer thickness as (Miller 2019):

$$\kappa^{-1} = (1.8 \cdot 10^{16} \cdot I)^{-0,5} \qquad 2.6$$

High ion concentration and ionic strength causes rapid decay in the electric potential and a thin double layer and weaker repulsion. This can ultimately lead to particle aggregation. Generally, a dispersion can be assumed to be stable if its zeta potential is above 25 mV for unmodified nanoparticles (Miller 2019).

2.3.3 Formation of Surface Charges

Surface charges can be formed by acid-base reactions or the adsorption of water molecules. In acid-base reactions pH of the aqueous solution is the driving factor. In a high pH more acidic groups will dissociate and remain negatively charged in the solution (see Figure 2.7). Conversely, in a very low pH solution the pronation of basic groups will be enhanced (Luxbacher 2014).

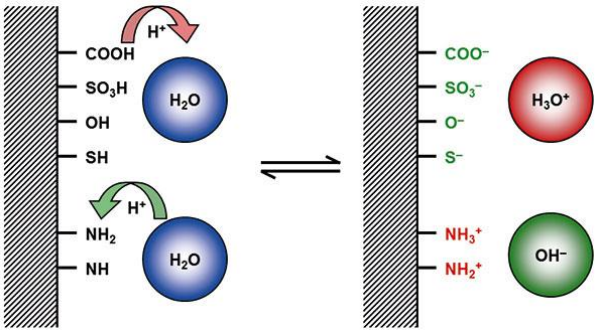

***Figure 2.7**: Charge formulation at solid-liquid interface with acidic (left) and basic (right) functional groups (Luxbacher 2014).*

Surfaces without functional groups cause charge formation by adsorption since they behave hydrophobically. Water molecules near the surface either form hydronium (H_3O^+) ions or hydroxide (OH^-) ions. In this type of charge formation also pH plays a major role. In general, the zeta potential at the solid-liquid interface depends on the properties shown in Table 2.1 (Luxbacher 2014).

***Table 2.1:** Properties affecting the Zeta potential at solid – liquid interfaces.*

Liquid properties	Solid properties	Others
pH value	Size	Measuring time
Ionic strength	Porosity	Temperature
Additive concentration	Electric conductance	Material
	Surface roughness	

2.3.4 Measurement of Zeta Potential of Solid Surfaces

Charged solid surfaces surrounded by an electrolyte react similar to the case with suspended particles. Determination of the zeta potential of these solid surfaces is conducted by measurement of the streaming potential as seen in Figure 2.8. An aqueous solution in a capillary forms a surface charge that is compensated by ions of opposite charge (counterions). When the solution is forced to move through the capillary these counterions are moved with the flow. Hence, a charge separation between inlet and outlet is generated that leads to an electrical potential difference which can be measured (Luxbacher 2014). This so-called streaming potential strongly depends on volume flow rate, ionic strength and size of the capillary.

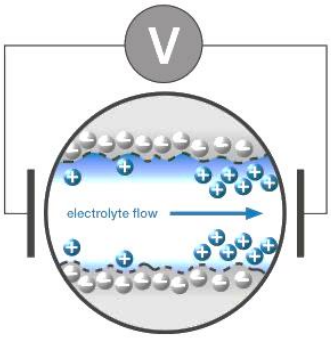

Figure 2.8: *Streaming potential measurement: Electrolyte flow in a capillary channel generates a measurable charge separation that can be measured as an electrical potential (Anton Paar).*

2.3.5 Measurement of Zeta Potential of Nanoparticles

To measure the zeta potential of nanoparticles in suspension electrophoretic light scattering is used. Electrophoretic mobility is the phenomenon that explains why charged particles move when an electric field is applied to the suspension. This principle allows the measuring of zeta potential of nanoparticles, an electric field is applied to the suspension and a laser beam is focused onto it. This laser beam will be scattered by the particles creating Doppler shifts, depending on the velocity of the particles. The sum of the particles creates an intensity of scattered light, that varies over time. Analysis of the scattered light spectrum allows a conversion from Doppler shift frequencies to a velocity distribution. Knowing the electrical field an electrophoretic mobility distribution and a zeta potential distribution can be calculated, known as Laser Doppler Electrophoresis (LDE). Later in the 1980s Phase analysis light scattering (PALS) was developed to overcome LDE's limitations in high salinity solutions. Higher electrolyte concentrations cause undesired effects such as heating or bubbles on the electrode's surface that prevent a reliable measurement by LDE. Above an ionic strength of $10 \cdot 10^{-3}$ M PALS is recommended to be used (Miller 2019).

2.4 Nanomaterials

Over the recent years more and more scientific interest has been generated for the application of nanotechnology and nanoscience. Research has covered the design, characterization, production and optimal application of materials and substances in a size of 1-100 nm. Their small size provides higher surface to volume ratio and therefore higher reactivity with other molecules. The use of nanotechnology enables processes to be more economical and sustainable. In this section different studies and applications in exploration, drilling, production, processing and enhanced oil recovery (EOR) are covered (Ledwani and Sangwai 2020; Sandeep, Jain, and Agrawal 2020 and Fakoya and Shah 2017).

Nanoparticles are used due to their small size which allows them to flow freely hopefully without getting adsorbed. They have been utilized as stabilizers, to improve mobility of hydrocarbons, formation and stabilization of emulsion, form drilling fluids, wettability alteration for improved oil recovery (IOR). The term '*nanofluid*' is used when base fluids (oil, gas or water) include colloidal suspensions of nanoparticles.

Materials that have nanoparticles embedded into their structure are also called *'nanomaterials'* (Fakoya and Shah 2017).

The oil industry has focused are mainly silica nanoparticles (SiO_2) due to economic reasons, however research includes many other nanomaterials have been developed and studied already. Alomair, Matar, and Alsaeed (2014) for example described the use of SiO_2, NiO, TiO_2 and Al_2O_3 particles in EOR. Their diameters are smaller than the pore throats of thief zones and could therefore improve the flooding potential without reducing permeability. This effect is achieved by an increased area of fluid contact by the driving fluid and an increased microscopic sweep efficiency.

The production of nanomaterials is usually conducted via one of six possible methods. Chemical/vapor deposition, plasma arching, electrodeposition, sol-gel synthesis, ball milling or the use of natural nanoparticles (Fakoya and Shah 2017). Among others Ledwani and Sangwai, 2020; Sandeep, Jain, and Agrawal, 2020; Fakoya and Shah, 2017; Liu, Jin, and Ding, 2016; Lashari and Ganat, 2020; Bera and Belhaj, 2016 as well as Kamal et al., 2017, provide a valuable overview over the work that has been conducted and existing literature.

Nanoparticle adsorption, which is a very relevant and important topic in nanomaterial application was covered in large extent by Petosa et al. (2010) and Zhang et al. (2015). Further, a more detailed description of the literature covering adsorption will be discussed.

2.4.1 Application of Nanotechnology in Upstream

Exploration

Nano sensors could be used for geo-exploration by seismic characterization, data interpretation and formation evaluation (Bera and Belhaj 2016). When nanoparticles are adsorbed to the surface of the reservoir rock their optical, magnetic or electrical properties can be utilized to use as nano sensors (Mogensen and Bennetzen 2014).

Since microbes in hydrocarbons possess special properties depending on their environment their detection can indicate certain reservoir parameters like pressure, temperature or salinity. Jahagirdar (2008) proposed the use nano optical fibers to detect these microbes. Later, Li and Meyyappan (2011) developed a technology for real-time monitoring of reservoir parameters based on this principle.

Oil water contacts, drive fluid and flood fronts can be detected using magnetic and superparamagnetic nanoparticles (Al-shehri et al. 2013; Rahmani et al. 2013).

In 2010 nano-robots were tested in a field trial for the first time by Saudi Aramco. These devices are injected with water, travel through the reservoir and brought back to the surface at producer wells to be analyzed. Liu, Jin, and Ding (2016) predicted nano-robots will be able to record, store and transfer data obtained on the path through the reservoir. This would allow a better detection of geological strata, faults and highly permeable pathways.

Drilling and Production

Lubricating Properties: Abdo (2014) investigated nano attapulgite to improve the tribological properties of drilling fluids. His work suggests, that this material can reduce the friction between the drill string and the wellbore and therefore the need for other expensive additives.

Filtration Control & Shale Inhibition: Fakoya and Shah (2017) suggested the use of nanofluids in drilling muds for their filtration properties. Poor drilling fluids form a thick mud cake which results in an increased force necessary to pull the drill string and consequently potential differential sticking. According to Fink (2015) iron oxide nanoparticles can reduce friction by adsorption to metal surfaces when using xanthan gum suspensions. Hoxha et al. (2019) investigated the subject of shale inhibition with nanoparticles as well.

Amanullah, Al-Arfaj, and Al-Abdullatif (2011) found that their used water-based nanofluids showed improved rheological properties compared to bentonite mud. The values for 10 s and 10 min gel strength were identical and in an API fluid loss test no spurt loss was observed. The produced filter cake was less than 1 mm thick suggesting a possible solution for above mentioned problem. Salih et al. (2016) also conducted experiments investigating rheological and filtration properties and suggested, that silica nanoparticles can replace oil-based mud in horizontal and shale drilling operations, however noted their pH sensitivity that may lead to flocculation problems. Bentonite-based drilling mud with sepiolite nanoparticles was studied by Al-Malki et al. (2016).

Sharma et al. (2012) showed that nanoparticle used in drilling fluid were able to reduce fluid invasion by 10-100 times. This greatly minimizes wellbore instability issues.

McDonald (2012) discusses potassium silicate-based drilling fluid to stabilize shales and control drilling time and costs. According to the work of Hoelscher et al. (2012) 5-100 nm silica nanoparticles minimize fluid loss when drilling in shale when used in water-based mud (WBM). Cai et al. (2012) used inexpensive, commercially available, nonmodified silica nanoparticles in WBM, bentonite mud and low solids mud. The particles with 7-15 nm in 10 wt% concentration reduce shale permeability and therefore reduce the interaction of shale with water based fluids. Xu (2012) studied the application of nanotechnology in gas drilling. The used solution carries reverse wetting agents to change the wetting properties of shales to prevent swelling. Additionally, the fluid reduces friction between the drill string and the borehole wall.

The use of bio polymer surfactant nanoparticles to enhance rheological and fluid loss properties was investigated by Srivatsa and Ziaja (2011). Their higher stability at elevated temperatures provided promising laboratory results for fluid loss reduction. Contreras et al. (2014) investigated filtration loss reduction with iron and Ca-based nanoparticles in permeable media at high pressure (~35 bar) and high temperature (~120°C). In a filter press test a reduction of filtration loss of up to 76% with these additives and up to 100% in combination with graphite was observed.

***Improvements for Cementing Operations**:* After the use of oil-based mud (OBM) for drilling a cleaning spacer slug has to be used. This is necessary prior to cementing to provide a clean surface on the outside of the casing for the cement slurry to bond to. Maserati et al. (2010) showed in an experimental study that nano-emulsions can effectively be utilized as spacer for cleaning and additionally reverse the wettability to provide a better bond between the cement slurry, the casing and the borehole wall. For a water droplet placed on a surface that was covered with OBM the used nano-spacers changed a water droplet's contact angle from 70° to approximately 0°. In a load test higher bond between casing and cement was achieved compared to conventional cement. Fink (2015) suggested the use of nano silica particles as accelerator for cement. In low temperature the slurry usually has a longer setting time which can be reduced since smaller particle size and a higher aspect ratio accelerates the hydration of cement. The use of nano sized clay for cement was investigated by Liu, Jin, and Ding (2016). The use of nano bentonite showed an improvement in compressive and tensile strength and a reduction of permeability of the set cement with by 29-80%. Nano montmorillonite and nano clay was therefore suggested as well-treatment fluid. Li et al. (2004) and Xu et al. (2011) investigated the use of silica, Fe_2O_3 and $CaCO_3$ nanoparticles to increase the strength of Portland cement.

Corrosion Inhibition: Nanomaterial's corrosion inhibition properties were tested by Jauhari et al. (2010) and Khabashesku (2016).

Enhanced Oil Recovery (EOR)

Enhanced oil recovery is a technique that involves the application of various additional methods to improve the recovery of hydrocarbons. Over the recent years nanotechnology has received greater attention in this discipline. Their ability to flow freely in the reservoir without getting retained allows a higher reservoir contact. In EOR pore throat plugging can be a desired effect: since nanoparticles can be adsorbed on the grain walls at pore throats, they increase a bulk pressure difference by narrowing the pore channel. This leads to an increase in drive fluid velocity and higher pressures, forcing trapped oil drops into the flow (Sandeep, Jain, and Agrawal 2020). Ledwani and Sangwai (2020) mentioned in his work the improved flooding potential without reducing permeability leading to better microscopic sweep efficiency. Ehtesabi et al. (2015) achieved an 80% increase of oil recovery in oil-wet sandstone using TiO_2 nanoparticles. 96% increase in recovery factor in field trial in a carbonate reservoir was found by Kanj et al. (2011) after the use of carbon based fluorescent nanoparticles.

The reason nanoparticles can cause the release of oil droplets that are trapped in thin pore throats are several effects such as wettability alteration, spontaneous emulsion formation and emulsion stabilization, change of interfacial tension (IFT) between reservoir fluids and change of flow properties of the porous medium as shown in Figure 2.9.

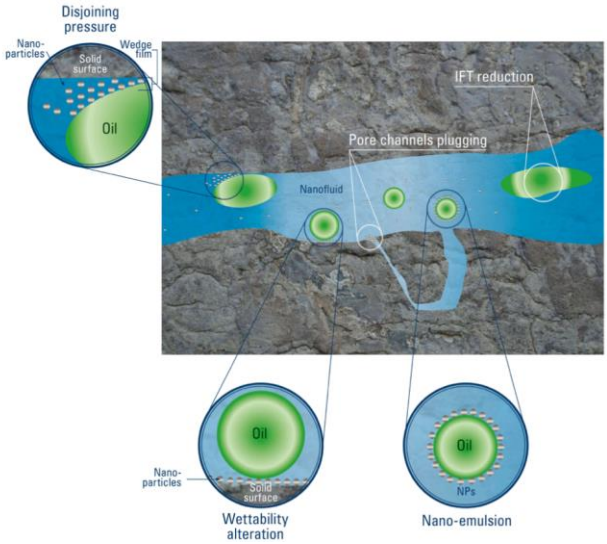

***Figure 2.9**: Nanofluids are utilized in EOR to obtain higher oil recovery by the following depicted effects: increase of disjoining pressure that leads to a wettability alteration, pore channel plugging, stabilization of emulsion and IFT reduction.*

Wettability Alteration due to Disjoining Pressure: Since wettability defines the fluid distribution in a reservoir its alteration greatly affects the release of hydrocarbon from a reservoir. Since NP are smaller than oil droplets and colloidal particles, they induce a low risk of being trapped in thin pore throats. This way they can access smaller pores and therefore a higher portion of the reservoir (Cheraghian, Rostami, and Afrand 2020).

According to Rostami et al. (2019) the additional hydrocarbon recovery is caused by an increased disjoining pressure. A thin film of nanoparticles is formed on the rock surface. This so-called wedge layer creates a disjoining pressure that acts on the discontinuous oil phase and helps separating an oil droplet from the water-wet surface. The driving force between this effect is an increased overall entropy by allowing the nanoparticles to form these microstructures on the solid surfaces (Wasan, Nikolov, and Kondiparty 2011).

Emulsion Formation & Stabilization: Nanoparticles have found to be suitable to stabilize emulsions to increase the recovery efficiency. Emulsions stabilized with nanoparticles have shown to withstand higher temperatures for longer periods of time (Sandeep, Jain, and Agrawal 2020).

IFT Reduction: Nanoparticles can reduce the IFT by creating a thin layer between the oil and injection fluids. With increasing nanoparticle and surfactant concentration the IFT and surfactant adsorption to the reservoir rock decrease (Cheraghian, Rostami, and Afrand 2020). Abhishek and Hamouda (2017) stated that this IFT reduction results in a better mobility and consequently in a reduction of fines migration.

Viscosity Increase: Viscous fingering in EOR processes results in poor sweep efficiency. Usually, polymers are added to the injection fluid to increase the viscosity, however these polymers degrade in HPHT conditions. Nanomaterials can overcome this limit and stabilize polymer solutions at elevated temperatures and salinities. Various studies covering this topic have been summarized by Lashari and Ganat (2020). 1% CuO nanoparticles added to CO_2-injection increased the viscosity by 140 times in the work of Shah (2009). This contributed in an 71% increase in heavy oil recovery.

Saleh (2020) investigated wettability changes due to nanomaterials and alkali in spontaneous imbibition experiments. The used nanoparticles resulted in 97.7%recovery of oil originally in place (OOIP) in combination with alkali. To further understand Saleh's results and gain a better knowledge of nanoparticle interaction with reservoir rock the same nanoparticles are investigated in various single-phase experiments in this work.

2.4.2 Unique Properties of Nanoparticles

Due to their high surface area to volume ratio, they are far more reactive compared to their base material. Their small size allows nanoparticles to travel into smallest pores and improve hydrocarbon recovery from thief zones. These zones are areas comprised of small pores that trap oil and treatment chemicals and are responsible for a large portion of hydrocarbon left immobile in the reservoir. Entrapment of injected chemicals also possibly creates formation damage which results in an undesired reduction in permeability (Sandeep, Jain, and Agrawal 2020).

An understanding on the formation of clusters is important, because these can be retained within the pore-throats of the porous media. With their large surface area nanoparticles tend to agglomerate quickly if they are not stabilized since this minimizes their surface energy. Nanoparticles in dispersion are subject to Brownian motion and therefore collide with each other. When a collision occurs, depending on the magnitude of attraction and repulsion forces the particles will form clusters or stay dispersed (Huh et al. 2019).

Colloidal stability can be provided by electrostatic stabilization, a stabilizing fluid or surfactant (depletion stabilization) or surface modification (functionalization) of nanoparticles. These methods are shown in Figure 2.10.

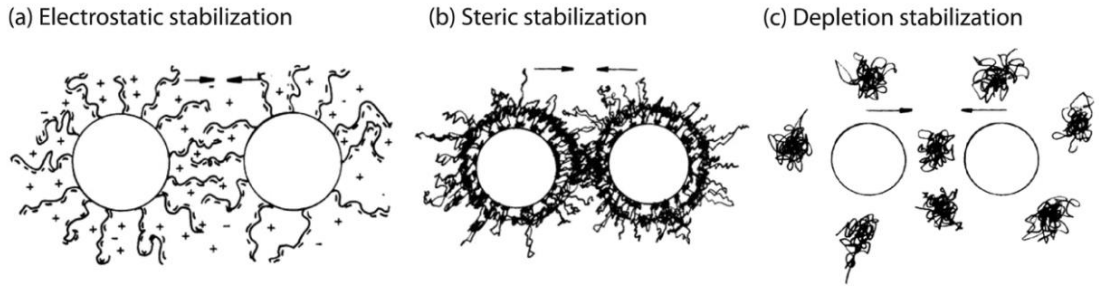

Figure 2.10: *Schematic of three methods to provide colloidal stability in a nanoparticle suspension: for electrostatic stabilization (a) ionic groups are absorbed to the surface of the nanoparticle and form a charged layer; b) steric stabilization is usually obtained by grafting macromolecules to the surface. These must be longer than the effective range of van der Waals forces to prevent attraction. In depletion stabilization (c) polymers are added to the solution that separate the particles (Huh et al. 2019).*

Electrostatic stabilization is achieved by the particle's repelling forces caused by their zeta potential as mentioned in section 2.3.2. This repulsion is weakened in the presence of dissolved salts in brines: electrolytes destabilize the particle dispersion by compression of the EDL. An increase in electrolyte concentration therefore reduces the energy barrier. Kinetic energy of the particles then surface charges dictate the probability of aggregation (Abhishek and Hamouda 2017).

2.4.3 Adsorption of Nanoparticles

Nanoparticles interact with the surrounding fluid, other nanoparticles and the rock surface in a porous media. These interactions are governed by static interaction, thermodynamic forces and hydrodynamic forces. Upon collision with rock, particles tend to stay in the stagnant points of the flow surface. The DLVO theory is used to predict van der Waals (vdW) attraction and EDL repulsion in this case. Since vdW repulsion is a function of separation distance it declines with increasing particle separation, however stronger attraction is observed with larger particles. The sum of these two interactions predicts the behavior of particles depending on the distance from the rock surface. Figure 2.11 shows the interaction energy of nanoparticles with Boise sandstone, where vdW attraction is dominant (Zhang et al. 2015).

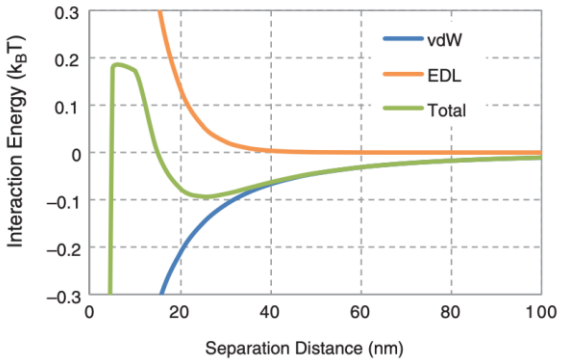

Figure 2.11: *Interaction energy curves between nanoparticle (-20 mV surface potential) and Biose- sand grains (-22mV zeta potential) in deionized water (Zhang et al. 2015).*

Electrostatic repulsion greatly depends on the surface potential and the ionic strength of the brine. Strong repulsion only exists in low salinity brine (10 mM / 0.051 wt% NaCl). In most injection brines the salinity and therefore the ionic strength is much higher and therefore the double layer repulsion might be negligible. Steric stabilization – polymer coating on the outside of particles – can provide enough repulsion to stabilize the dispersion in this case (Zhang et al. 2015). For the subject of this thesis, steric repulsion is the most important non-DLVO force, but others are magnetic forces for iron cased particles and hydration forces. When nanoparticles acre coated with hydrophilic functional groups, they can hydrolyze i.e., bind significant amount of water. These bound water molecules consequently play a role in particle interaction since they provide longer range of interaction compared to EDL forces, especially in solutions like formation brines with high ionic strength.

Electrical double layer interaction energy V_{EDL} (Eq. 2.7), steric interaction energy V_{st} (Eq. 2.8) and van der Waals interaction energy V_{vdW} (Eq. 2.9) can be calculated according to Petosa et al. (2010). These equations apply for particle-particle interaction between spherical particles of similar size and are added as additional terms to the total interaction energy stated in Eq.2.1.

$$V_{EDL} = 64\pi\varepsilon_0\varepsilon_r \frac{a_1 a_2}{a_1 + a_2}\left(\frac{k_B T}{ze}\right)^2 \Gamma_1\Gamma_2 \exp(-\kappa h) \quad 2.7$$

$$V_{vdW} = -\frac{A_{121} a_1 a_2}{6h(a_1{+}a_2)(1 + 14h/\lambda)} \quad 2.8$$

$$V_{st} = -\int_{\infty}^{h} 2\pi\left(\frac{a_1 a_2}{a_1 + a_2}\right)\left(\frac{k_B T}{s^3}\right)\left\{\frac{8l}{5}\left[\left(\frac{2l}{h}\right)^{\frac{5}{4}} - 1\right] + \frac{8l}{7}\left[\left(\frac{h}{2l}\right)^{\frac{7}{4}} - 1\right]\right\} dh \quad 2.9$$

Langmuir-Adsorption

According to Lauth and Kowalczyk (2016), Irving Langmuir's model is one of the most used ones to describe particle adsorption. It assumes that the surface of the adsorbent has a limited number of equal spots where particles can be bound. The probability of adsorption to a certain spot does not depend on the occupancy of neighboring spots. Furthermore, the reaction speed for adsorption depends on the pressure of the adsorbate and the number of free spots on the adsorbent. The adsorption ends when all spots are occupied in a single layer.

If nanoparticles are injected into a fresh sample of rock the thermodynamic force attracts nanoparticles to the rock surface. After continuous injection at some point equilibrium between nanoparticles in the dispersion and on the surface will be reached. The subsequent post-flush does not contain nanoparticles and the thermodynamic force is reversed. Desorption occurs and removes nanoparticles from the surface. Another force moving nanoparticles is the hydrodynamic force, which requires a minimum flowrate as soon as the particle hits an obstacle. The height of the obstacle and the size of the particle determine the minimal flowrate to remove particles. To allow nanoparticle removal the surface would have to be incredible smooth with asperity heights in the nanometer scale which is not the case on the surface of rock samples. The surface properties of the rock grains, vdW attraction are therefore the main contributors to nanoparticle adsorption. Therefore, the size of nanoparticles, surface coating and the rock lithology are defining factors (Zhang et al. 2015).

The maximum adsorption concentration $R_{monolayer}$ is equal to the mass of nanoparticles in a unit surface area and achieved when particles are densely packed in a hexagonal pattern. This number is also called the surface coverage,

$$R_{monolayer} = \frac{\pi}{3\sqrt{3}} d_p \rho_p \quad 2.10$$

where d_p is the particle diameter and ϱ_p is the density of the nanoparticles. In reality, repulsion between the particles causes them to fill only ~55% of this maximum and it also prevents a multilayer adsorption. Zhang et al. (2015) tested adsorption of silica and iron oxide nanoparticles with and without surface coatings and reported a range for maximum adsorption concentration between 10^{-5} and 10 mg/g (mg nanoparticle per g rock).

Zhang et al. (2015) also reported that increasing nanoarticle injection concentration resulted in higher irreversible adsorption. Their work also revealed, that higher clay content results in higher nanoparticle adsorption. The interaction between clay minerals and nanoparticles is weaker compared to sand grains, however due to the increased surface area due to the addition of clay minerals more nanoparticles are retained per mass rock. The adsorption per unit surface area is less if clay is present. Higher injection flow rate usually results in less adsorption. This indicates that the adsorption is not caused by size exclusion effects but physiochemical interaction since the particles have more residence time in the porous media. Once the excess nanoparticles have been removed during a postflush, the nanoparticle recovery in a second injection step was 100%. This suggests, that nanoparticles adsorbed in the first injetion prevented the adsoption of further nanoparticles during the second slug. This suggests that there is a finite number of irreversible adsorption sites on rocks. When nanoparticles from the effluent have been injected into a fresh core normal adsorption behavior was seen, suggesting that nanoparticles which were not adsorbed in the first injection are not different than others and can be adsorpbed once free spots are available.

Chapter 3 Materials and Methods

3.1 Materials

3.1.1 Core Plugs

The used rock material was outcrop rock from Berea and Keuper sandstone as shown in Figure 3.1. The material used for the batch adsorption experiment was crushed to a coarse powder. Samples consisted of homogeneous material of mixed grain sizes to ensure fine clay material was included as well. Core plugs were cut dry to avoid clay swelling.

Figure 3.1: *Berea (left) and Keuper (right) outcrop rock plugs were used in the experiments.*

Berea

Berea sandstone is a well sorted yellowish sandstone with approximately 87% quartz, 5% feldspar and 7% clay. The roundness is angular to sub-angular. The prevailing type of porosity is interparticle porosity, that has been reduced by growth of quartz. A SEM image of a thin section analysis from the same outcrop is shown in Figure 3.2. Pore walls are covered with feldspar or clay (Ladwein and Sauer 1986). According to the obtained XRD data, the clay is a mix of 92 % kaolinite, 7.5 % chlorite and 0.7% illite by mass.

Keuper

Keuper sandstone is a fine-grained red-brown sandstone with dark spots. The mineralogical composition is approximately 95% quartz, 1% feldspar, 4% mica. It is well sorted and mainly grain supported. The porosity is mainly interparticle porosity with a small fraction of solution porosity in feldspar. Frequently, pore walls are coated with Limonite and Kaolinite. Limonite is the iron oxide that causes the reddish color (Sauer and Phillipovich 1988).

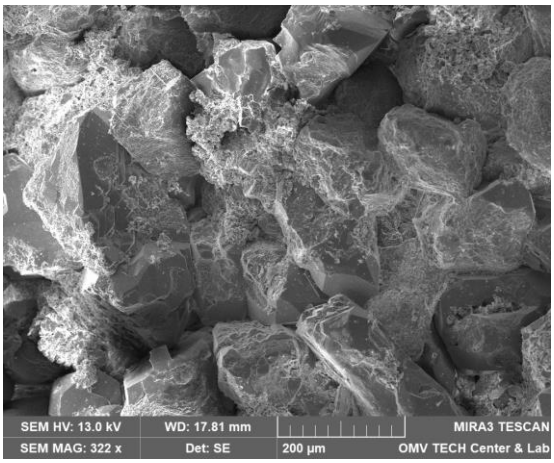

Figure 3.2: *SEM image of Berea. Quartz cement can be identified by its smooth surfaces compared to the sand grains. Kaolinite is placed between sand grains in its typical book-shape.*

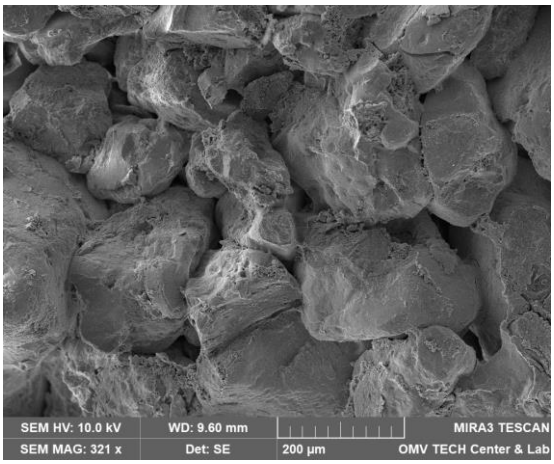

Figure 3.3: *SEM image of Keuper. The sand grains are more rounded compared to Berea, but a reduced amount of clay and quartz cement is visible.*

Keuper core plugs show higher permeability compared to Berea with similar porosity, however Berea is more homogeneous. Petrophysical data of the used core plugs is summarized in Table 3.1. Permeability k to nitrogen was plotted vs. porosity Φ in Figure 3.4. BET surface area measurements were conducted both on crushed material and core plugs and visible in Table 3.2. The used device was a *Micromeritics ASAP 2020*.

Table 3.1*: Petrophysical data of Berea and Keuper core plugs.*

	Berea		Keuper	
	Porosity Φ [%]	Permeability (N_2) k [mD]	Porosity Φ [%]	Permeability (N_2) k [mD]
Mean	21.92	485	23.54	1424
STD	0.121	32	0.794	172
Min	21.7	422	22.6	1285
Max	22.1	542	24.9	1742

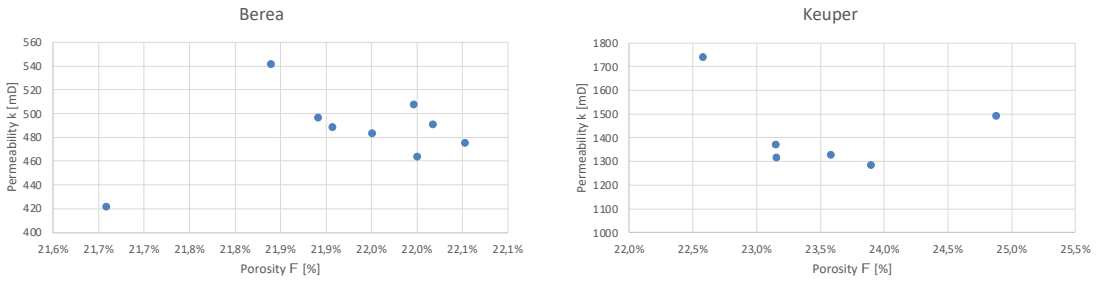

Figure 3.4: *Petrophysical properties of the used Berea (left) and Keuper (right) core plugs.*

The underlying theory is that gas molecules adsorb on the surface of a solid in layers. This differs to the previously discussed Langmuir adsorption theory, where only a single layer was assumed to be adsorbed. To measure adsorption, nitrogen is passing over the probe. Due to cooling via liquid nitrogen smallest reductions in pressure can be measured. By reduction of pressure the adsorbed nitrogen molecules desorb from the surface of the probe. The desorbed mass of nitrogen is in certain pressure ranges proportional to the surface area, which makes a measurement of specific surface area possible (Brunauer, Emmett, and Teller 1938).

As expected, the specific surface area of crushed Berea material is slightly higher compared to the core plug measurement. Touching grains are no longer attached to each other and more surface area of the grains is exposed. Each crushed material sample was taken from a mixture from approximately 700 g of crushed material, whereas the core plug measurements were repeated measurements on the same plug. The heterogeneity that was visible on Keuper could therefore explain the unexpected high surface area of the core plug measurement whereas the specific surface area of the crushed sample appears more representative. Measurements were taken at 60°C on crushed samples and core plugs and at 110°C on Berea core plugs to investigate the temperature effect. Higher temperature results in higher surface area.

Table 3.2: *Specific surface area measurements were conducted using the BET method for core plugs and crushed material.The similarity between the specific surface area of the crushed material underlines that the crushed material for both rock types was comparable in grain size.*

	Specific Surface Area (BET) [m²/g]	
	Berea	**Keuper**
Core plug (60°C)	1.4364	0.9896
Core plug (110°C)	1.6184	-
Crushed material (60°C)	1.5621	1.5645

3.1.2 Fluids

Brines

A softened injection brine, test water (TW) and a synthetic formation brine, formation water (FW) were selected to investigate the effect of divalent cations. Their composition and properties are shown in Table 3.3.

***Table 3.3**: Composition of synthetic brines test water (TW) and formation water (FW).*

	TW [g/l]	**FW** [g/l]
NaCl	18.960	19.750
$NaHCO_3$	1.850	-
$CaCl_2 \cdot 2\ H_2O$	-	0.400
$MgCl_2 \cdot 6\ H_2O$	-	0.660
NH_4Cl	-	0.170
pH (22.8°C)	8.46	6.53
Ionic strength [M]	0.346	0.373

Alkali Solution

The prepared alkali solution was 3000 ppm Na_2CO_3 in TW, hereafter, named *alkali solution* (AS). This concentration was selected, since it resulted in the highest emulsion stability and interfacial tension (IFT) reduction with 0.1 wt% nanoparticle concentration in preceding experiments by Neubauer et al. (2020). In a first step a 50000 ppm mother solution was prepared and subsequently diluted to create 3000 ppm concentration when mixed with the respective nanofluid. 3000 ppm Na_2CO_3 in TW was used as a background probe for the UV-Vis measurements, having a pH of 9.89.

Nanofluids

The used nanomaterials were in the form of dispersions of fumed silica nanoparticles. The dispersion does not have a high salt content but might have silanes in excess. The nanofluids differ in the surface modification applied to them and are hereafter called *NF A* and *NF B*. NF A contains PEG chains as surface modifications and showed to be rather unreactive during in house corrosion tests. NF B has two 2 diol groups grafted to the surface of the particles and showed higher corrosive potential. Their properties can be seen in Table 3.4. Measurements at room temperature were conducted at 22°C.

Transmission Electron Microscope (TEM) images (Figure 3.5, Figure 3.6) were provided by the manufacturer and show images of the modified particles. The loose agglomerates can break easily break apart, while the aggregates remain within dispersion.

Table 3.4: *Properties of Nanofluids (NF).*

	Nanofluid A	**Nanofluid B**
Density at 25°C [g/cm³]	$1.15 \pm 8 \cdot 10^{-4}$	1.14 ± 10^{-3}
Density at 60°C [g/cm³]	$1.13 \pm 2 \cdot 10^{-3}$	$1.11 \pm 4 \cdot 10^{-4}$
Solid content [%] *(loss on drying at 105°C)*	24.9	27.8
Viscosity at 10 1/s [mPas]	19	48
Viscosity at 100 1/s [mPas]	18	37
Particle size (d50) DLS [nm][a]	128	140
Particle size (d50) SLS [nm][a]	111	117
R_g [nm] [b]	60[c]	96[d]
R_{hyd} [nm] [e]	52	61
pH at 22°C [f]	$8.99 \pm 2 \cdot 10^{-2}$	$2.82 \pm 2 \cdot 10^{-2}$

a) measured in DIW
b) mean radius of gyration: online MALS, random coil model
c) particle size distribution 19-131 nm; D50 91 nm
d) particle size distribution 19-199 nm, D50 130 nm
e) mean hydrodynamic radius
f) measurement in triplets, SD $2 \cdot 10^{-4}$

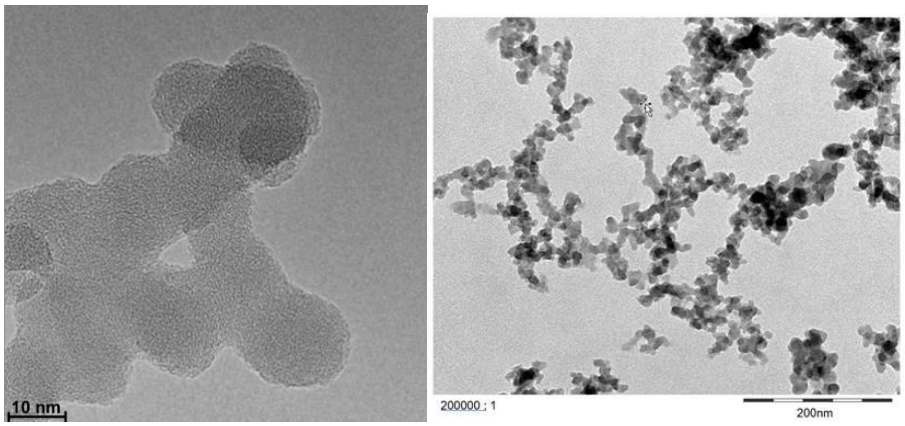

Figure 3.5*: TEM (left, 10 nm; right, 200 nm) images of unmodified silica nanoparticles.*

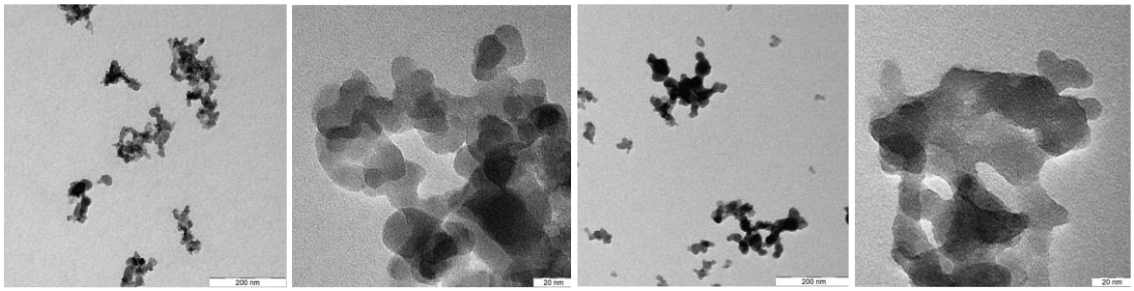

Figure 3.6: *TEM images of NF A (left) and NF B (right) in 200 nm and 20 nm.*

Zeta-Potential Titration

Zeta-Potential of the nanoparticle suspensions varies with pH as seen in Figure 3.7. These measurements were conducted by the manufacturer using a *3P DT-300* over the pH range 3-10. The device uses electroacoustic measurement of colloidal vibration current. An ultrasound pulse displaces suspended particles in the medium due to inertia caused by their density difference. The particles are moved relative to their diffuse EDL to form fluctuating dipoles. An alternating current – i.e. the colloidal vibration current - is generated that subsequently allows the calculation of zeta potential (3p Instruments).

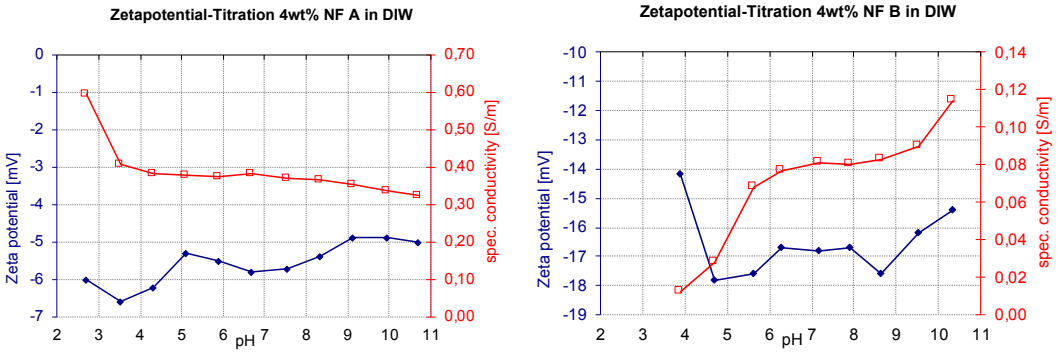

***Figure 3.7**: Zeta-Potential and specific conductivity for NF A and NF B.*

NF B is more negatively charged due to the polar functionality of its surface coating. This should result in better colloidal stability. As mentioned earlier, unmodified silica particles need a zeta potential of at least -25 mV to form a stable emulsion (Huh et al. 2019). In this case the surface modifications provide additional steric repulsion to keep the particles suspended, even with these apparently low zeta potential values.

Tracer

The selected chemical as tracer for the core floods was Ammonium Thiocyanate (NH_4SCN). Pre-emptive spectrophotometry tests showed influence of the tracer below 260 nm. Therefore, the selected wavelength for all interpretations of UV-Vis spectrophotometer data was 270 nm. 1000 ppm NH_4SCN solution was added to the brines to create a tracer concentration of 30 ppm in the nanofluid slugs. The effluent samples were eventually diluted by 1:3 and analyzed using Ion Chromatography (IC).

3.1.3 Chemical Combinations and Concentrations

To evaluate the fluid/fluid and fluid/rock interactions, the following concentrations and combinations were prepared as seen in Table 3.5. A mixture of FW and Na_2CO_3 was not used due to incompatibility found in earlier experiments resulting in calcium carbonate precipitations.

Table 3.5: *NF A and NF B were diluted in two concentrations each in TW and FW. The mixtures containing alkali were mixed in 0.1 wt% only. These pH measurements were performed in triplets and the standard deviation was ~2·10⁻².*

Brine	Fluid	Concentration [wt %]	pH (22°C)
TW	NF A	0.1	8.53
		0.03	8.56
	NF B	0.1	8.49
		0.03	8.55
FW	NF A	0.1	7.14
		0.03	6.96
	NF B	0.1	4.91
		0.03	6.16
AS	NF A	0.1	9.90
	NF B	0.1	9.87

3.2 Experimental Procedures

3.2.1 Overall Methodology

To evaluate the influence of nanoparticles on various rock types the following procedures were undertaken:

- Characterization of outcrop material
- Characterization of fluids
- Visual compatibility tests between brines and nanofluids
- Batch adsorption tests to investigate nanoparticle adsorption to crushed rock material
- Core floods on selected samples and analysis of effluent
- SEM imaging of nanoparticle treated cores to visualize adsorption preferences

3.2.2 Porosity

First the core plugs were cleaned using Soxhlet extraction and dried in a vacuum chamber at 60°C for several days. Porosity was measured using a Boyle – helium porosimeter (Figure 3.8) and mercury buoyancy.

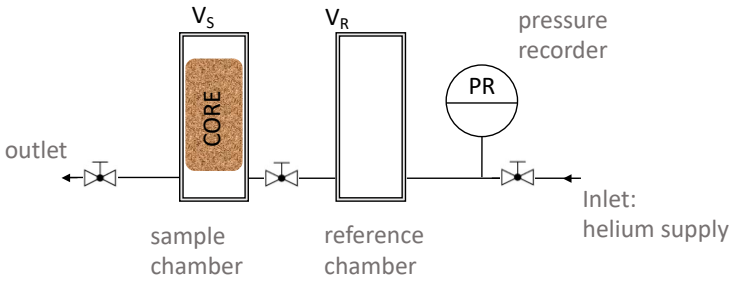

Figure 3.8: *A helium porosimeter was used to determine the porosity of the rock sample. First helium is filled into the reference chamber until a stable pressure was observed. Then all valves are closed and the valve between the two chambers is opened and a stable pressure recorded.*

The principle of measurement is, that the expansion of gas from the reference chamber with pressure p_1 into the sample chamber leads to an equilibrium pressure p_2. By knowing the reference volume V_R and the sample chamber volume V_S, the unknown grain volume V_{grain}, bulk volume V_{bulk} and porosity Φ can be calculated using the following equations:

$$V_{grain} = V_S - V_R \cdot \frac{p_2}{p_1 - p_2} \quad 3.1$$

$$V_{bulk} = \frac{m_{Hg}}{\rho_{Hg}} \quad 3.2$$

$$\Phi = \frac{V_{grain} - V_{bulk}}{V_{bulk}} \cdot 100 \quad 3.3$$

Mass in mercury m_{Hg} was obtained by submerging the core plug in a mercury bath and measuring the added weight.

3.2.3 Permeability

Permeability to gas was measured by mounting the core plug in a Hassler cell and injecting Nitrogen with a flowrate q of 400 – 800 ml min^{-1}. A differential pressure transducer was connected to the inlet and the atmosphere. Subsequently the permeability was calculated using the following Eq. 3.4 based on the Darcy equation and corrected for the Klinkenberg gas slippage effect:

$$k_{gas} = -\frac{q\mu l}{A\Delta p} \quad 3.4$$

3.2.4 Streaming Potential

Generally, for permeable material and irregular shaped samples like core plugs permeation mode is used. Here the brine is flowing though the core plug with increasing pressure differences. An electrical response is generated and reported as the streaming potential. This streaming potential is related to the zeta potential via the Helmholtz-Smoluchowski approach,

$$\zeta = \frac{dI_{str}}{d\Delta p} \cdot \frac{\eta}{\varepsilon \cdot \varepsilon_0} \cdot \frac{l}{A} \qquad 3.5$$

where I_{str} is the measured streaming current, η is the dynamic viscosity and $\varepsilon \cdot \varepsilon_0$ is the dielectric coefficient of the electrolyte solution. A and l are the cross section area of the core plug and its length (Luxbacher 2014). Further details to streaming potential measurements were discussed in section 2.3.4.

Cores were either pre-saturated in brine (aged) to obtain equilibrium prior to the measurement or measured directly with the respective brine (unaged). A flow with increasing pressures was set, flowing an electrolyte through the core that creates a measured electric potential. After a sufficient time period, the unaged cores are assumed to equilibrate until their zeta potential values would match the results from aged cores. Streaming potential values for Berea reached equilibrium for both brines between -14 and -17.5 mV. The values for unaged cores are assumed to be similar to these of aged cores a after sufficiently long time period. The results are presented in Figure 3.9. The device used for these measurements was an *Anton Paar SurPASS 3*.

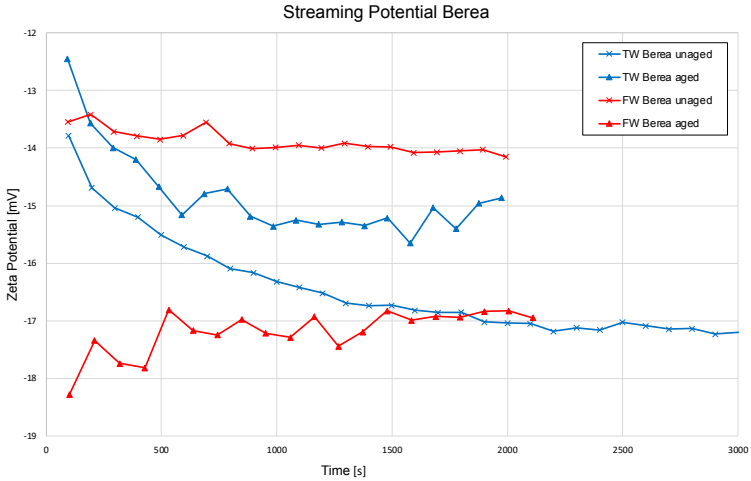

***Figure 3.9**: Streaming potential of Berea rock in different brines. The zeta potential values reach equilibrium between -14 and -17.5 mV.*

3.2.5 Density Measurements

An *Anton Paar 5000 M density meter* was used to measure fluid densities. The device uses the oscillating U-tube method: A fluid sample is electronically excited to vibrate at its characteristic frequency (Anton Paar). From this characteristic frequency the density of the fluid can be calculated. The densities were measured at 25 and 60°C in triplets and the respective average value was used.

3.2.6 pH Measurements

pH measurements were conducted using a *MU 6100 H Multi-parameter meter* with a *pHenomenal 110 pH* electrode. The electrode was cleaned with DIW and dried between measurements. The temperature of the measurements was RT, but noted with the respective measurement. Tests were conducted to verify that the used filters do not affect the pH measurements.

3.2.7 Particle Size Measurement

To separate the solids by size in the sample prior to the measurement, they were fractionated using an *AF2000 Flow FFF System*. Consequently, the samples were analyzed using a *PN3621 Multi Angle Light Scattering* (MALS) and a *PN3704 Dynamic Light Scattering* (DLS) system to measure particle size. Additionally, effects on particle size caused by the brine were investigated. Therefore, 0.1 wt% of each nanofluid was mixed with TW and FW and analyzed using a *Malvern Zetasizer*.

Field-Flow Fractionation

Field-Flow Fractionation (FFF) is a separation technique that use a forcefield to separate solids in suspensions in sizes from 1 nm to 100 μm. Hereby, the forcefield is applied perpendicularly to the fluid stream in the separation channel. Under the influence of a separation force (gravity, fluid flow, centrifugal force or temperature gradient) and the opposing diffusion field layers of sample size are formed. The laminar main flow in the channel forms a parabolic flow profile. Bigger particles are therefore placed in slower stream lines of the laminar flow inside the channel and smaller particles in the faster stream lines. Therefore, the smaller particles are transported faster through the channel and arrive the succeeding detection earlier than bigger particles. In Asymmetric Flow FFF (AF4) the force field used is a fluid cross stream inside the channel. This crossflow is separated from the main flow channel, directed through the main channel and though a semipermeable membrane (see Figure 3.10). This membrane allows the solvent to exit the side of the channel but provides a barrier for the solids. After fluid stream is fractionated by particle size, the measurement of particle size over time is conducted (Meier and Heinzmann 2017).

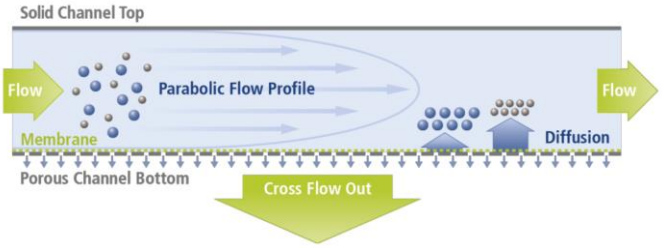

***Figure 3.10**: Principle of Asymmetric Flow Field-Flow Fractionation (Meier and Heinzmann 2017).*

Dynamic Light Scattering (DLS) & Multi Angle Light Scattering (MALS)

Suspended particles move in random thermal i.e., *Brownian* motion. A monochromatic light source illuminates the sample, which scatters the light onto a detector. The optical signal received on the detector undergoes random changes, due to the particle's movement (see Figure 3.11). The variation in the signal over time can be related to particle size, since bigger particles vibrate slower compared to smaller particles otherwise identical conditions (Horiba). The observed diffusion coefficient D_c allows the derivation of the hydrodynamic radius R_{hyd} via the Stokes-Einstein equation:

$$D_c = \frac{k_b T}{6\pi\eta R_{hyd}} \qquad 3.6$$

Particle diffusion depends on the absolute temperature T and the viscosity η of the fluid; k_B is the Boltzmann constant. The hydrodynamic radius R_{hyd} of a particle is the hypothetical radius of a solid sphere, that diffuses at the same rate as the particle including surrounding solvent molecules (Pusey 1974, Leszczyszyn 2012).

Static light scattering (SLS) a monochromatic light source is passing through the sample and scattered an angle θ. The angle of scattering allows the determination of the mean radius of gyration R_g. It is defined as the mass weighed average distance from the core of a molecule to each mass element in the molecule (Horiba). This can give information on the molecular weight, since the intensity of the scattered light is averaged over time (Carvalho et al. 2018). In this case multiple angles were measured using multi angle light scattering (MALS).

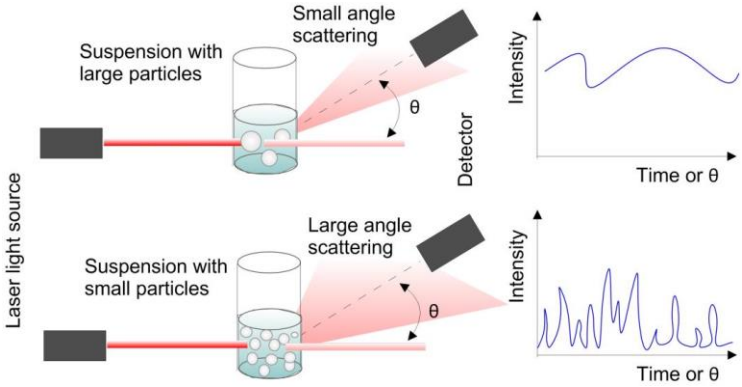

***Figure 3.11:** Static and dynamic light scattering: Lower variation in scattering intensity and small angle scattering for larger particles (Nikolova and Bayryamov 2019).*

3.2.8 Zeta potential Measurements

Zeta potential measurements in the respective brines were conducted using a *Malvern Zetasizer*. The solutions listed in Table 3.6 were measured with 9 repeats each.

***Table 3.6**: Zeta potential measurements in test water (TW) and formation water (FW) with and without sodium carbonate.*

Nanofluid	Concentration [wt%]	Brine	Na_2CO_3 [ppm]
NF A	1.43	TW	-
		TW	3000
		TW	7000
		FW	-
NF B	1.39	TW	-
		TW	3000
		TW	7000
		FW	-

3.2.9 UV-Vis Spectrophotometry

The device used for the measurements was a *Thermo Scientific Evolution 201* (Figure 3.12). It features a usable wavelength rage of 190 to 1100 nm in combination with a quartz QX 10 mm cuvette. The principle used by this device is that monochromatic light split into two beams and introduced into a sample and a reference filled with the solvent to be detected separately. Only light with certain wavelengths is extracted from the spectrum.

***Figure 3.12:** Thermo Scientific Evolution 201 (Fisher Scientific).*

The intensity I of the transmitted light from the reference is compared to the intensity of the incident light I_0 using *Beer's law* (*Eq. 3.7*) to define transmittance T_B. The transmittance is directly proportional to the concentration and thickness of an absorbing medium.

$$\frac{I}{I_0} = T_B \qquad 3.7$$

The *Beer - Lambert law* (*Eq.3.8*) correlates absorbance Abs with transmittance:

$$Abs = \log\frac{I}{I_0} = log\frac{100}{T_B} = \varepsilon cl \qquad 3.8$$

ε being the molar attenuation coefficient [$M^{-1}cm^{-1}$], c the molar concentration [M] and l the pathlength [cm]. This formula is only valid at single wavelengths and absorbance values > 0,8 should not be trusted (Biochrom). In this work the wavelength of 270 nm was chosen to use for all UV-Vis spectrophotometry measurements and the calibration. Both the influence of brine and the used chemical tracer in the core-floods led to this decision.

The cuvette was flushed twice with sample fluid and then filled. First, the device needs to have both cuvettes filled with the solvent to create a reference. This allows the device to calculate a comparison between the two sample holders. Then, the reference cuvette stays filled with solvent and the blank vail gets filled with the sample that has to be measured. The fluid in this blank vail was the respective solvent of the NP solution: either TW, FW or AS. This method deviates to the methodology Abhishek (2019) uses, as there all measurements are compared to the absorbance in deionized water (DIW). This methodology was tested as well by comparing TW, FW and AS vs DIW. The influence of the dissolved salts led to the decision, to use each respective solvent instead of DIW as a reference.

As a first step various calibration concentrations were mixed for all three brines. Then they were stored for 24 h and filtered using *0,45 µm MCA hydrophilic PTFE syringe filters* and their absorbance was measured.

Additional measurements were conducted to investigate various influencing factors:

- TW against DIW
- FW against DIW
- 3000 ppm Na_2CO_3 in TW against TW
- 30 ppm tracer in brine against brine
- Impact of various filters
- Solution age (instant, 10 d, 14 d)
- Impact of glass vs. plastic bottles at 22°C and 60°C
- device drift over time: repeated measurements over time
- Repeatability of measurements

3.2.10 Batch Sorption Experiment

The batch sorption experiment was used to determine the interaction of rock material with nanoparticles and brines in various combinations and conditions. Therefore, 5 g of both types of crushed rock material was mixed with 20 ml of each respective solution described in Table 3.5. Two samples of each combination were placed in a sample holder inside a heating cabinet at RT or 60°C. The sample holder was rotating the samples for 24 h at approximately 35 rpm. A schematic of the experimental setup is shown in Figure 3.13.

Figure 3.13: *A sample holder was mounted on an axis which was connected to an electric motor outside the heating cabinet. The samples were placed in the sample holder and rotated for 24 h at ~35 rpm at RT or 60°C.*

Subsequently, the samples were left resting for one hour for gravity settling (see Figure 3.14). Then the suspension was filtered with 0,45 µm MCA hydrophilic PTFE syringe filters. This method also varies from the work reported by Abhishek (2019), where liquids were separated using a centrifuge and filtered using a 0.22 µm filter. In theory, both gravity settling and centrifugal separation should only remove particle aggregates and rock particles and keep stable suspended particles unaffected. After the filtration pH and UV-Vis spectrophotometric measurements followed as described in section 3.2.6. and 3.2.9.

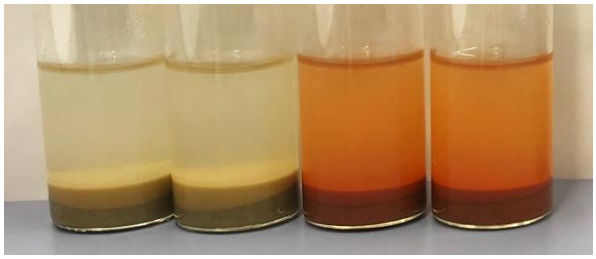

Figure 3.14: *Batch sorption samples after gravity settling. The glass bottles are filled with Berea (left) and Keuper (right) rock material and NF A in FW. After one hour resting time, the fluid was taken into a syringe and filtered to be analysed.*

3.2.11 Core Flooding

Permeability to Brine

The initial core flooding setup is shown in Figure 3.15. Brine and nanofluid were prepared and filled into piston accumulators. The core plugs were vacuum saturated in the respective brine for several hours and placed in a hassler cell. This was then mounted vertically inside a heating cabinet at 60° C and a confining pressure of 35 bar was set. Absolute and differential pressure sensors were used to measure the pressure differential across the core. A backpressure regulator was set to 5 bar.

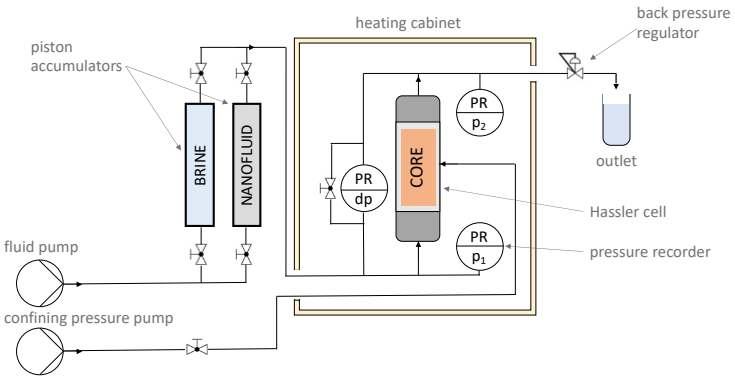

Figure 3.15: *Core flooding setup for permeability measurements. The core holder was placed vertically inside a heating cabinet and pressure sensors were fitted to record the pressure differential across the core. A confining pressure of 35 bar was used.*

To measure permeability to brine various flowrates were injected to perform a step rate test and the pressure response recorded. Then 60 ml 0.1 wt% nanofluid in TW was injected into the core with 0.325 ml/min. The injection of nanofluid and brine at 0.325 ml/min correlates to an interstitial velocity of 0.046 cm/min (2.2 ft/day) and a Darcy velocity of 0.21 cm/min (10 ft/day). After the first injection, permeability to brine was again measured by conducting a step rate test. The next injection was using 60 ml 1 wt% nanofluid in TW at 0.325 ml/min and a subsequent step rate test. This showed the potential effect of nanoparticle treatment on permeability.

Effluent Analysis

A simplified core flood setup was used for the experiments with effluent analysis (see Figure 3.16). This setup did not contain pressure sensors, but was extended by a sample collector after the backpressure regulator. Again 60°C and a vertical position of the Hassler cell were used.

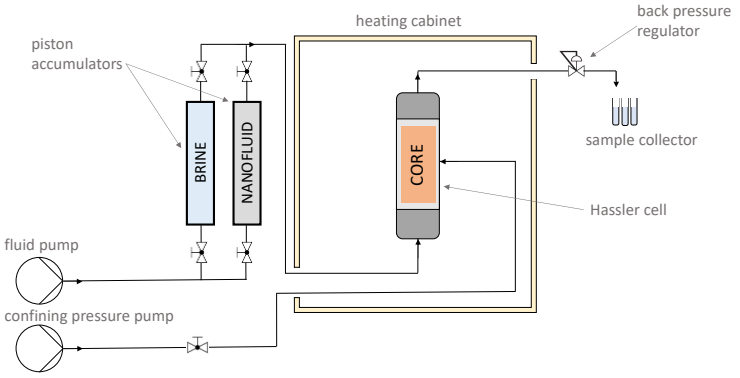

***Figure 3.16**: Core flooding setup for effluent analysis. Fluid samples were collected after being injected into the rock at 60°C.*

In a first step TW was injected though the TW saturated cores. Then, 60 ml 0.1 wt% nanofluid in TW with 30 ppm tracer was injected at 0.325 ml/min. After a sufficient volume of brine injection, 60 ml 1 wt% nanofluid in TW with 30 ppm tracer was injected, followed by a post-flush of brine. During all these steps effluent samples of 3-6 ml were collected. These samples were either analyzed via FFF, diluted with DIW by 1:3 for IC measurements or diluted with TW for UV-Vis spectrophotometry. The samples containing the 0.1 wt% nanofluid injection were diluted by 1:5 and samples with 1 wt% by 1:10.

UV-Vis Spectrophotometry measurements indicated contamination from the core by a peak at approximately 300 nm that led to the decision to dry the cores at 110° C for several hours. Additionally, the core plugs were isolated from the rubber sleeve in the Hassler cell with aluminum foil. The pressure sensors used for permeability evaluation were removed because stagnant brine in the lines to the pressure sensors caused visible corrosion and were possible sources of contamination.

3.2.12 Scanning Electron Microscope (SEM)

Electron microscopy differs to optical microscopy by the use of a beam of accelerated electrons instead of a visible light source. The wavelength of optical light limits the resolution of an image in an optical microscope. Electrons with a much smaller wavelengths are therefore necessary. When the primary electrons strike the sample, electrons are backscattered or ejected as secondary electrons. Collection of these secondary electrons from each point on the sample surface creates an image (Akhtar et al. 2018).

Core plugs of Berea and Keuper were cut into 1 cm disks to facilitate evaluations. These disks were vacuum saturated for several hours in 1wt% nanofluid of both types in either TW or FW. After vacuum saturation, the rock disks were dried in a vacuum oven at 60° C. The dried rock disks were broken to expose a rough untouched surface. After mounting the rock pieces on sample holders, the sides were covered with silver and the top was sputtered with gold. This cover of a thin gold layer is necessary to be electrically conductive and avoid overcharging on the surface (Akhtar et al. 2018). Subsequently, SEM imaging was conducted using a *TESCAN Mira3*. A preemptive test was conducted to evaluate, how crystallization of salt from brine influenced the SEM imaging. Overcharging was not observed and NaCl crystals distinctive in shape and size. Therefore, they could be identified using the EDX feature included in the SEM imaging system. Note that samples that have been treated with alkali solution were excluded from SEM imaging since they became very challenging to measure.

3.2.13 Ion Chromatography

Ion Chromatography (IC) is an analytical method to separate ions based on their interaction with a stationary and a mobile phase. These phases attract either anions or cations and measure conductivity for a specific type of ion that is attracted. The speed at which the ions move through the columns depends on differences in ion charge and size. As eluent is moving thought the column ions with weaker interaction will be carried out faster than ones with stronger interaction. Once the ions exit the column a detector measures electrical conductivity and the concentration of analytes can be determined (OSU.edu).

The chemical tracer Ammonium Thiocyanate (NH_4SCN) was added to the nanofluids in the core flood experiment. The prepared concentration was 30 ppm and the effluent samples were diluted by 1:3 with DIW. Subsequently, the samples were analyzed using a *Thermo Fisher Aquion* with an *AS9-SC* carbonate anion-exchange column. The eluent was 10 mM Na_2CO_3.

Chapter 4 Results and Discussion

4.1 Fluid Compatibility

Clear precipitations were observed by visually inspecting the mixture of FW with alkali (3000 ppm Na_2CO_3) as seen in Figure 4.1. Presumably these were mostly calcium carbonate due to the high pH of the alkali solution causing a supersaturation of dissolved calcium. Subsequently, compatibility tests of another nanoparticle manufacturer (not-included in this work) depicted precipitations for FW and TW. The presence of precipitations caused UV-Vis measurements to be inconclusive for those products, hence were excluded from the experimental program. Compatibility experiments for the nanoparticles shown in this work did not show any particular issue as described by Neubauer et al. (2020), Neubauer, Hincapie, Borovina, et al. (2020) and Saleh (2020).

***Figure 4.1**: Precipitations in a solution containing formation water and alkali (Saleh 2020).*

4.2 Batch Sorption

Batch sorption experiments were conducted to quantify the maximum mass of absorbable nanoparticles for a given combination of rock- fluid. Therefore, crushed rock material was mixed with nanofluids and alkali, tracking the concentration of nanoparticles using UV-Vis spectrophotometry (Section 3.2.9).

Various concentrations of nanofluid and brine were mixed and their UV-Vis signal measured to establish calibration plots. Plotting absorbance vs. concentration shows a linear relationship. The generated calibration constants that form the calibration plots shown in Figure 4.2 are listed in Table 4.1. They were used to calculate nanoparticle concentration from absorbance signals.

***Table 4.1**: Calibration constants for 24 h aged nanofluid solutions after filtration at 270 nm. These constants were later used to calculate nanoparticle concentrations from UV-Vis absorption measurements (FW: formation water, TW: test water, AS: alkali solution).*

	Brine	k_i	d_i	R^2
NF A	TW	0.3624	0.0020	0.9992
	FW	0.3984	0.0002	0.9991
	AS	0.3962	0.0023	0.9931
NF B	TW	0.4871	0.0046	0.9880
	FW	0.4579	0.0020	0.9982
	AS	0.4248	0.0346	0.9868

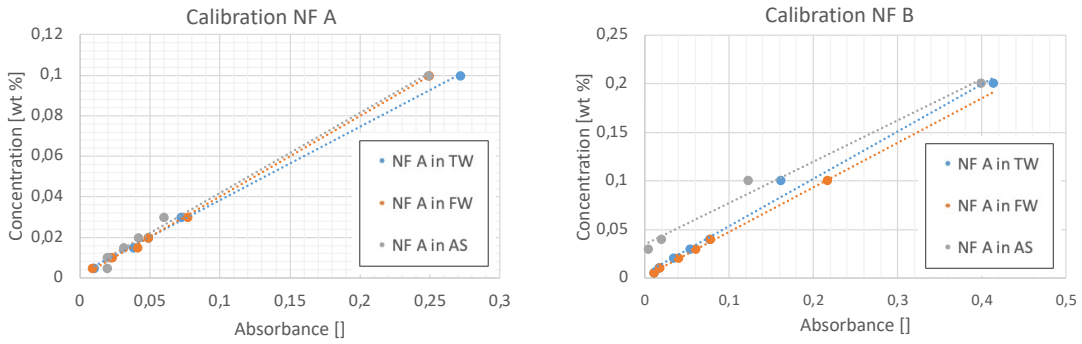

(a) Nanofluid A (b) Nanofluid B

Figure 4.2: Calibration graph for different concentrations of NF A (a) and NF B (b) in TW, FW and AS. The solutions were left resting for 24h after mixing and filtered using a 0,45 µm filter. A linear trend was found to fit the measured behaviour best for all solutions. These calibration plots enable the calculation of nanoparticle concentration from an absorbance measurement.

Blank samples comprised of the same mixture of brine and nanoparticle; however, they did not contain the respective rock material. To investigate the influence of rock and brine, reference samples were examined, which only contains brine and rock material. The absorbance signal of brine and rock without nanoparticle was taken as a baseline value and correction factors $Abs_{corr,i}$ are shown in Table 4.2. These correction factors account for the influence each rock type has on the UV-Vis measurement in a certain brine and temperature, when no nanofluid is present.

***Table 4.2:** Absorbance correction factors for rock materials in different brines at two temperatures using doublet measurements and an average standard deviation for absorbance at 270 nm of $3.8 \cdot 10^{-3}$ (FW: formation water, TW: test water, AS: alkali solution).*

Rock type	Brine	$Abs_{corr,i}$	
		22°C	60°C
Berea	TW	0.031	0.047
	FW	0.019	0.027
	AS	0.048	0.091
Keuper	TW	0.054	0.133
	FW	0.023	0.044
	AS	0.088	0.237

The measured values were evaluated using Eq. 4.1 and the calibration coefficients and the correction factors stated in Table 4.1 and Table 4.2.

$$c_{NF,i} = k_i * (Abs - Abs_{corr}) + d_i \quad 4.1$$

A reduction from initial nanoparticle concentration to the calculated residual concentration $c_{NF,i}$ was consequently accounted as nanoparticle adsorption to the rock material. Therefore, relative adsorption compared to the initial concentration [%] and absolute adsorption [wt %] was calculated.

Limitations of Measurement – Exclusion Criterion

Some of the obtained nanofluid's absorbance signals were far too small compared to the baseline correction factors, hence classified as noise. The decision was made to exclude measurements where the corrected absorbance was lower than 20% of the baseline values. The lower detection limit for the device in this configuration was found to be 0.005. Consequently, values below this threshold were excluded from the evaluation. This is attributed to the high influence of the rock and a corresponding high baseline combined with a low absorbance caused by the nanofluids. Therefore, the experimental set of samples was reduced to the ones listed in Table 4.3, Table 4.4, Table 4.5 and Table 4.6. The formation of a filter cake in the syringe filters was assumed, since it required considerable force to push the fluid through the filters compared to brine.

Nanofluid A

The results for NF A are presented in Table 4.3 for Berea and Table 4.4 for Keuper. In Berea outcrops, adsorption was similar across the brines with values of 92% (FW), 91% (AS) and 88% (TW). The high adsorption values for AS could be explained with the relatively high baseline values for alkali. It was observed that temperature had a minor effect on the adsorption behavior. Moreover, the addition of NF A did not alter the pH significantly in the investigated samples. Once crushed rock was added to mixtures of NF A with brine, pH slightly reduced by 0.3 in TW and 0.35 in FW.

Table 4.3: *Adsorption results and pH measurements for NF A in Berea. Absorbance measurements were performed in doublets with an average standard deviation of $1.8 \cdot 10^{-3}$ for all fluids. pH standard deviation was defined as $2 \cdot 10^{-2}$ for all fluids in average (FW: formation water, TW: test water, AS: alkali solution).*

Initial conc.	Brine	T	Residual conc. $c_{NF,i}$	Adsorption		Specific Adsorption		pH		
[wt%]		[°C]	[wt%]	[wt%]	[%]	[mg/g]	[mg/m²]	brine rock	NF brine rock	NF brine
0.1	TW	22	0.0118	0.0882	88	3.53	2.26	8.29	8.26	8.45
0.1	TW	60	0.0107	0.0893	89	3.57	2.39	8.24	8.29	8.58
0.1	FW	22	0.0083	0.0917	92	3.67	2.35	6.77	6.75	6.94
0.1	FW	60	0.0097	0.0903	90	3.61	2.31	6.87	6.78	7.14
0.1	AS	2	0.0088	0.0912	91	3.65	2.34	9.82	9.88	9.89
0.03	TW	22	0.0102	0.0198	66	0.79	0.51	8.29	8.30	8.41
0.03	TW	60	0.0070	0.0230	77	0.96	0.61	8.24	8.37	8.63
0.03	FW	22	0.0050	0.0250	83	1.00	0.64	6.77	6.79	6.80
0.03	FW	60	0.0050	0.0250	83	1.00	0.64	6.87	6.73	6.99

In Keuper outcrops, adsorption of NF A was similar in TW and FW with 77-80% at 22°C and 87-88% at 60°C. Here approximately 10% higher adsorption was seen in higher temperature. Brine containing alkali showed the lowest adsorption (77%). The pH values were very similar across the samples with pH 8.5 for TW, pH 7.1 for FW and pH 9.85 for AS.

Table 4.4: *Adsorption results for NF A in Keuper. Absorbance measurements were performed in doublets with an average standard deviation of $5 \cdot 10^{-3}$ for all fluids. pH standard deviation was defined as $2 \cdot 10^{-2}$ for all fluids in average (FW: formation water, TW: test water, AS: alkali solution).*

Initial conc.	Brine	T	Residual conc. $c_{NF,i}$	Adsorption		Specific Adsorption		pH		
[wt%]		[°C]	[wt%]	[wt%]	[%]	[mg/g]	[mg/m²]	brine rock	NF brine rock	NF brine
0.1	TW	22	0.0227	0.0773	77	3.09	1.98	8.40	8.40	8.45
0.1	TW	60	0.0133	0.0867	87	3.57	2.29	8.49	8.45	8.58
0.1	FW	22	0.0198	0.0802	80	3.21	2.05	7.03	7.15	6.94
0.1	FW	60	0.0119	0.0881	88	3.52	2.25	7.18	7.07	7.14
0.1	AS	22	0.0233	0.0767	77	3.07	1.96	9.85	9.88	9.89
0.03	TW	22	0.0116	0.0184	61	0.74	0.47	8.42	8.38	8.41
0.03	FW	22	0.0070	0.0230	77	0.92	0.59	7.03	7.11	6.80
0.03	FW	60	0.0073	0.0227	76	0.91	0.58	7.18	7.15	6.99

Nanofluid B

Table 4.5 shows the results for NF B in Berea and Table 4.6 for Keuper. In Berea outcrop samples adsorption was 94% (FW), 86%(TW) and 61% (AS). Adsorption in alkali samples was significantly lower compared to samples in TW and FW. The effect of temperature is not significant in TW and FW, however Berea samples showed high baseline values in TW at 60°C. The addition of rock material to the nanofluid in FW increased the pH from 4.71 to 6.36 (60°C). Data obtained for 0.03 wt% solutions suggest, that at this concentration nanofluid adsorption is high. Hence, the residual nanofluid concentration cannot be detected when the fluids contact the crushed rock.

Table 4.5: *Adsorption results for NF B in Berea. Note the increase in pH from 4.71 to 6.36 for 0.1 wt% NF B in FW at 60°C. Note the increase in pH from 4.71 to 6.36 for 0.1 wt% NF B in FW at 60°C.Absorbance measurements were performed in doublets with an average standard deviation of* $7.4 \cdot 10^{-4}$*. pH standard deviation was defined as* $2 \cdot 10^{-2}$ *for all fluids in average (FW: formation water, TW: test water, AS: alkali solution).*

Initial conc.	Brine	T	Residual conc. $c_{NF,i}$	Adsorption		Specific Adsorption		pH		
[wt%]		[°C]	[wt%]	[wt%]	[%]	[mg/g]	[mg/m²]	brine rock	NF brine rock	NF brine
0.1	TW	22	0.0125	0.0875	88	3.50	2.27	8.29	8.22	8.44
0.1	TW	60	0.0146	0.0854	85	3.42	2.19	8.24	8.27	8.61
0.1	FW	22	0.0057	0.0943	94	3.77	2.41	6.77	6.21	4.96
0.1	FW	60	0.0068	0.0932	93	3.73	2.39	6.87	6.36	4.71
0.1	AS	22	0.0387	0.0613	61	2.45	1.57	9.82	9.83	9.86
0.03	FW	22	0.0051	0.0249	83	1.00	0.64	6.77	6.53	6.24
0.03	FW	60	0.0125	0.0243	81	1.01	0.65	-	6.74	-

For crushed Keuper material nanoparticle adsorption was 93% (FW), 83% (TW) and 61% (AS). Adsorption in samples containing AS was significantly lower compared the samples without. The effect of temperature seemed to be minor compared to the influence of the crushed rock material, which resulted in high baseline absorbance values. The addition of Keuper material to FW and NF B resulted in an increase from pH 4.71 to pH 6.36.

Table 4.6: *Adsorption results for NF B in Keuper. Note the increase in pH from 4.71 to 6.73 for 0.1 wt% NF B in FW at 60°C. Absorbance measurements were performed in doublets with an average standard deviation of $3.6 \cdot 10^{-3}$. pH standard deviation was defined as $2 \cdot 10^{-2}$ for all fluids in average (FW: formation water, TW: test water, AS: alkali solution).*

Initial conc.	Brine	T	Residual conc. $c_{NF,i}$	Adsorption		Specific Adsorption		pH		
[wt%]		[°C]	[wt%]	[wt%]	[%]	[mg/g]	[mg/m²]	brine rock	NF brine rock	NF brine
0.1	TW	22	0.0172	0.0828	83	3.31	2.12	8.40	8.30	8.44
0.1	FW	22	0.0065	0.0935	93	3.74	2.39	7.03	6.64	4.96
0.1	FW	60	0.0066	0.0934	93	3.74	2.39	7.18	6.73	4.71
0.1	AS	22	0.0468	0.0532	53	2.13	1.36	-	9.86	-
0.03	FW	22	0.0062	0.0238	79	0.95	0.61	7.03	6.89	6.24

Discussion of Batch Sorption Results

Nanoparticle concentration reduction in the batch adsorption can have two main reasons: particle aggregation (colloidal instability) or adsorption to the minerals. The formation of aggregates would result in a filtration by the syringe filter (0.45 µm mesh). As seen in Figure 4.4 (section 4.3.1) the particle structures formed during a core flood are almost 500 nm in size. If the agglomeration behavior between batch sorption and core flood is similar, these structures would be filtered out by the syringe filter. Note, that the formation of a filter cake was assumed since it required higher force to filter batch sorption samples compared to other fluids. This is in agreement with S. Li et al. (2019) who found a severe influence of nanoparticles of the same manufacturer on permeability as discussed in detail in section 4.3.1.

The specific adsorption values are considerably higher compared to the ones observed in the core flood experiments described in section 4.3. This could be explained by the higher fluid to rock ratio (4:1) used in batch sorption experiments compared to the core flood experiments (5:3). Despite similar results for specific surface area the crushed rock material could provide new binding sites for nanoparticles, since the rock is freshly broken. The high adsorption in FW samples could be explained by the presence of divalent cations in the brine, which result in a higher ionic strength. An increased ionic strength compresses the EDL and therefore weakens particle repulsion forces (Miller 2019). Hence, electrostatic stabilization is expected to fail in these conditions since the energy barrier for particle agglomeration is lowered and the kinetic energy increasingly dictates the particle aggregation (Metin et al. 2011). A compression of the EDL was also thought to be the primary influence of particle aggregation in the presence of NaCl in the work presented by Pham and Nguyen (2013). The observation of highest absorption in FW and lowest in alkali solution could also be explained with their respective pH. For unmodified silica nanoparticles a higher pH results in a more negative Zeta Potential and therefore higher particle repulsion. This effect could be less pronounced for the used nanoparticles, since Zeta Titration plots (Figure 3.7) suggest similar Zeta Potential values across the applied pH range. Additionally, nanoparticles could be in competition with weakly associated alkali cations as described by Qiu et al. (2018). The work of Yukselen-

Aksoy and Kaya (2003) showed that kaolinite had a more negative zeta potential with increase in pH however the presence of divalent cations (Ca^{2+} & Mg^{2+}) decreased the zeta potential. This behavior could be a possible explanation for high adsorption in formation water. The work conducted by Pham and Nguyen (2013) showed reduced adsorption in higher concentrations of nanofluid. They suggested surface modifications provide stability to the dispersion beyond a certain concentration threshold. The described trend is difficult to evaluate due to weak response in UV-Vis measurements for 0.03 wt% solutions. S. Li et al. (2019) reported similar problems detecting UV-Vis signals at concentrations as low as 0.05 wt%.

The observations made in the batch sorption experiments attribute temperature a minor effect in adsorption behavior do not confirm the work presented by Pham and Nguyen (2013). There, an increased nanoparticle aggregation rate at elevated temperatures was attributed to the higher kinetic energy and more frequent particle collisions.

4.3 Core Flood Experiments

4.3.1 Permeability to Brine

Step rate tests with brine have been performed to evaluate the potential damage of nanofluid injection. Injecting brine before nanoparticles (baseline) and after nanoparticles allowed defining the possible damage. The permeability was assessed using Darcy's equation as shown in Eq.4.2. Permeability to brine was plotted in Figure 4.3 for each step of the injection sequence.

$$k_{brine} = \frac{Q\mu l \cdot 4 \cdot 1000 \cdot 1.01325}{d^2\pi \cdot 60 \cdot dp} \qquad 4.2$$

where Q is flow rate [ml/min], μ is brine viscosity [mPas], l and d core length and diameter [cm] and dp the differential pressure dp [bar].

Note that permeability to gas was measured as for both cores ~490 mD for the tested cores, whereas permeability to brine was considerably lower. This observation is in agreement with the work of Tanikawa and Shimamoto (2009). Permeability to brine (before and after) proved that injecting the tested nanofluids do not reduce the permeability to brine considerably to be accounted.

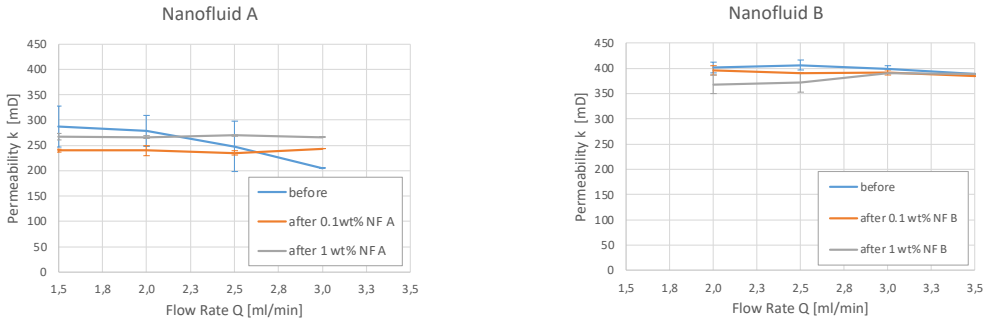

(a) Nanofluid A (b) Nanofluid B

Figure 4.3: *Permeability to brine was measured before a nanofluid injection (blue), after an injection of 0.1 wt% of NF (orange) and after an injection of 1 wt% NF (grey). NF A (a) and NF B (b) were both diluted in TW and all permeability measurements were conducted with TW.*

Discussion of Core Flooding Results

The formation of a filter cake was not visible which is in contrast to the work of Bila and Torsæter (2021) who investigated similar products to NF A in two phase experiments on Berea core plugs. There, the formation of a filter cake and higher displacement pressures were observed in oil displacement tests with crude oil. One could assume that the presence of oil enhanced the possible filter-cake formation as compared to single-phase evaluations here presented.

Various studies have been conducted investigating fines migration behavior. If the ratio between particle to host diameter (d/D) is between 0.01 and 0.6 the particles can form bridges and block pores (Cao et al. 2017, Khilar and Fogler 1998). The formation of aggregates would be necessary to block pore throats since the nanoparticles themselves are orders of magnitude smaller than typical pore-throat diameters. Nanoparticle retention is mainly caused by physicochemical interaction with the porous media (Zhang et al. 2015, Nowack and Bucheli 2007). Since the tested nanofluids did not reduce the permeability to brine considerably a formation of aggregates of sufficient size to block pores could be ruled out. Scanning electron microscopy (SEM) images discussed in detail in section 4.4 support this observation, showing adsorbed particles on the rock. The formation of the nanoparticle clusters seen in Figure 4.4 is assumed to be insufficient to block pore throats and cause a reduction in permeability. This is in agreement with the work of Yu et al. (2012), who studied adsorption and transport of nanoparticles in porous media. They observed no effects on permeability in sandstone, whereas severe plugging occurred in dolomite and limestone samples. A detailed investigation on the effects of hydrophilic (FNP) and hydrophobic fumed silica nanoparticles (FNP-O) was conducted by (S. Li et al. 2019). Their work provided evidence, that 0.05 wt% FNP in 30g/l NaCl reduced permeability to brine by a factor of 200.

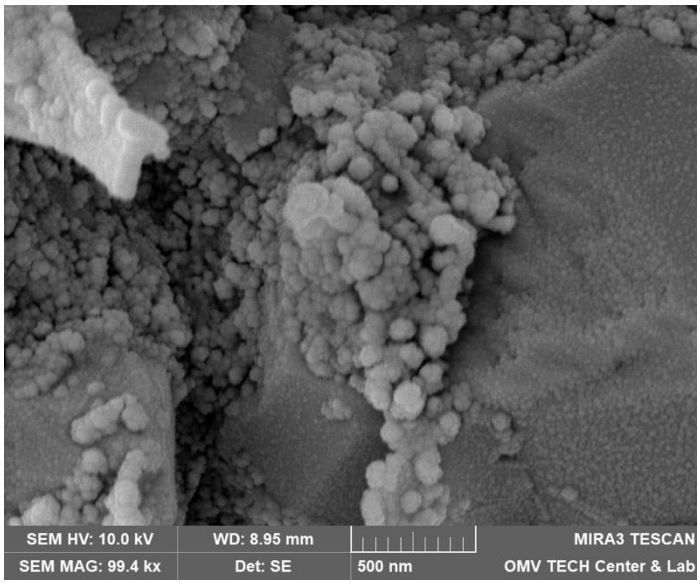

Figure 4.4: *Scanning Electron Microscopy (SEM) image of a core flood rock sample following an injection of 1 wt% nanofluid A in test water.*

4.3.2 Effluent Analysis

Four core floods have been conducted to analyze effluents for nanoparticle and tracer concentration. Selected samples have been additionally analyzed using Flow Field Flow Fractionation (FFF), Dynamic Light Scattering (DLS) and Multi Angle Light Scattering (MALS).

Each core flood comprised of 1) an initial flush with TW, 2) a low concentration nano injection, 3) TW flush, 4) a high concentration of nanofluid injection and 5) TW post flush, as described in section 3.2.11. For all plots in this section NF and tracer injection starts at 0 PV on the abscissa and the end is marked with a dashed vertical line.

Nanofluid A in Berea

The effluent analysis for 0.1 wt% and 1 wt% NF A injections in Berea is shown in Figure 4.5. Plot (a) shows, that the nanoparticle concentration in the effluent does not rise considerably during the first injection. The tracer included in the nanofluid injection was detected and has a distinctively shaped breakthrough curve. After a flush with TW the second injection caused an almost parallel increase in both tracer and nanoparticle concentration. This behavior might result from a saturation with nanoparticles and no further adsorption in the core. It is worth noticing that both the tracer and the 1 wt% nanofluid injection reach a stable plateau at a lower concentration than the injection concentration. A comparison between tracer effluent history for both injection steps is presented in Figure 4.6. The breakthrough is similar for injection steps with 50% of the tracer concentration arriving after ~0.95 PV. After a plateau the concentration reduces in the second injection step slower.

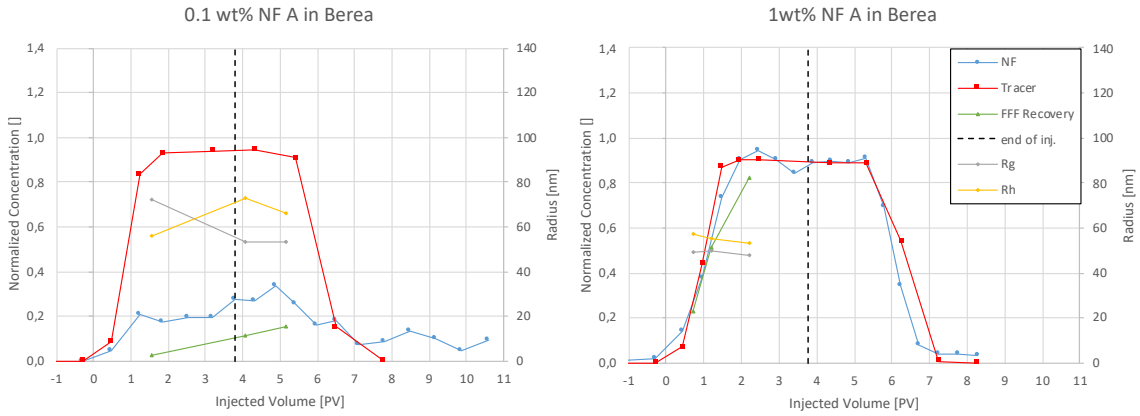

(a) 0.1 wt% NF A – Berea

(b) 1 wt% NF A - Berea

Figure 4.5: *Effluent analysis for 0.1 wt% (a) and 1 wt% (b) NF A in TW in Berea sandstone. For the low concentration injection high adsorption is seen for NF A, whereas the tracer seems to pass the core unaffected. During the high concentration injection of NF A, the effluent concentration follows the tracer concentration better indicating no further adsorption. Particle size measurements confirm the low NF recovery (green) and larger particles arriving earlier in the effluent.*

A nanoparticle concentration calculation via the DLS measurements shows a similar low recovery in the first injection step as the UV-Vis spectrophotometry. The results for this calculation can be seen in the green lines in Figure 4.5 and show a parallel trend to the respective nanoparticle concentration. Hydrodynamic radius (R_h) describes the radius of the particle including a hull of solvent. Therefore, usually R_h is slightly bigger compared to the radius of gyration (R_g). The results for the first measurement done in the first injection (a) shown in Figure 4.5, indicates otherwise. This may be explained with the low concentration of recovered nanofluid resulting in an error of 4.3% (R_g) and 8.3% (R_h) compared to an average error of 2.5% (R_g) and 1.4% (R_h) in Keuper samples. The effluent history shows a slight decrease in size (second injection), indicating that bigger particles move faster through the core.

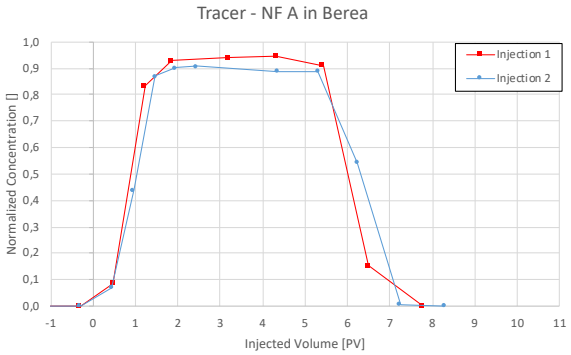

Figure 4.6: *A comparison of tracer concentration history indicates a similar tracer breakthrough at ~0.95 PV (50%) for both injection steps and a slightly longer retention in the second injection.*

The obtained effluent histories were used to calculate the mass of produced nanofluid and tracer by integration and results are presented in Table 4.7. The ratio of produced over injected tracer is ~85%, indicating an baseline value for recovery of an inert chemical. The recovery of NF A in the second injection step is almost at that level (79.3%), whereas it is only 22.5% of the first injection. These results lead to a specific adsorption of 0.455 mg/g and 1.215 mg/g (nanoparticle/rock) respectively.

Table 4.7: *Adsorption results following mass balance calculation for NF A in Berea.*

	0.1 wt% NF A in TW	**1 wt% NF A in TW**
NF Recovery [%]	22.46	79.31
NF Adsorption [mg/m²]	0.317	0.846
NF Adsorption [mg/g]	0.455	1.215
Tracer Recovery [%]	85.49	84.37

Discussion of Effluent Analysis for Berea NF A

The adsorption of considerable amount of nanofluid resulting in a delay in nanoparticle breakthrough seen in this core flood is in agreement with experiments performed by an external provider. In these experiments 0.1 wt% NF A in TW was injected into a Berea core with 3.5 cm diameter with 7.8 ml/min and the effluent was analyzed using DLS. The

recorded nanofluid concentration seen in Figure 4.7 shows no breakthrough until 17 PV had been injected.

Specific adsorption values presented in Table 4.7 comply with results provided by Zhang et al. (2015) for PEG coated silica nanoparticles in Boise sand packs.

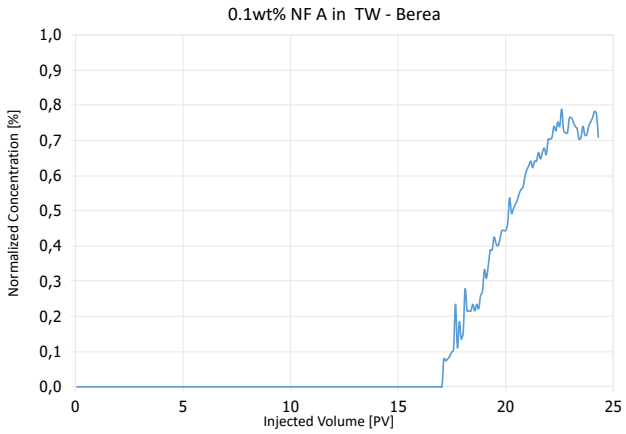

***Figure 4.7**: Preceding tracer test showing a nanofluid breakthrough after 17 PV. In this core flood 0.1 wt% NF A in TW was injected and nanoparticle concentration was evaluated using DLS.*

Nanofluid A in Keuper

The effluent history for NF A in Keuper shows a significant difference to Berea as seen in Figure 4.8.The low concentration injection of NF A results in a delayed increase in nanoparticle concentration compared to the tracer. The NF concentration peaks at 0.13 wt% and decreases to zero with a delay compared to the tracer. The second injection shows NF concentration increase earlier or at least simultaneously to the tracer.

The comparison between tracer concentration history for both injection steps seen in Figure 4.9 shows a parallel breakthrough of tracer. However, the plateau is reached slower and a delay in concentration reduction can be observed for the second injection step. Particle size measurements reveal that larger particles elute earlier compared to smaller ones for both injection steps.

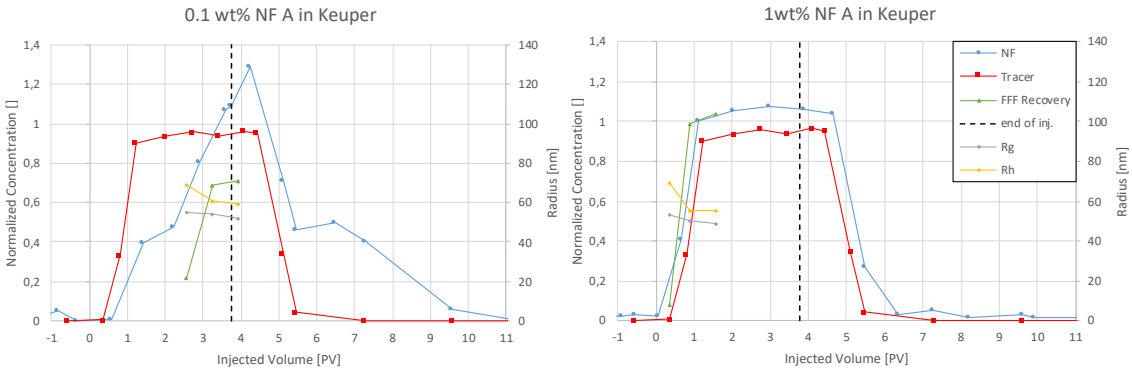

(a) 0.1 wt% NF A - Keuper

(b) 1 wt% NF A - Keuper

Figure 4.8: *Effluent analysis for 0.1 wt% (a) and 1 wt% (b) NF A in TW in Keuper sandstone. A delayed breakthrough of nanoparticles can be seen in (a) peaking at a higher concentration than injected. An earlier nanoparticle breakthrough is seen in (b) compared to the tracer. Particle size measurements confirm UV-Vis concentration results and show larger particle arriving faster in the effluent.*

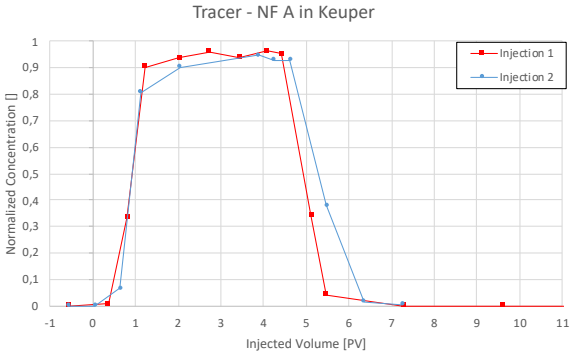

Figure 4.9: *Tracer concentration history for Nanofluid A in Keuper in two injection steps. An identical tracer breakthrough can be observed at 0.9 PV (50%) whereas the plateau is reached slower. A delayed decrease in concentration for the second injection step can be observed.*

The mass balance calculated from these concentration profiles shows a tracer recovery of 85-90%. Nanoparticle recovery of recovery of ~105% in for UV-Vis measurements are confirmed by FFF recovery during the second injection. A calculation of negative specific adsorption is therefore meaningless, since it can be assumed the core does not produce nanoparticles.

Table 4.8: *Adsorption results following mass balance calculation for NF A in Keuper.*

	0.1 wt% NF A in TW	**1 wt% NF A in TW**
NF Recovery [%]	104.20	104.98
Tracer Recovery [%]	84.72	90.05

Discussion of Effluent Analysis for Keuper NF A

The NF concentration history shown in Figure 4.8 (a) suggests a reversible retention of nanoparticles in the core resulting in sorption and desorption. The early breakthrough of nanoparticles observed in plot (b) might indicate, that the core is saturated with nanoparticles and no further ones can be adsorbed. A delayed breakthrough of nanoparticles compared to tracer was observed as well by Abhishek, Hamouda, and Ayoub (2018) and S. Li et al. (2019). The latter used PEG coated silica nanoparticles by the same manufacturer as used in this evaluation. The delayed breakthrough was explained with the adsorption/retention of nanoparticles on the rock surface. The delayed decrease in nanoparticle concentration was explained with desorption of reversibly attached nanoparticles.

The nanoparticle recovery exceeding 100% could be caused by the elution of other UV light absorbing material. This effect has been minimized by covering the rock cores in aluminum foil to reduce contact with the core holder's rubber sleeve. Additionally, they

have been dried in the vacuum oven at 105°C after Soxhlet extraction. Preemptive tests indicated that the solvents used for this cleaning procedure had a strong effect on UV-Vis measurements.

Nanofluid B in Berea

Nanofluid (NF) B showed little delay to the tracer breakthrough in Berea as seen in Figure 4.10. In the first injection step the nanofluid shows a delayed breakthrough forming a peak at 0.11 wt%. Effluent concentration decreases faster compared to the tracer. In the second injection step nanoparticles show now delay to the tracer but also exceed the injected concentration. This behaviour creates a calculated NF recovery of ~77 % and ~112 % respectively. FFF and DLS data confirms these concentration measurements by showing a NF concentration of 106 % compared to blank samples. Particle size analysis suggests, that larger particles arrive earlier in both injection steps. The comparison seen in Figure 4.11 shows a very similar trend for tracer concentration history in both injection steps. Mass balance calculation (Table 4.9) of the first injection step results in a specific adsorption of 0.09 mg/m² and 0.13 mg/g (nanoparticle/rock).

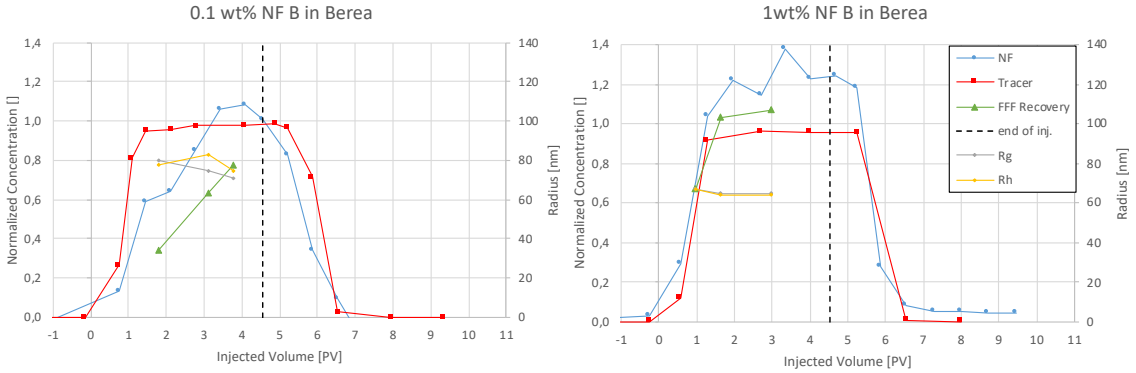

(a) 0.1 wt% NF B - Berea

(b) 1 wt% NF B - Berea

***Figure 4.10**: Effluent analysis for NF B in for 0.1 wt% (a) and 1 wt% (b) in TW in Berea sandstone. The calculated maximum concentration exceeds the injected concentration. The nanofluid shows only a slightly delayed breakthrough compared to the tracer.*

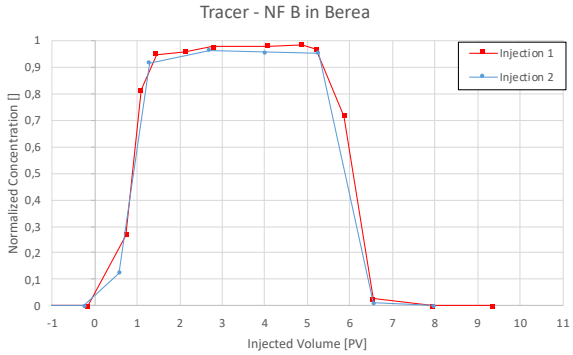

***Figure 4.11:** Tracer breakthrough comparison for NF B in Berea shows both breakthroughs at 0.9 PV.*

Table 4.9: *Adsorption calculation via mass balance following concentration calculation using UV-Vis spectroscopy data for nanofluid A in Berea outcrop core.*

	0.1 wt% NF B in TW	**1 wt% NF B in TW**
NF Recovery [%]	77.21	112.65
NF Adsorption [mg/m²]	0.090	-
NF Adsorption [mg/g]	0.130	-
Tracer Recovery [%]	90.35	89.50

Discussion of Effluent Analysis for Berea NF B

NF B showed less adsorption compared to NF A. The nanofluid recovery exceeding 100% in the second injection suggests the elution of other UV light absorbing material as mentioned above. Based on this result, it can be assumed, that the calculated values for specific adsorption seen in Table 4.9 might be not representative.

Nanofluid B in Keuper

Effluent analysis for Keuper outcrop core is seen in Figure 4.12 for 0.1 wt% and 1 wt% NF B in Keuper. The maximum measured NF concentration was 0.14 and 1.2 wt%, exceeding the respective injection concentration. Furthermore, the concentration does not reduce completely to zero after the injection and stays at ~12% in both cases. These two factors suggest the elution of other UV light absorbing material, which could result in an increased calculated concentration. For the first injection step FFF and DLS data show a nanofluid concentration below the injected concentration. However, the values are considerably lower compared to results obtained via UV-Vis for all four core floods. Nanofluid breakthrough appears to be only slightly delayed for the first injection and earlier for the second injection. As particle size measurements indicated in all previous experiments, bigger particles are eluted faster than smaller ones.

Since NF concentration did not reduce to zero, the mass balance calculation had to be adapted. The concentration was assumed to be zero after 7 PV, where tracer concentration was zero. Still, the calculated NF recovery exceeded 100% as seen in Table 4.10.

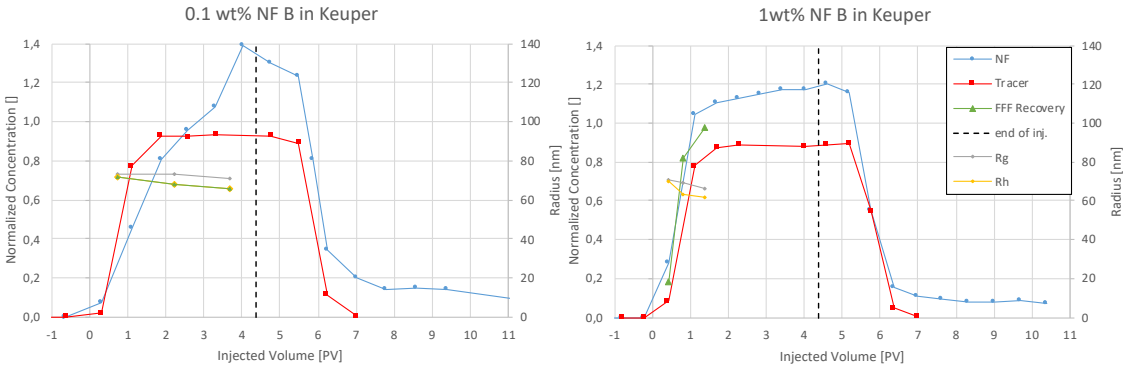

(a) 0.1 wt% NF B - Keuper (b) 1 wt% NF B - Keuper

Figure 4.12: *Effluent analysis for nanofluid (NF) B in Keuper shows concentration peaks exceeding the injected concentration. In both cases the calculated concentration remains at a constant level after the injection.*

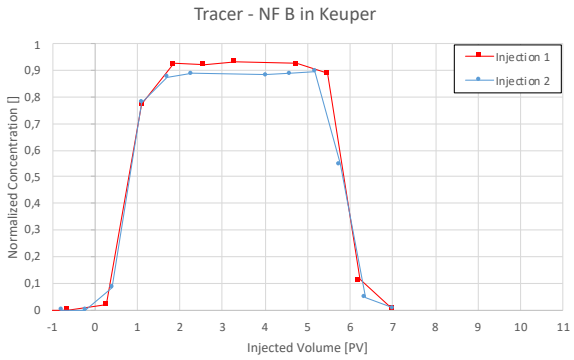

Figure 4.13: *Tracer analysis for nanofluid (NF) B in Keuper outcrop core. The concentration history is almost parallel for both injection steps.*

Table 4.10: *Adsorption calculation via mass balance following concentration calculation using UV-Vis spectroscopy data for nanofluid B in Keuper outcrop core.*

	0.1 wt% NF B in TW	**1 wt% NF B in TW**
NF Recovery [%]	108.1	113.1
Tracer Recovery [%]	89.85	85.87

Discussion of Results

Nanofluid B appeared to have lower adsorption to the used rock cores compared to NF A. Nevertheless, a higher nanofluid recovery was observed in Keuper rock compared to Berea which could be explained by the higher clay content in Berea. The early nanoparticle breakthrough compared to tracer (second injection) suggests low adsorption to the rock and faster elution compared to the tracer. A possible explanation for this effect may be a saturation of the core during the first injection step. In the second injection step adsorption sites for nanoparticles would be occupied leading to an early breakthrough. Since the tracer has not been adsorbed to the core in the first injection step

it would pass through it in the exact same pattern in the second injection, which can be seen in Figure 4.12.

4.3.3 FFF & Particle Size Measurements

Flow Field Flow Fractionation (FFF) and subsequent DLS and MALS measurements performed for selected core flood effluent samples have been mentioned in the previous section. Additionally, measurements comparing the effect of brine on particle size have been investigated and the results can be seen in Table 4.11. Results for radius of gyration (R_g) and hydrodynamic radius (R_h) did not differ significantly across the used concentrations. A difference in size was not observed between samples diluted in FW and TW for both nanofluids. NF B showed higher values for hydrodynamic radius compared to the radius of gyration, whereas both values were very similar.

Table 4.11: *Particle size measurements for different concentrations of nanofluids (NF) in two brines (formation water (FW) and test water (TW). R_g: Radius of gyration (R50; MALS), R_h: Hydrodynamic radius (DLS).*

Nanofluid	Brine	Concentration [wt%]	R_g [nm]	R_h [nm]
NF A	TW	0.1	48 ± 1.6%	56 ± 2.7%
		1	48 ± 0.5%	54 ± 1.4%
	FW	0.1	49 ± 0.1%	54 ± 0.5%
	DIW	-	60	52
NF B	TW	0.1	64 ± 0.8%	62 ± 1.6%
		1	66 ± 0.4%	67 ± 3%
	FW	0.1	68 ± 1.6%	64 ± 0.8%
	DIW	-	96	61

Discussion of Results

The used nanoparticles have high fractal dimensions as observed in the reported measurements. This could explain why the particle size measured by DLS (R_h) is smaller than one via R_g, especially for NF B in DIW. However, the value for R_g for NF B in DIW (96 nm) is significantly higher compared to all other R_g values (FW and TW). The differences seen here might be explained by the strong influence of the device and experimental setup for particle size estimation. Values for nanoparticle solutions in DIW have been measured by the manufacturer, whereas all other measurements were conducted in the means of this work.

4.4 Scanning Electron Microscopy (SEM)

Rock disks from Berea and Keuper outcrop material have been vacuum saturated in 1 wt% of NF in TW and FW. Furthermore, a section of the middle of each rock used in the core flood experiment has been investigated. The detailed analysis of over 180 SEM images was comprised; however, this chapter focuses on outlining differences in adsorption behavior and therefore only a selection is presented.

4.4.1 Effect of Minerology

Both nanofluids showed adsorption to all minerals present in the rock, regardless of the used brine. Spots not completely covered in nanoparticles were usually smooth quartz cement faces as seen in Figure 4.14. However, the adsorption of nanoparticles in clusters was also observed on those. Clay minerals present in the rock such as kaolinite, chlorite, illite and iron oxide minerals were coated and in the following section examples of kaolinite are presented (Figure 4.15, Figure 4.16).

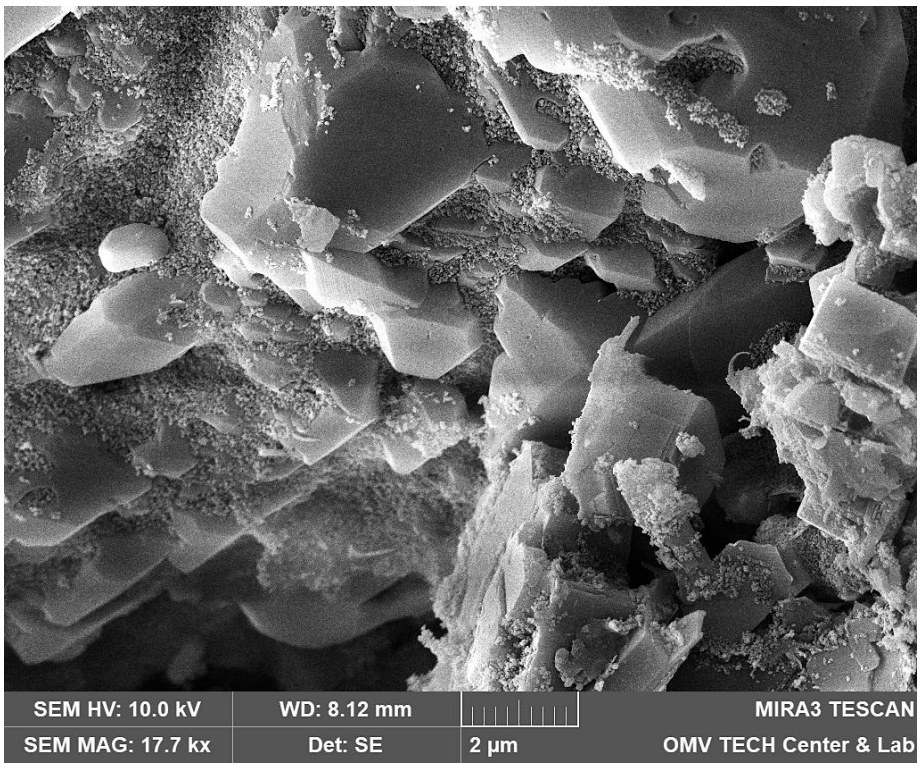

***Figure 4.14**: This image representative for SEM images conducted in this work. Nanoparticles can be observed on almost all surfaces of minerals. The only exception is quartz cement with its distinctive smooth faces (Vacuum saturation of 1 wt% NF A in formation water; Berea).*

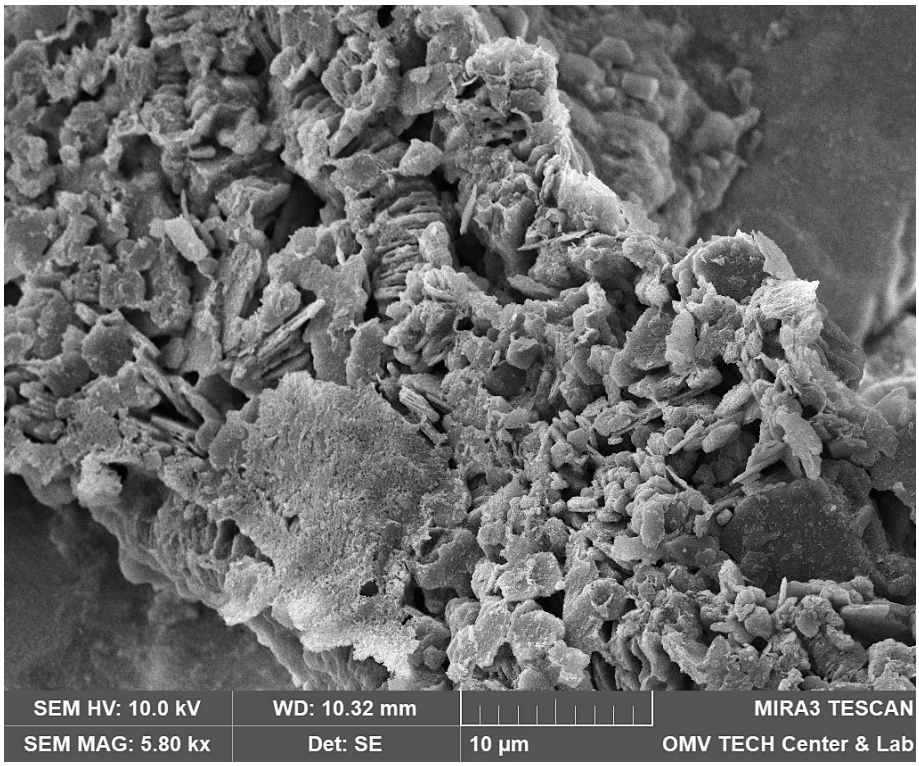

Figure 4.15: *This overview shows various clay minerals that are coated completely with a layer of nanoparticles (Vacuum saturation of 1 wt% NF B in FW; Keuper).*

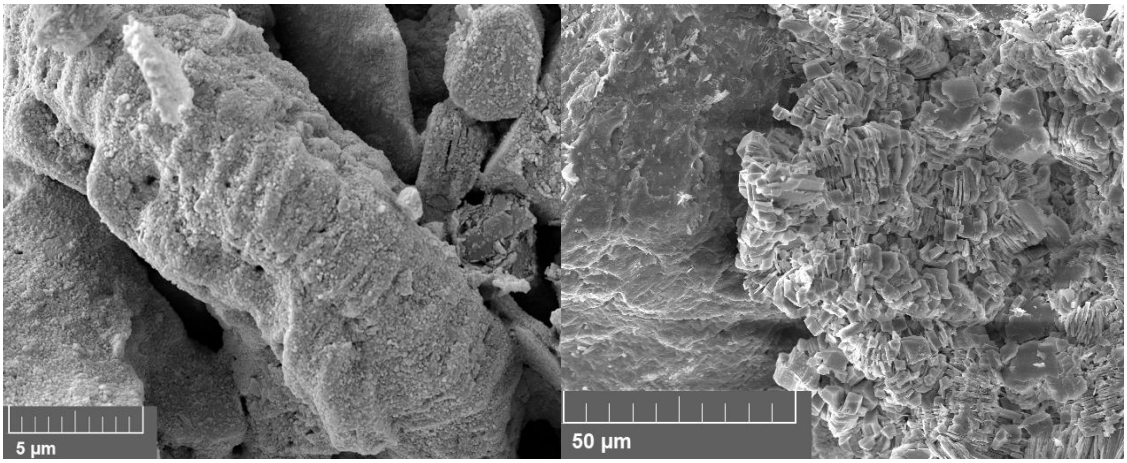

Figure 4.16: *A comparison between nanoparticle covered(left) and clean (right) kaolinite structures. Note, that the smoothed edges on left image are signs of weathering and not caused by the nanoparticle treatment (left: core flood sample of 1 wt% NF A in test water, Keuper; right: untreated sample, Berea).*

Interesting adsorption patterns can be seen in Figure 4.17, where nanoparticles are aligned with mineral edges in distinctive patterns. Figure 4.18 shows adsorption to spherical iron oxide minerals that seem to form towers radiating away from the spheres.

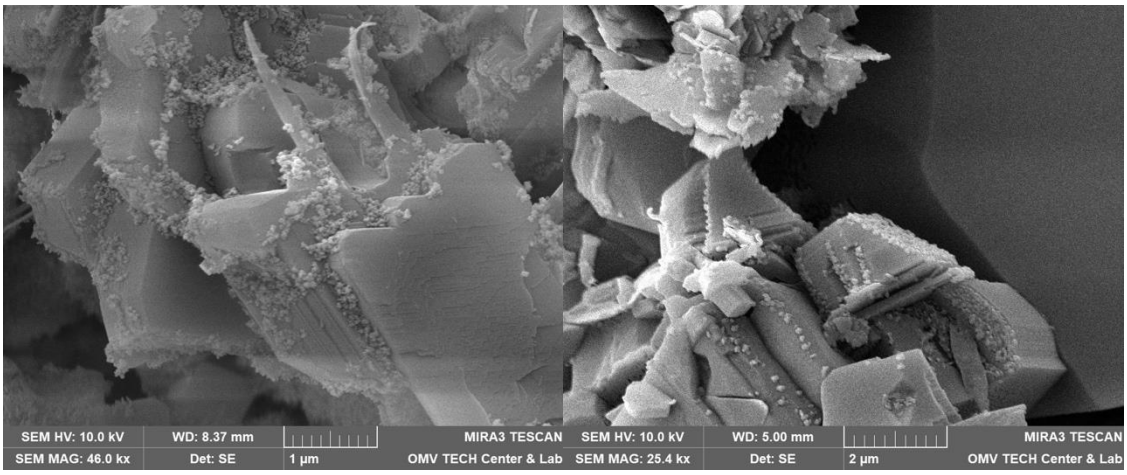

***Figure 4.17**: Nanoparticles are adsorbed in patterns parallel to mineral edges. The images show vacuum saturation samples of 1wt% NF A in FW (left) and 1wt% NF B in TW (right).*

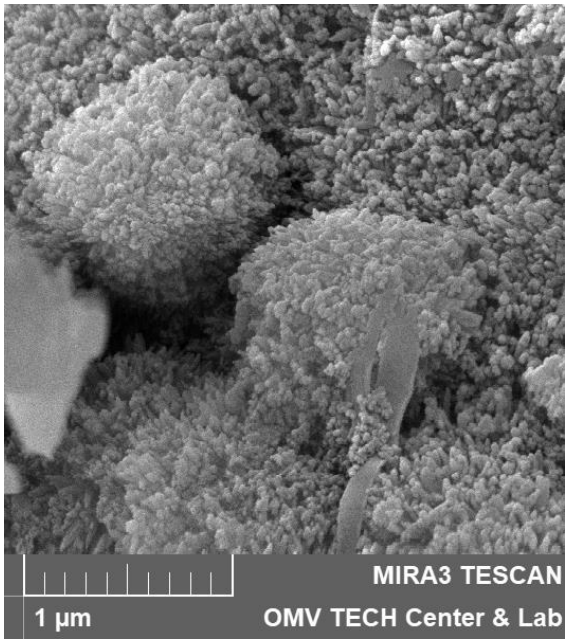

***Figure 4.18:** Nanoparticles were also observed to adsorb on iron oxides as seen in this image. The nanoparticles seem to form towers that are directed away from the centers of these mineral spheres. (Vacuum saturation of 1 wt% NF A in FW; Berea).*

4.4.2 Effect of Brine

Vacuum saturation samples with nanofluid diluted in FW and TW showed slightly higher adsorption in FW. This can be seen in Figure 4.19 for NF A in Berea. In NF B this effect was not as strong pronounced as seen in Figure 4.20 in kaolinite structures found in Keuper.

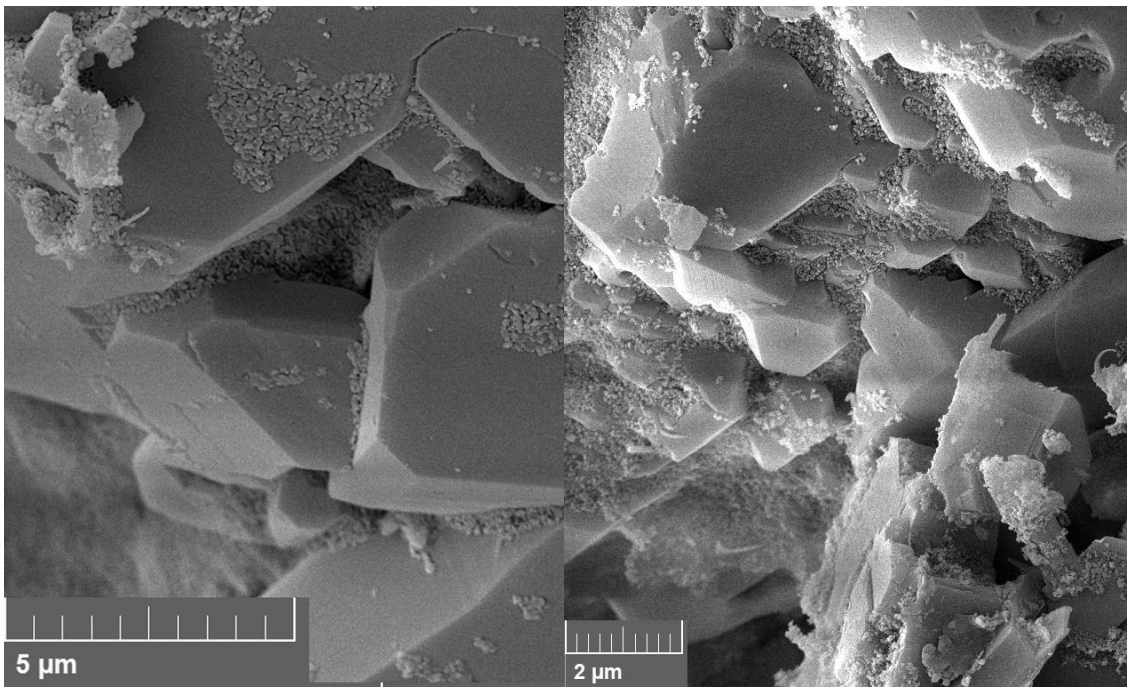

***Figure 4.19**: This image shows a comparison between adsorption of NF A to Berea in formation water (left) compared TW (right). Surfaces in the FW sample were coated slightly more with nanoparticles. (left: Vacuum saturation of 1 wt% NF A in FW, Berea; right: vacuum saturation of 1 wt% NF A in TW, Berea).*

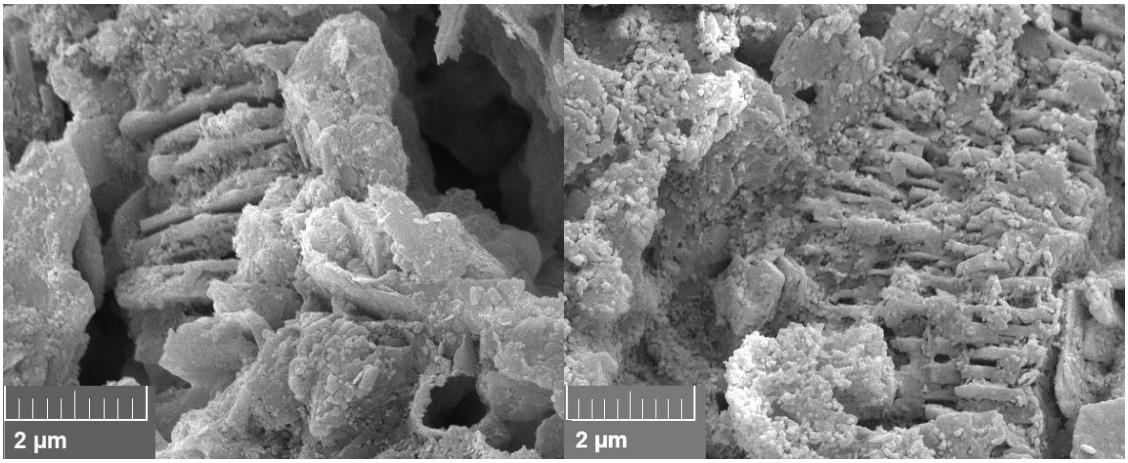

***Figure 4.20:** Comparison between NF B in formation water (left) and test water (right) on kaolinite structures found in Keuper rock. The sample treated with NF B in TW shows slightly higher adsorption of nanoparticles (left: Vacuum saturation of 1 wt% NF B in FW, Keuper; right: Vacuum saturation of 1 wt% NF B in TW, Keuper).*

4.4.3 Vacuum Saturation vs. Core Flood

SEM images of samples used in core floods show variations of the vacuum saturated samples. Direct comparisons for 1 wt% NF A and B in TW are seen in Figure 4.21 and Figure 4.22. Nanoparticles are adsorbed in bigger clusters in the core flood image compared to a monolayer adsorption in the vacuum saturation sample.

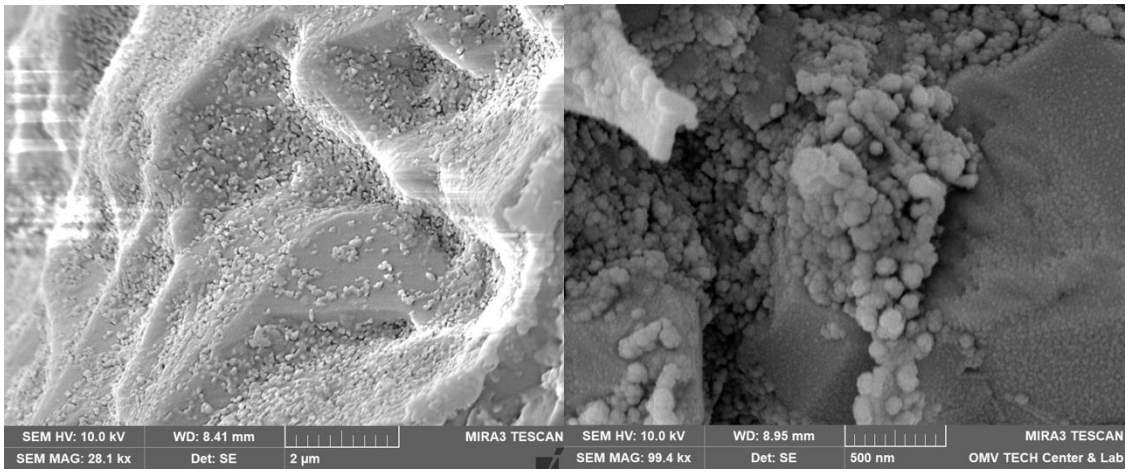

Figure 4.21: *The image on the left shows a rock sample that has been vacuum saturated whereas the image on the right shows a core flood sample. Both samples have been treated with 1 wt% nanofluid A in test water. Bigger particle structures can be seen on the core flood sample.*

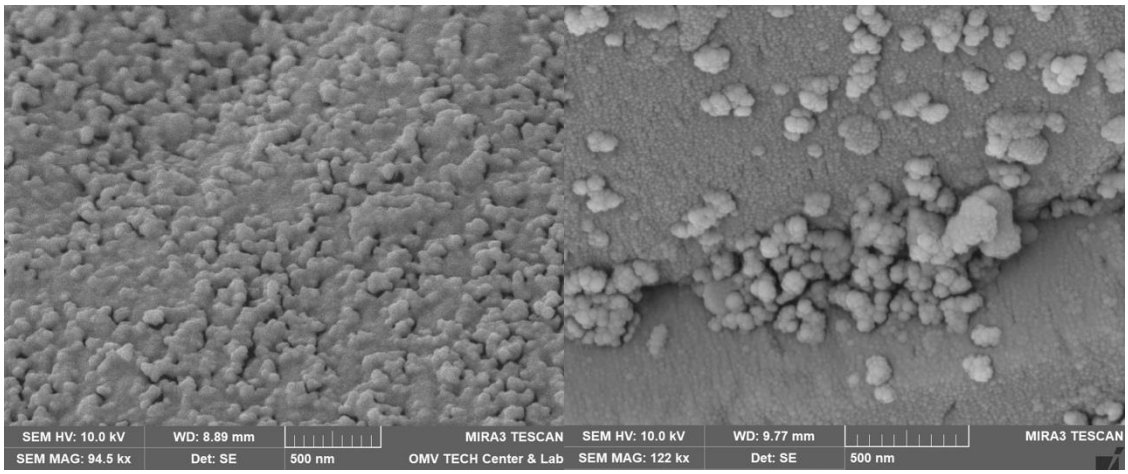

Figure 4.22: *This comparison shows a rock sample that has been vacuum saturated on the left and a core flood sample on the right. Both samples have been treated with 1 wt% nanofluid B in test water, however bigger particle agglomeration can be seen the core flood image.*

4.4.4 Discussion of Scanning Electron Microscopy Results

The results suggest that the mineral types present in the rock have a minor effect on the adsorption behavior. A higher adsorption affinity for quartz over kaolinite as described by Abhishek and Hamouda (2017) has not been observed in these experiments. This behavior could be explained with quartz and kaolinite having a strong negatively charged surface which would result in higher repulsion (Yukselen-Aksoy and Kaya 2003). In contrast to this, high adsorption in successive layers was found on iron oxide minerals, which have strong positive zeta potential. Since the used silica nanoparticles have negative zeta potential the opposing potentials result in attraction (Tc, Sharma, and Kennedy 2017).

Surface roughness could be an influencing factor for adsorption site selection, since smooth quartz cement faces were the only faces that showed less surface coverage. This could be explained by the processes described by Zhang et al. (2015). The hydrodynamic force necessary to remove nanoparticles increases with asperity height and therefore surface roughness.

The effect of brine on adsorption behavior seen in previous experiments was confirmed by these microscopy images. Higher nanoparticle adsorption was observed on FW samples for both rock types.

Adsorption in vacuum saturation samples was in single layers, whereas clusters have been observed in core flood samples. This suggests that the flow through the porous rock exerts higher hydrodynamic force on the nanoparticles as described by Zhang et al. (2015). Particles are pushed closer to each other or rock surfaces which increases the influence of attractive vdW forces.

The formation of a nanoparticle monolayer is a difference to the work of Abhishek and Hamouda (2017) who observed adsorption in successive layers due to drying effects. The rock samples were stored in brine after vacuum saturation to wash off excess nanoparticles appeared to be a successful method to reduce these drying effects.

Chapter 5 Conclusion and Future Work

5.1 Conclusion

A study on possible formation damage and sorption of nanoparticles was conducted by cross analyzing various laboratory data sources. The focus was given to evaluating fluid-fluid and fluid-rock interaction by means of compatibility tests, batch sorption experiments and core floods.

- Berea and Keuper outcrop rock material have similar porosity and specific surface area. Berea has a higher clay content and permeability is higher in Keuper although it has a higher degree of inhomogeneity. Zeta Potential for both nanofluids indicate, that the dispersion stability is provided by their surface modifications.
- Results suggest that formation water promoted the adsorption of both types of nanoparticles compared to test water due to the presence of divalent cations. The influence of pH on adsorption behavior can be seen in highest adsorption values seen in this brine and lowest in alkali solutions. Temperature had a minor effect on nanoparticle adsorption behavior.
- Berea rock showed a higher potential for adsorption than Keuper rock in all conducted experiments.
- Surface roughness seems to be the dominant driving factor for adsorption site selection. Small nanoparticle clusters have been observed on core flood samples, whereas vacuum saturation samples showed adsorption in a single layer.
- Core flood experiments showed that the injected nanofluids did not have a sufficient effect on permeability to be accounted for. A formation of a filter cake was not observed in the core flood experiments. A delayed nanofluid breakthrough compared to tracer suggests adsorption and saturation with nanoparticles. This leads to adsorption spots being occupied and an earlier elution compared to the tracer for a succeeding injection. It was observed, that bigger nanoparticles move faster through the core.

5.2 Future Work

The results gathered in this thesis work are unique in a way that the used nanofluids differ to ones used by other researchers, since they are still in the Research & Development phase and not commercially available. The knowledge gained in the process of this thesis is therefore highly important for further research in this field and application in a possible field trial.

Future work in this research area should investigate the effect of brine salinity on these nanoparticles. Further, tests with reservoir rock cores and produced reservoir brine shall be conducted. Understanding single-phase application provides the necessary framework to conduct further research in two phase experiments such as wettability alteration and IFT measurements.

Bibliography

3p Instruments. n.d. “Electroacoustics / Zeta Potential | 3P Instruments.” Accessed June 13, 2021. https://www.3p-instruments.com/measurement-methods/electroacoustics-zeta-potential/.

Abdo, J. 2014. “Nano-Attapulgite for Improved Tribological Properties of Drilling Fluids.” *Surface and Interface Analysis* 46 (10–11): 882–87. https://doi.org/10.1002/sia.5472.

Abhishek, Rockey. 2019. *Interaction of Silica Nanoparticles with Chalk and Sandstone Minerals: Adsorption, Fluid/Rock Interactions in the Absence and Presence of Hydrocarbons*. University of Stavanger, Norway. https://uis.brage.unit.no/uis-xmlui/handle/11250/2602326.

Abhishek, Rockey, and Aly Hamouda. 2017. “Effect of Various Silica Nanofluids: Reduction of Fines Migrations and Surface Modification of Berea Sandstone.” *Applied Sciences* 7 (November): 1216. https://doi.org/10.3390/app7121216.

Abhishek, Rockey, Aly A. Hamouda, and Amr Ayoub. 2018. “Effect of Silica Nanoparticles on Fluid/Rock Interactions during Low Salinity Water Flooding of Chalk Reservoirs.” *Applied Sciences* 8 (7). https://doi.org/10.3390/app8071093.

Akhtar, Kalsoom, Shahid Ali Khan, Sher Bahadar Khan, and Abdullah M. Asiri. 2018. “Scanning Electron Microscopy: Principle and Applications in Nanomaterials Characterization.” In *Handbook of Materials Characterization*, edited by Surender Kumar Sharma, 113–45. Cham: Springer International Publishing. https://doi.org/10.1007/978-3-319-92955-2_4.

Al-Malki, Needaa, Peyman Pourafshary, Hamoud Al-Hadrami, and Jamil Abdo. 2016. “Controlling Bentonite-Based Drilling Mud Properties Using Sepiolite Nanoparticles.” *Petroleum Exploration and Development* 43 (4): 717–23. https://doi.org/10.1016/S1876-3804(16)30084-2.

Alomair, Osamah A., Khaled M. Matar, and Yousef H. Alsaeed. 2014. “Nanofluids Application for Heavy Oil Recovery.” In . https://doi.org/10.2118/171539-MS.

Al-shehri, Abdullah, Erika Ellis, Jesus Servin, Dmitry Kosynkin, Mazen Kanj, and Howard Schmidt. 2013. “Illuminating The Reservoir: Magnetic NanoMappers.” *SPE Middle East Oil and Gas Show and Conference, MEOS, Proceedings* 3 (March). https://doi.org/10.2118/164461-MS.

Amanullah, Md.., Mohammad K Al-Arfaj, and Ziad Al-Abdullatif. 2011. “Preliminary Test Results of Nano-Based Drilling Fluids for Oil and Gas Field Application.” In . https://doi.org/10.2118/139534-MS.

Anton Paar. n.d. “Anton Paar.” https://www.anton-paar.com/us-en/.

Bennion, D. 2002. “An Overview of Formation Damage Mechanisms Causing a Reduction in the Productivity and Injectivity of Oil and Gas Producing Formations.” *Journal of Canadian Petroleum Technology - J CAN PETROL TECHNOL* 41 (November). https://doi.org/10.2118/02-11-DAS.

Bera, Achinta, and Hadi Belhaj. 2016. “Application of Nanotechnology by Means of Nanoparticles and Nanodispersions in Oil Recovery - A Comprehensive Review.” *Journal of Natural Gas Science and Engineering* 34 (August): 1284–1309. https://doi.org/10.1016/j.jngse.2016.08.023.

Bergaya, Fa, and G. Lagaly. 2006. “Chapter 1 General Introduction: Clays, Clay Minerals, and Clay Science.” *Developments in Clay Science* 1 (December). https://doi.org/10.1016/S1572-4352(05)01001-9.

Bila, Alberto, and Ole Torsæter. 2021. “Experimental Investigation of Polymer-Coated Silica Nanoparticles for EOR under Harsh Reservoir Conditions of High Temperature and Salinity.” *Nanomaterials* 11 (3). https://doi.org/10.3390/nano11030765.

Biochrom. n.d. “UV-VIS Spectrophotometry.” Accessed April 15, 2021. www.biochrom.co.uk.

Boisnault, Jean-Marc, Dominique Guillot, Pierre Maroy, Philippe Revil, Robert Roemer, A. Bourahla, T. Tirlia, et al. 1999. “Concrete Developments in Cementing Technology.” *Oilfield Review* 11 (May): 16–29.

Brunauer, Stephen, P. H. Emmett, and Edward Teller. 1938. “Adsorption of Gases in Multimolecular Layers.” *Journal of the American Chemical Society* 60 (2): 309–19. https://doi.org/10.1021/ja01269a023.

Cai, Jihua, Martin Chenevert, Mukul Sharma, and James Friedheim. 2012. “Decreasing Water Invasion Into Atoka Shale Using Nonmodified Silica Nanoparticles.” *SPE Drilling & Completion - SPE DRILL COMPLETION* 27 (March): 103–12. https://doi.org/10.2118/146979-PA.

Cao, Shuang, Junbong Jang, W. Waite, Mohammad Jafari, and Jongwon Jung. 2017. *A 2D Micromodel Study of Fines Migration and Clogging Behavior in Porous Media: Implications of Fines on Methane Extraction from Hydrate-Bearing Sediments*.

Carvalho, Patrícia M., Mário R. Felício, Nuno C. Santos, Sónia Gonçalves, and Marco M. Domingues. 2018. “Application of Light Scattering Techniques to Nanoparticle Characterization and Development.” *Frontiers in Chemistry* 6. https://doi.org/10.3389/fchem.2018.00237.

Cheraghian, Goshtasp, Sara Rostami, and Masoud Afrand. 2020. “Nanotechnology in Enhanced Oil Recovery.” *Processes* 8 (9). https://doi.org/10.3390/pr8091073.

Contreras, Oscar, Geir Hareland, Maen Husein, Runar Nygaard, and Mortadha Alsaba. 2014. “Application of In-House Prepared Nanoparticles as Filtration Control Additive to Reduce Formation Damage.” In . https://doi.org/10.2118/168116-MS.

Deng, Sai, Chao Kang, Alireza Bayat, Ergun Kuru, Manley Osbak, Kristin Barr, and Cainan Trovato. 2020. “Rheological Properties of Clay-Based Drilling Fluids and Evaluation of Their Hole-Cleaning Performances in Horizontal Directional Drilling.” *Journal of Pipeline Systems Engineering and Practice* 11 (August): 04020031. https://doi.org/10.1061/(ASCE)PS.1949-1204.0000475.

Ehtesabi, Hamide, M. Mahdi Ahadian, and Vahid Taghikhani. 2015. “Enhanced Heavy Oil Recovery Using TiO2 Nanoparticles: Investigation of Deposition during Transport in Core Plug.” *Energy & Fuels* 29 (1): 1–8. https://doi.org/10.1021/ef5015605.

Fakoya, Muili Feyisitan, and Subhash Nandlal Shah. 2017. “Emergence of Nanotechnology in the Oil and Gas Industry: Emphasis on the Application of Silica Nanoparticles.” *Petroleum* 3 (4): 391–405. https://doi.org/10.1016/j.petlm.2017.03.001.

Fanchi, John R. 2002. “Chapter 16 - Improved Recovery.” In *Shared Earth Modeling*, edited by John R. Fanchi, 272–81. Woburn: Butterworth-Heinemann. https://doi.org/10.1016/B978-075067522-2/50016-1.

Fink, Johannes Karl. 2015a. “Chapter IV - Other Water-Based Uses.” In *Water-Based Chemicals and Technology for Drilling, Completion, and Workover Fluids*, 179–207. Boston: Gulf Professional Publishing. https://doi.org/10.1016/B978-0-12-802505-5.00004-4.

———. 2015b. “Chapter V - Additives for General Uses.” In *Water-Based Chemicals and Technology for Drilling, Completion, and Workover Fluids*, 209–50. Boston: Gulf Professional Publishing. https://doi.org/10.1016/B978-0-12-802505-5.00005-6.

———. 2015c. “Water-Based Chemicals and Technology for Drilling, Completion, and Workover Fluids.” In *Water-Based Chemicals and Technology for Drilling, Completion, and Workover Fluids*, 179–207. Boston: Gulf Professional Publishing. https://doi.org/10.1016/B978-0-12-802505-5.00004-4.

Fisher Scientific. n.d. “Thermo Scientific™ Evolution™ 201/220 UV-Vis-Spektrophotometer Evolution 201 PC Thermo Scientific™ Evolution™ 201/220 UV-Vis-Spektrophotometer | Fisher Scientific.” Accessed August 17, 2021. https://www.fishersci.de/shop/products/evolution-201-220-uv-visible-spectrophotometers/10161808?searchHijack=true&searchTerm=evolution-201-220-uv-visible-spectrophotometers&searchType=Rapid&matchedCatNo=10161808.

Herrada García, Rosa, Maribel Pérez Corona, Reena Shrestha, Sibel Pamukcu, and Erika Bustos. 2014. “Electrokinetic Remediation of Polluted Soil Using Nano-Materials: Nano-Iron Case.” In , 37/661.

Hoelscher, Katherine, Guido Stefano, Meghan Riley, and Steven Young. 2012. “Application of Nanotechnology in Drilling Fluids,” June. https://doi.org/10.2118/157031-MS.

Horiba. n.d. “Dynamic Light Scattering for Nanoparticle Size Analysis - HORIBA.” Accessed June 21, 2021. https://www.horiba.com/at/scientific/products/particle-characterization/technology/dynamic-light-scattering/.

Hoxha, B. B., E.. van Oort, and H.. Daigle. 2019. “How Do Nanoparticles Stabilize Shale?” *SPE Drilling & Completion* 34 (02): 143–58. https://doi.org/10.2118/184574-PA.

Huh, Chun, Hugh Daigle, Valentina Prigiobbe, and Maša Prodanović. 2019. *Practical Nanotechnology for Petroleum Engineers*. https://doi.org/10.1201/9781351210362.

Jahagirdar, Shruti. 2008. “Oil-Microbe Detection Tool Using Nano Optical Fibers,” March. https://doi.org/10.2118/113357-MS.

Jauhari, Smita, Kinnari Parekh, K.B. Pai, and Ramesh Upadhyay. 2010. “Using Nanomagnetic Fluid for Corrosion Inhibition of Mild Steel.” *Materials Performance* 49 (August): 54–58.

Kamal, Muhammad Shahzad, Ahmad A. Adewunmi, Abdullah S. Sultan, Mohammed F. Al-Hamad, and Umer Mehmood. 2017. “Recent Advances in Nanoparticles Enhanced Oil Recovery: Rheology, Interfacial Tension, Oil Recovery, and Wettability Alteration.” Edited by Minea A. Adriana. *Journal of Nanomaterials* 2017 (October): 2473175. https://doi.org/10.1155/2017/2473175.

Kanj, Mazen Y., Md. Harunar Rashid, and Emmanuel P. Giannelis. 2011. “Industry First Field Trial of Reservoir Nanoagents.” In . https://doi.org/10.2118/142592-MS.

Khabashesku, V. 2016. “Monteiro, O. R., Murugesan, S., Suresh, R., & Khabashesku, V. N. (2016, May 9). Corrosion- and Erosion-Resistant Metal Matrix Nanocomposite Coatings for the Oil and Gas Industry. 179933-MS SPE Conference Paper – 2016. Society of Petroleum Engineers. Doi:10.2118/179933-MS.,” May.

Khilar, K., and H. S. Fogler. 1984. “The Existence of a Critical Salt Concentration for Particle Release.” *Journal of Colloid and Interface Science* 101: 214–24.

———. 1998. “Migrations of Fines in Porous Media.” In .

Khoshnevisan, Kamyar, and Mohammad Barkhi. 2015. *Zeta Potential*. https://doi.org/10.13140/RG.2.1.4554.3844.

Ladwein and Sauer. 1986. "Bericht über Sedimentogrphische Untersuchungen von Proben aus dem Berea-Sandstein und dem Nordhorner Sandstein." TG-LAP Geologisches Labor.

Lashari, Najeebullah, and Tarek Ganat. 2020. "Emerging Applications of Nanomaterials in Chemical Enhanced Oil Recovery: Progress and Perspective." *Chinese Journal of Chemical Engineering* 28 (8): 1995. https://doi.org/10.1016/j.cjche.2020.05.019.

Lauth, Jakob, and Jürgen Kowalczyk. 2016. *Einführung in Die Physik Und Chemie Der Grenzflächen Und Kolloide*. https://doi.org/10.1007/978-3-662-47018-3.

Lavrov, Alexandre, author. 2016. *Physics and Mechanics of Primary Well Cementing*. Switzerland : Springer, 2016. https://search.library.wisc.edu/catalog/9912248648302121.

Ledwani, Lalita, and Jitendra S. Sangwai. 2020. "Nanotechnology for Energy and Environmental Engineering." In *Nanotechnology for Energy and Environmental Engineering*, 257–327. https://public.ebookcentral.proquest.com/choice/publicfullrecord.aspx?p=6133727.

Li, Hui, Hui-gang Xiao, Jie Yuan, and Jinping Ou. 2004. "Microstructure of Cement Mortar with Nano-Particles." *Composites Part B: Engineering* 35 (March): 185–89. https://doi.org/10.1016/S1359-8368(03)00052-0.

Li, Jing, and Meyya Meyyappan. 2011. REAL TIME OIL RESERVOIR EVALUATION USING NANOTECHNOLOGY. The United States of America as represented by the Administrator of the National Aeronautics and Space Administration (NASA), Washington, DC (US) US 7,875,455 B1, filed July 12, 2006, and issued 2011.

Li, Shidong, Ole Torsæter, Hon Chung Lau, Nanji J. Hadia, and Ludger P. Stubbs. 2019. "The Impact of Nanoparticle Adsorption on Transport and Wettability Alteration in Water-Wet Berea Sandstone: An Experimental Study." *Frontiers in Physics* 7: 74. https://doi.org/10.3389/fphy.2019.00074.

Liu, He, Xu Jin, and Bin Ding. 2016. "Application of Nanotechnology in Petroleum Exploration and Development." *Petroleum Exploration and Development* 43 (6): 1107–15. https://doi.org/10.1016/S1876-3804(16)30129-X.

Luxbacher, Thomas. 2014. *The Zeta Potential for Solif Surface Analysis*. Austria: Anton Paar GmbH.

Maserati, Gianfranco, Emanuela Daturi, Lucilla del gaudio, Alessandra Belloni, Stefano Bolzoni, Walter Lazzari, and Giuseppe Leo. 2010. "Nano-Emulsions as Cement Spacer Improve the Cleaning of Casing Bore During Cementing Operations," September. https://doi.org/10.2118/133033-MS.

McDonald, Michael. 2012. "A Novel Potassium Silicate for Use in Drilling Fluids Targeting Unconventional Hydrocarbons." In . https://doi.org/10.2118/162180-MS.

Meier, Florian, and Gerhard Heinzmann. 2017. "Field-Flow Fractionation: A Powerful Technology for the Separation and Advanced Characterization of Proteins, Antibodies, Viruses, Polymers and Nano-/Microparticles." *Www.Chemie.De*, July.

Metin, Cigdem O., Larry W. Lake, Caetano R. Miranda, and Quoc P. Nguyen. 2011. "Stability of Aqueous Silica Nanoparticle Dispersions." *Journal of Nanoparticle Research* 13 (2): 839–50. https://doi.org/10.1007/s11051-010-0085-1.

Miller, John. 2019. *How To Measure Zeta Potential More Confidently - Slides and Notes*.

Mogensen, Kristian and Bennetzen. 2014. *Novel Applications of Nanoparticles for Future Enhanced Oil Recovery*. https://doi.org/10.2523/17857-MS.

Mohan, K.Krishna, Ravimadhav N. Vaidya, Marion G. Reed, and H.Scott Fogler. 1993. "Water Sensitivity of Sandstones Containing Swelling and Non-Swelling Clays." *A Collection of Papers Presented at the International Symposium on Colloids in the Aquatic Environment, Organized by SCI and Surface Chemistry Group* 73 (June): 237–54. https://doi.org/10.1016/0927-7757(93)80019-B.

Murray, Haydn. 2006. "Chapter 2 Structure and Composition of the Clay Minerals and Their Physical and Chemical Properties." *Developments in Clay Science* 2 (December). https://doi.org/10.1016/S1572-4352(06)02002-2.

Neubauer, Elisabeth, Rafael E. Hincapie, Ante Borovina, Magdalena Biernat, Torsten Clemens, and Yusra Khan Ahmad. 2020. "Influence of Nanofluids on Wettability Changes and Interfacial Tension Reduction." In . https://doi.org/10.2118/200643-MS.

Neubauer, Elisabeth, Rafael E. Hincapie, Torsten Clemens, and Maximilian Cornelius. 2020. "Selection of Nanomaterials as Emulsion Stabilizers in Alkali-Polymer EOR of High-TAN Number Oil." In . https://doi.org/10.2118/200411-MS.

Nikolova, Maria, and Stanislav Bayryamov. 2019. *A Review of Methods and Techniques for Characterization of Structure, Morphology and Dispersion Stability Pf Microcapsules*.

Nowack, Bernd, and Thomas Bucheli. 2007. "Occurrence, Behavior and Effects of Nanoparticles in the Environment." *Environmental Pollution (Barking, Essex : 1987)* 150 (December): 5–22. https://doi.org/10.1016/j.envpol.2007.06.006.

Oilfieldteam.com. 2017. "Drilling Fluid Additives." 2017. https://oilfieldteam.com/en/a/learning/Drilling-Fluid-Additives.

Omurlu, Cigdem, H. Pham, and Q. P. Nguyen. 2016. "Interaction of Surface-Modified Silica Nanoparticles with Clay Minerals." *Applied Nanoscience* 6 (8): 1167–73. https://doi.org/10.1007/s13204-016-0534-y.

OSU.edu. n.d. "Ion Chromatography- Theory | OSU Chemistry REEL Program." Accessed August 20, 2021. https://research.cbc.osu.edu/reel/research-modules/environmental-chemistry/instrumentation/instrument-calibration/ion-chromatography-theory/.

Petosa, Adamo R., Deb P. Jaisi, Ivan R. Quevedo, Menachem Elimelech, and Nathalie Tufenkji. 2010. "Aggregation and Deposition of Engineered Nanomaterials in Aquatic Environments: Role of Physicochemical Interactions." *Environmental Science & Technology* 44 (17): 6532–49. https://doi.org/10.1021/es100598h.

Pham, Hieu, and Quoc P. Nguyen. 2013. "Effect of Silica Nanoparticles on Clay Swelling and Aqueous Stability of Nanoparticle Dispersions." *Journal of Nanoparticle Research* 16 (1): 2137. https://doi.org/10.1007/s11051-013-2137-9.

Pusey, P. N. 1974. "Macromolecular Diffusion." In *Photon Correlation and Light Beating Spectroscopy*, edited by H. Z. Cummins and E. R. Pike, 387–428. NATO Advanced Study Institutes Series. Boston, MA: Springer US. https://doi.org/10.1007/978-1-4615-8906-8_10.

Qiu, Canrong, Peter Eng, Christoph Hennig, and Moritz Schmidt. 2018. "Competitive Adsorption of ZrO2 Nanoparticle and Alkali Cations (Li+-Cs+) on Muscovite (001)." *Langmuir : The ACS Journal of Surfaces and Colloids* 34 (September). https://doi.org/10.1021/acs.langmuir.8b02277.

Rahmani, Amir, Steve Bryant, Chun Huh, Alex Athey, Mohsen Ahmadian, Jiuping Chen, and Michael Wilt. 2013. "Crosswell Magnetic Sensing of Superparamagnetic

Nanoparticles for Subsurface Applications." *SPE Journal* 1 (September). https://doi.org/10.2118/166140-MS.

Richard, Udoh Richard. 2013. "SAND & FINES IN MULTIPHASE OIL AND GAS PRODUCTION." Institutt for petroleumsteknologi og anvendt geofysikk. https://ntnuopen.ntnu.no/ntnu-xmlui/handle/11250/240270.

Rostami, Peyman, Mohammad Sharifi, Babak Aminshahidy, and Jalal Fahimpour. 2019. "The Effect of Nanoparticles on Wettability Alteration for Enhanced Oil Recovery: Micromodel Experimental Studies and CFD Simulation." *Petroleum Science* 16 (4): 859–73. https://doi.org/10.1007/s12182-019-0312-z.

Saleh, Samhar. 2020. "Wettability Changes Due to Nanomaterials and Alkali in Spontaneous Imbibition Experiments." University of Leoben. https://pure.unileoben.ac.at/portal/en/publications/wettability-changes-due-to-nanomaterials-and-alkali-in-spontaneous-imbibition-experiments(7e69d455-3e52-4e20-9342-1d98a21cba4a).html?customType=theses.

Salih, A. H., T. A. Elshehabi, and H. I. Bilgesu. 2016. "Impact of Nanomaterials on the Rheological and Filtration Properties of Water-Based Drilling Fluids." In . https://doi.org/10.2118/184067-MS.

Sandeep, R., Shikha Jain, and A. Agrawal. 2020. "Application of Nanoparticles-Based Technologies in the Oil and Gas Industry." In .

Sauer and Phillipovich. 1988. "Mineralogische Untersuchung Des Keupersandsteins." TG-G Geologisches Labor.

Shah, Rusheet D. 2009. "Application of Nanoparticle Saturated Injectant Gases for EOR of Heavy Oils." In . https://doi.org/10.2118/129539-STU.

Sharma, Mukul M., R.. Zhang, M. E. Chenevert, L.. Ji, Q.. Guo, and J.. Friedheim. 2012. "A New Family of Nanoparticle Based Drilling Fluids." In . https://doi.org/10.2118/160045-MS.

Srivatsa, Jayanth, and Malgorzata Ziaja. 2011. "An Experimental Investigation on Use of Nanoparticles as Fluid Loss Additives in a Surfactant - Polymer Based Drilling Fluids." *Society of Petroleum Engineers - International Petroleum Technology Conference 2012, IPTC 2012* 3 (November). https://doi.org/10.2523/IPTC-14952-MS.

Szczygieł, Andrzej. 2019. "Complex Reservoir Drilling Fluid Solutions for Reservoir Drilling." *AGH Drilling, Oil, Gas*, no. Vol. 36, 1. https://doi.org/10.7494/drill.2019.36.1.45.

Tanikawa, Wataru, and Toshihiko Shimamoto. 2009. "Comparison of Klinkenberg-Corrected Gas Permeability and Water Permeability in Sedimentary Rocks." *International Journal of Rock Mechanics and Mining Sciences* 46 (December): 229–38. https://doi.org/10.1016/j.ijrmms.2008.03.004.

Tc, Prathna, Saroj Sharma, and Maria Kennedy. 2017. *Arsenic and Fluoride Removal by Iron Oxide and Iron Oxide/Alumina Nanocomposites: A Comparison*. https://doi.org/10.11159/icnfa17.118.

Tournassat, Christophe, Ian C. Bourg, Carl I. Steefel, and Faïza Bergaya. 2015. "Chapter 1 - Surface Properties of Clay Minerals." In *Developments in Clay Science*, edited by Christophe Tournassat, Carl I. Steefel, Ian C. Bourg, and Faqpza Bergaya, 6:5–31. Elsevier. https://doi.org/10.1016/B978-0-08-100027-4.00001-2.

Wasan, D., Alex Nikolov, and Kirti Kondiparty. 2011. "The Wetting and Spreading of Nanofluids on Solids: Role of the Structural Disjoining Pressure." *Current Opinion in Colloid & Interface Science - CURR OPIN COLLOID INTERFACE S* 16 (August): 344–49. https://doi.org/10.1016/j.cocis.2011.02.001.

"What Is EOR, and How Does It Work?" n.d. Accessed July 11, 2021. https://www.rigzone.com/training/insight.asp?insight_id=313&c_id=.

Williamson, Don. 2013. "The Defining Series: Drilling Fluid Basics | Schlumberger." Oilfield Review. https://www.slb.com/resource-library/oilfield-review/defining-series/defining-drilling-fluids.

Wood, David A., and Bin Yuan. 2018. "Chapter Fifteen - Integrated Risks Assessment and Management of IOR/EOR Projects: A Formation Damage View." In *Formation Damage During Improved Oil Recovery*, edited by Bin Yuan and David A. Wood, 587–631. Gulf Professional Publishing. https://doi.org/10.1016/B978-0-12-813782-6.00015-4.

Xu, Qing, Meng Tao, and Miao Huang. 2011. "Effects of Nano-CaCO3 on the Compressive Strength and Microstructure of High Strength Concrete in Different Curing Temperature." *Applied Mechanics and Materials* 121–126 (October). https://doi.org/10.4028/www.scientific.net/AMM.121-126.126.

Xu, Zichen. 2012. "Application of Nanotechnology on Borehole Wall Stability in Gas-Liquid Medium Transition during Gas Drilling." In . https://doi.org/10.2118/160906-STU.

Yu, Jianjia, Cheng An, Di Mo, Ning Liu, and Robert Lee. 2012. "Study of Adsorption and Transportation Behavior of Nanoparticles in Three Different Porous Media." In . https://doi.org/10.2118/153337-MS.

Yukselen-Aksoy, Yeliz, and Abidin Kaya. 2003. "Zeta Potential of Kaolinite in the Presence of Alkali, Alkaline Earth and Hydrolyzable Metal Ions." *Water Air and Soil Pollution* 145 (May): 155–68. https://doi.org/10.1023/A:1023684213383.

Zhang, Tiantian, Michael J. Murphy, Haiyang Yu, Hitesh G. Bagaria, Ki Youl Yoon, Bethany M. Neilson, Christopher W. Bielawski, Keith P. Johnston, Chun Huh, and Steven L. Bryant. 2015. "Investigation of Nanoparticle Adsorption During Transport in Porous Media." *SPE Journal* 20 (04): 667–77. https://doi.org/10.2118/166346-PA.

Acronyms

AF4	Asymmetric Flow Field Flow Fractionation
AS	Alkali Solution
BET	Brunauer-Emett-Teller
CEC	Cation Exchange Capacity
CSC	Critical Salt Concentration
DIW	Deionized Water
DLS	Dynamic Light Scattering
DLVO	Dejaguin- Landau- Verwey-Overbeek
ECD	Equivalent Circulating Density
EDL	Electrical Double Layer
EOR	Enhanced Oil Recovery
FFF	Field Flow Fractionation
FNP	Hydrophilic Fumed Silica Nanoparticles
FNP-O	Hydrophobic Fumed Silica Nanoparticles
FW	Formation Water
IC	Ion Chromatography
IFT	Interfacial Tension
IOR	Improved Oil Recovery
KPI	Key Performance Indicators
LDE	Laser Doppler Electrophoresis
MALS	Multi Angle Light Scattering
NF	NanoFluid
OBM	Oil-Based Mud
OOIP	Oil Originally In Place
PALS	Phase Analysis Light Scattering
PEG	Polyethylenglycol
PTFE	Polytetrafluoroethylene
RCA	Routine Core Analysis
RDF	Reservoir Drill-in Fluids
SEM	Scanning Electron Microscopy
TEM	Transmission Electron Microscope
TO	Tetrahedral-Octahedral
TOT	Tetrahedral-Octahedral-Tetrahedral
TW	Test Water
UV-Vis	Ultraviolet-Visible (Spectrophotometry)
vdW	van der Waals

Symbols

Symbol	Name	Value / [unit]
A	Area	[m^2]
A_c	Hamaker constant	[J]
a_i	Particle radius	[m]
Abs	Absorbance	[-]
Abs_{corr}	Absorbance correction	[-]
c	Molar concentration	[mol/l]
D	Separation distance	[m]
D_c	Diffusion coefficient	[m^2/s]
d_i	Concentration Offset	[wt%]
d_p	Particle diameter	[m]
e	elementary charge	$1.602 \cdot 10^{-19}$ C
h	Surface to surface separation distance	[m]
I	Ionic strength	[M]
I	Intensity of transmitted light	[W/m^2]
I_0	Intensity of incident light	[W/m^2]
I_{str}	Streaming current	[A]
k_B	Boltzmann constant	$1.3805 \cdot 10^{-23}$ J/K
k	Permeability	[mD]
k_i	Calibration Plot Slope	
l	Film thickness	[m]
L	length	[m]
m_{Hg}	Mass of displaced mercury	[kg]
N_A	Avogadro constant	$6.02214 \cdot 10^{-23}$ mol^{-1}
p	pressure	[Pa]
q	Flow rate	[ml/min]
R_g	Radius of gyration	[m]
R_{hyd}	Hydrodynamic radius	[m]
$R_{monolayer}$	Maximum adsorption concentration in monolayer	[-]
s	Distance between polymer chains on surface	[m]
T	Absolute temperature	[K]
T_B	Transmittance	[-]
V_A	Attraction energy	[J]
V_{bulk}	Bulk volume	[m^3]
V_{EDL}	Electrical-double layer interaction energy	[J]
V_{grain}	Grain volume	[m^3]
V_T	Total interaction energy	[J]
V_{vdW}	Van der Waals interaction energy	[J]
V_R	Repulsion energy	[J]
V_R	Reference chamber volume	[m^3]
V_S	Potential energy as function of solvent	[J]
V_S	Sample chamber volume	[m^3]
V_{ST}	Steric interaction energy	[J]
z	Valence	[-]

Symbol	Name	Value / [unit]
Γ_i	Dimensionless surface potential for particle $\Gamma_i = \tanh[(ze\psi_i)/(4k_BT)]$	[-]
ε_0	Dielectric permittivity in vacuum	$8.85 \cdot 10^{-12}$ F/m
ε_r	Relative dielectric permittivity of solution	[-]
ε	molar attenuation coefficient	$[M^{-1}cm^{-1}]$
ζ	Zeta potential	[mV]
η	Dynamic viscosity $\eta = \mu \cdot \varrho$	[Pa·s]
θ	Angle of scattering	[°]
κ^{-1}	Debye length	[m]
μ	Kinematic viscosity	$[m^2 \cdot s^{-1}]$
ϱ_{Hg}	Density mercury	$[kg/m^3]$
ϱ_P	Particle density	$[kg/m^3]$
λ	Characteristic wavelength	[m]
Φ	Porosity	[%]
Ψ, ψ_i	Surface potential	

List of Figures

Figure 2.1: Effect of wettability on fines migration in water wet rock: In most cases the rock and fines are water wet. When oil is produced fines are mobilized in a later stage of production: a) fines immobile in wetting phase (water); b) non wetting phase (oil) is mobilized - fines remain immobile; c) wetting phase mobilizes and fines migrate (modified after Bennion 2002). 6
Figure 2.2: Clay mineral particles have a substructure that can be arranged in TOT or TO layers connected by interlayer cations (modified after Tournassat et al. 2015). 7
Figure 2.3: Shear stress versus shear rate relationships of various rheological models. For drilling fluid a behaviour similar to Herschel-Bulkley is desired, since there at low shear rates (at a pump standstill) cuttings are prevented from settling, but at higher shear rates the viscosity does not increase dramatically and therefore reduce pump requirements (Deng et al. 2020). 9
Figure 2.4: Schematic illustration of a) cementing operation and b) finished well after cementing and perforation. During the cementing operation (a) the cement is pushed down the inside of the casing until it exits and fills the annular space between the steel pipe and the rock. Then the next section can be drilled with a smaller size bit on the inside of this section. Multiple casing strings are placed in succession to form the finished well (b) (Lavrov 2016). 10
Figure 2.5: Layer succession according to Bockris-Müller-Devanthan model: A charged particle is surrounded by the stern layer and a diffuse layer. The graph shows the surface potential as a function of distance from particle surface (Herrada García et al. 2014). 12
Figure 2.6: Electrical potential as a function of distance from the surface of a charged particle (modified after Miller 2019). 13
Figure 2.7: Charge formulation at solid-liquid interface with acidic (left) and basic (right) functional groups (Luxbacher 2014). 14
Figure 2.8: Streaming potential measurement: Electrolyte flow in a capillary channel generates a measurable charge separation that can be measured as an electrical potential (Anton Paar). 15
Figure 2.9: Nanofluids are utilized in EOR to obtain higher oil recovery by the following depicted effects: increase of disjoining pressure that leads to a wettability alteration, pore channel plugging, stabilization of emulsion and IFT reduction. 19
Figure 2.10: Schematic of three methods to provide colloidal stability in a nanoparticle suspension: for electrostatic stabilization (a) ionic groups are absorbed to the surface of the nanoparticle and form a charged layer; b) steric stabilization is usually obtained by grafting macromolecules to the surface. These must be longer than the effective range of van der Waals forces to prevent attraction. In depletion stabilization (c) polymers are added to the solution that separate the particles (Huh et al. 2019). 21
Figure 2.11: Interaction energy curves between nanoparticle (-20 mV surface potential) and Biose- sand grains (-22mV zeta potential) in deionized water (Zhang et al. 2015). 22
Figure 3.1: Berea (left) and Keuper (right) outcrop rock plugs were used in the experiments. ... 25
Figure 3.2: SEM image of Berea. Quartz cement can be identified by its smooth surfaces compared to the sand grains. Kaolinite is placed between sand grains in its typical book-shape. 26
Figure 3.3: SEM image of Keuper. The sand grains are more rounded compared to Berea, but a reduced amount of clay and quartz cement is visible. 26
Figure 3.4: Petrophysical properties of the used Berea (left) and Keuper (right) core plugs. 27
Figure 3.5: TEM (left, 10 nm; right, 200 nm) images of unmodified silica nanoparticles. 29
Figure 3.6: TEM images of NF A (left) and NF B (right) in 200 nm and 20 nm. 29

Figure 3.7: Zeta-Potential and specific conductivity for NF A and NF B. 30
Figure 3.8: A helium porosimeter was used to determine the porosity of the rock sample. First helium is filled into the reference chamber until a stable pressure was observed. Then all valves are closed and the valve between the two chambers is opened and a stable pressure recorded. 32
Figure 3.9: Streaming potential of Berea rock in different brines. The zeta potential values reach equilibrium between -14 and -17.5 mV. 33
Figure 3.10: Principle of Asymmetric Flow Field-Flow Fractionation (Meier and Heinzmann 2017). 35
Figure 3.11: Static and dynamic light scattering: Lower variation in scattering intensity and small angle scattering for larger particles (Nikolova and Bayryamov 2019). 35
Figure 3.12: Thermo Scientific Evolution 201 (Fisher Scientific). 36
Figure 3.13: A sample holder was mounted on an axis which was connected to an electric motor outside the heating cabinet. The samples were placed in the sample holder and rotated for 24 h at ~35 rpm at RT or 60°C. 38
Figure 3.14: Batch sorption samples after gravity settling. The glass bottles are filled with Berea (left) and Keuper (right) rock material and NF A in FW. After one hour resting time, the fluid was taken into a syringe and filtered to be analysed. 38
Figure 3.15: Core flooding setup for permeability measurements. The core holder was placed vertically inside a heating cabinet and pressure sensors were fitted to record the pressure differential across the core. A confining pressure of 35 bar was used. 39
***Figure 3.16**: Core flooding setup for effluent analysis. Fluid samples were collected after being injected into the rock at 60°C.* 40
Figure 4.1: Precipitations in a solution containing formation water and alkali (Saleh 2020). 43
Figure 4.2: Calibration graph for different concentrations of NF A (a) and NF B (b) in TW, FW and AS. The solutions were left resting for 24h after mixing and filtered using a 0,45 μm filter. A linear trend was found to fit the measured behaviour best for all solutions. These calibration plots enable the calculation of nanoparticle concentration from an absorbance measurement. 44
Figure 4.3: Permeability to brine was measured before a nanofluid injection (blue), after an injection of 0.1 wt% of NF (orange) and after an injection of 1 wt% NF (grey). NF A (a) and NF B (b) were both diluted in TW and all permeability measurements were conducted with TW. 49
Figure 4.4: Scanning Electron Microscopy (SEM) image of a core flood rock sample following an injection of 1 wt% nanofluid A in test water. 50
Figure 4.5: Effluent analysis for 0.1 wt% (a) and 1 wt% (b) NF A in TW in Berea sandstone. For the low concentration injection high adsorption is seen for NF A, whereas the tracer seems to pass the core unaffected. During the high concentration injection of NF A, the effluent concentration follows the tracer concentration better indicating no further adsorption. Particle size measurements confirm the low NF recovery (green) and larger particles arriving earlier in the effluent. 51
Figure 4.6: A comparison of tracer concentration history indicates a similar tracer breakthrough at ~0.95 PV (50%) for both injection steps and a slightly longer retention in the second injection. 52
Figure 4.7: Preceding tracer test showing a nanofluid breakthrough after 17 PV. In this core flood 0.1 wt% NF A in TW was injected and nanoparticle concentration was evaluated using DLS. 53
Figure 4.8: Effluent analysis for 0.1 wt% (a) and 1 wt% (b) NF A in TW in Keuper sandstone. A delayed breakthrough of nanoparticles can be seen in (a) peaking at a higher concentration than injected. An earlier nanoparticle breakthrough is seen in (b) compared to the tracer.

Particle size measurements confirm UV-Vis concentration results and show larger particle arriving faster in the effluent. 54
Figure 4.9: Tracer concentration history for Nanofluid A in Keuper in two injection steps. An identical tracer breakthrough can be observed at 0.9 PV (50%) whereas the plateau is reached slower. A delayed decrease in concentration for the second injection step can be observed. 54
Figure 4.10: Effluent analysis for NF B in for 0.1 wt% (a) and 1 wt% (b) in TW in Berea sandstone. The calculated maximum concentration exceeds the injected concentration. The nanofluid shows only a slightly delayed breakthrough compared to the tracer. 55
Figure 4.11: Tracer breakthrough comparison for NF B in Berea shows both breakthroughs at 0.9 PV. 55
Figure 4.12: Effluent analysis for nanofluid (NF) B in Keuper shows concentration peaks exceeding the injected concentration. In both cases the calculated concentration remains at a constant level after the injection. 57
Figure 4.13: Tracer analysis for nanofluid (NF) B in Keuper outcrop core. The concentration history is almost parallel for both injection steps. 57
Figure 4.14: This image representative for SEM images conducted in this work. Nanoparticles can be observed on almost all surfaces of minerals. The only exception is quartz cement with its distinctive smooth faces (Vacuum saturation of 1 wt% NF A in formation water; Berea). 59
Figure 4.15: This overview shows various clay minerals that are coated completely with a layer of nanoparticles (Vacuum saturation of 1 wt% NF B in FW; Keuper). 60
Figure 4.16: A comparison between nanoparticle covered(left) and clean (right) kaolinite structures. Note, that the smoothed edges on left image are signs of weathering and not caused by the nanoparticle treatment (left: core flood sample of 1 wt% NF A in test water, Keuper; right: untreated sample, Berea). 60
Figure 4.17: Nanoparticles are adsorbed in patterns parallel to mineral edges. The images show vacuum saturation samples of 1wt% NF A in FW (left) and 1wt% NF B in TW (right). 61
Figure 4.18: Nanoparticles were also observed to adsorb on iron oxides as seen in this image. The nanoparticles seem to form towers that are directed away from the centers of these mineral spheres. (Vacuum saturation of 1 wt% NF A in FW; Berea). 61
Figure 4.19: This image shows a comparison between adsorption of NF A to Berea in formation water (left) compared TW (right). Surfaces in the FW sample were coated slightly more with nanoparticles. (left: Vacuum saturation of 1 wt% NF A in FW, Berea; right: vacuum saturation of 1 wt% NF A in TW, Berea). 62
Figure 4.20: Comparison between NF B in formation water (left) and test water (right) on kaolinite structures found in Keuper rock. The sample treated with NF B in TW shows slightly higher adsorption of nanoparticles (left: Vacuum saturation of 1 wt% NF B in FW, Keuper; right: Vacuum saturation of 1 wt% NF B in TW, Keuper). 62
Figure 4.21: The image on the left shows a rock sample that has been vacuum saturated whereas the image on the right shows a core flood sample. Both samples have been treated with 1 wt% nanofluid A in test water. Bigger particle structures can be seen on the core flood sample. 63
Figure 4.22: This comparison shows a rock sample that has been vacuum saturated on the left and a core flood sample on the right. Both samples have been treated with 1 wt% nanofluid B in test water, however bigger particle agglomeration can be seen the core flood image. 63

List of Tables

Table 2.1: Properties affecting the Zeta potential at solid – liquid interfaces. 14
Table 3.1: Petrophysical data of Berea and Keuper core plugs. 26
Table 3.2: Specific surface area measurements were conducted using the BET method for core plugs and crushed material.The similarity between the specific surface area of the crushed material underlines that the crushed material for both rock types was comparable in grain size. 27
Table 3.3: Composition of synthetic brines test water (TW) and formation water (FW). 28
Table 3.4: Properties of Nanofluids (NF). 29
Table 3.5: NF A and NF B were diluted in two concentrations each in TW and FW. The mixtures containing alkali were mixed in 0.1 wt% only. These pH measurements were performed in triplets and the standard deviation was ~$2 \cdot 10^{-2}$. 31
Table 3.6: Zeta potential measurements in test water (TW) and formation water (FW) with and without sodium carbonate. 36
Table 4.1: Calibration constants for 24 h aged nanofluid solutions after filtration at 270 nm. These constants were later used to calculate nanoparticle concentrations from UV-Vis absorption measurements (FW: formation water, TW: test water, AS: alkali solution). 44
Table 4.2: Absorbance correction factors for rock materials in different brines at two temperatures using doublet measurements and an average standard deviation for absorbance at 270 nm of $3.8 \cdot 10^{-3}$ (FW: formation water, TW: test water, AS: alkali solution). 44
Table 4.3: Adsorption results and pH measurements for NF A in Berea. Absorbance measurements were performed in doublets with an average standard deviation of $1.8 \cdot 10^{-3}$ for all fluids. pH standard deviation was defined as $2 \cdot 10^{-2}$ for all fluids in average (FW: formation water, TW: test water, AS: alkali solution). 46
Table 4.4: Adsorption results for NF A in Keuper. Absorbance measurements were performed in doublets with an average standard deviation of $5 \cdot 10^{-3}$ for all fluids. pH standard deviation was defined as $2 \cdot 10^{-2}$ for all fluids in average (FW: formation water, TW: test water, AS: alkali solution). 46
Table 4.5: Adsorption results for NF B in Berea. Note the increase in pH from 4.71 to 6.36 for 0.1 wt% NF B in FW at 60°C. Note the increase in pH from 4.71 to 6.36 for 0.1 wt% NF B in FW at 60°C.Absorbance measurements were performed in doublets with an average standard deviation of $7.4 \cdot 10^{-4}$. pH standard deviation was defined as $2 \cdot 10^{-2}$ for all fluids in average (FW: formation water, TW: test water, AS: alkali solution). 47
Table 4.6: *Adsorption results for NF B in Keuper. Note the increase in pH from 4.71 to 6.73 for 0.1 wt% NF B in FW at 60°C. Absorbance measurements were performed in doublets with an average standard deviation of $3.6 \cdot 10^{-3}$. pH standard deviation was defined as $2 \cdot 10^{-2}$ for all fluids in average (FW: formation water, TW: test water, AS: alkali solution).* 48
Table 4.7: Adsorption results following mass balance calculation for NF A in Berea. 52
Table 4.8: Adsorption results following mass balance calculation for NF A in Keuper. 54
Table 4.9: Adsorption calculation via mass balance following concentration calculation using UV-Vis spectroscopy data for nanofluid A in Berea outcrop core. 56
Table 4.10: Adsorption calculation via mass balance following concentration calculation using UV-Vis spectroscopy data for nanofluid B in Keuper outcrop core. 57
Table 4.11: Particle size measurements for different concentrations of nanofluids (NF) in two brines (formation water (FW) and test water (TW). R_g: Radius of gyration (R50; MALS), R_h: Hydrodynamic radius (DLS). 58